5-2012

Characterizing phyllosilicate distribution, abundance, and origin on Mars

Christina Elizabeth Viviano
cviviano@utk.edu

To the Graduate Council:

I am submitting herewith a dissertation written by Christina Elizabeth Viviano entitled "Characterizing phyllosilicate distribution, abundance, and origin on Mars." I have examined the final electronic copy of this dissertation for form and content and recommend that it be accepted in partial fulfillment of the requirements for the degree of Doctor of Philosophy, with a major in Geology.

Jeffrey E. Moersch, Major Professor

We have read this dissertation and recommend its acceptance:

Harry Y. McSween, Devon M. Burr, Michael E. Essington

Accepted for the Council:

Carolyn R. Hodges

Vice Provost and Dean of the Graduate School

(Original signatures are on file with official student records.)

Characterizing phyllosilicate distribution, abundance, and origin on Mars

A Dissertation Presented for the
Doctor of Philosophy Degree
The University of Tennessee, Knoxville

Christina Elizabeth Viviano
May, 2012

Dedication

To my mom and dad.

Acknowledgements

It is a pleasure to thank those who I have learned a great deal from and whose work with me over the last five and a half years made this dissertation possible. First, I would like to thank my advisor, Dr. Jeffrey Moersch, for providing me with intellectually stimulating research and teaching opportunities. Jeff has guided and encouraged me to conduct research with a level of excellence and rigor that has challenged and improved my abilities as a scientist, writer, and presenter. I am grateful for his extraordinary efforts and support throughout my degree. I also wish to thank the members of my committee, Dr. Harry Y. McSween, Dr. Devon Burr, and Dr. Michael Essington, for their instrumental guidance in petrology and geochemistry, surface processes, and phyllosilicate mineralogy, and for their invaluable encouragement and assistance along the way.

I would like to thank the THEMIS team for their efforts in targeting scenes used in this work. I am grateful to Kristen Bell for her assistance with preprocessing of THEMIS scenes and Jen Piatek for her advice and expertise on THEMIS processing software. Ed Perfect gave useful suggestions on statistical analyses and Ted Labotka provided guidance on carbonate geochemistry calculations. Deanne Rogers had insightful advice on THEMIS atmospheric corrections and Vicky Hamilton shared laboratory glass spectra. This work was funded by Arizona State University subcontract #10-254 (under Jet Propulsion Laboratory contract #1224808) for Dr. Moersch's participation on the THEMIS Science Team.

Lastly, I would especially like to thank my friends and family who supported me personally; they have played an essential role in the culmination of my formal education. I wish to express a heartfelt thank you to Andrew Beck. I am ever grateful for his endless encouragement and invaluable collaboration throughout our time at UT. I'd also like to thank my unconditionally supportive siblings, Jessica, Giancarlo, and Franky. And finally, I am forever indebted to my parents, Frank and Jeanette, who encouraged me to pursue my interest in science from an early start and instilled the value of hard work, discipline, and motivation towards learning that was essential to the pursuit of this degree.

Abstract

Secondary phyllosilicates are hydrated minerals formed in the presence of liquid water. On Earth, their formation is often indicative of a neutral, water-rich environment, capable of supporting and preserving organic matter. However, different phyllosilicate species may be produced in different pH levels and water-to-rock ratios. The identification of mineralogically diverse phyllosilicates in small, localized exposures on Mars provides a complex record of their formation processes. While discrete outcrops of phyllosilicates have been previously identified in high-resolution visible/near-infrared hyperspectral images of Mars, regional coverage of these phyllosilicate-rich areas at better resolution is limited. Furthermore, spectra of minerals in the visible/near-infrared wavelength range do not mix linearly, and therefore it is difficult to determine their modal abundances. To better understand the geologic context of these deposits, I used the global coverage of the THEMIS thermal infrared multispectral imaging instrument to develop a technique for mapping new phyllosilicate deposits on Mars and present results from the Mawrth Vallis and Nili Fossae regions.

Unlike in the visible/near-infrared, spectra of minerals in the thermal infrared mix linearly and can therefore be unmixed to derive endmember abundance. At 100-m/pixel resolution, the THEMIS instrument is also more likely to detect surfaces with predominately phyllosilicate-rich materials, rather than the 3x5 km/pixel resolution of the TES instrument (also operating in the thermal infrared) which can easily dilute the spectral signature of phyllosilicate components with surrounding materials. Presented here are unmixing results from THEMIS data of the Mawrth Vallis region. Fe/Mg-rich phyllosilicates are modeled in abundances of up to 40-60%, while Al-rich phyllosilicates

are modeled at ~20-40%. Geochemical analysis suggests the alteration that occurred in the Mawrth Vallis region was not solely in-place weathering in a closed system.

Finally, phyllosilicate-bearing material in the Nili Fossae region associated with metamorphic assemblages is characterized, revealing evidence for the presence of a talc component. This spectral component is found to be associated with magnesium carbonates and olivine in Nili Fossae. We hypothesize that this relationship and the limited occurrence of serpentine associated with these units indicate carbonation of serpentine was a localized process in this region. If this carbonation reaction was a widespread phenomenon in other olivine-rich protoliths on Mars, it may have been an important process in the ancient Martian carbon cycle and could have provided a sink for CO_2 in the past.

Table of Contents

List of Tables

Part 2

Part 3

List of Figures

Part 2

Part 3

Part 4

Part 1
Introduction

In the last 30 years, missions to Mars have revealed compositions of the surface through in situ and remotely sensed observations. Mineral compositions preserve evidence for environmental conditions occurring throughout Martian history. The spectral identification of hydrated minerals is a key indicator for the presence of liquid water on the surface of Mars early in its history. Studying the nature, abundance, and distribution of hydrated minerals can further our understanding of the ancient Martian environment. Materials rich in hydrated minerals, such as clays, may have facilitated preservation of organic matter on Mars, if it existed [*Wattel-Koekkoek et al.*, 2003]. Therefore, in the search for Martian biomarkers, hydrated minerals are important as they indicate environments that had the potential to harbor or preserve the remains of life. For that reason, it is important to fully map the extent of hydrated minerals on the surface of Mars. The mapping and identification of these minerals will allow us to better understand the geologic context of their formation (e.g. in long-standing surface water, or hydrothermal alteration in the subsurface) and reveal whether processes forming these minerals occurred only in localized areas or globally.

1.0 CLAY MINERALOGY

Hydrated minerals, such as clay minerals, are chemical byproducts of interactions between water and common rock-forming minerals. Clay minerals are classified as phyllosilicates, or sheet silicates, which can be separated into different subgroups based on their compositions and structures. There are two sheet types that make up layered silicates: tetrahedrally coordinated sheets (T) and octahedrally coordinated sheets (O). The tetrahedrally coordinated sheets are comprised of linked silica tetrahedra commonly

substituted with aluminum, $(Si,Al)_2O_5$, and they share their apical oxygen with the octahedral sheet. Octahedral sheets commonly coordinate with cations such as Al, Mg, and Fe. Divalent cations in the octahedral sheet cause all of the octahedron sites to be occupied (trioctahedral sheets), $M^{2+}(OH)_2O_4$, whereas trivalent cations in the octahedral sites cause $2/3^{rd}$ of the sites to be occupied (dioctahedral sheets), $M^{3+}(OH)_2O_4$. Al substitution in the tetrahedral sheet causes excessive negative charge, which may be satisfied by interlayer cations and water.

Phyllosilicates are grouped by layer type and the unit layer charge (which is directly related to the amount of substitution in the tetrahedral and octahedral sheets). The main clay mineral groups are:

1) Kaolin and Serpentine group: 1:1 layer (T-O) e.g., kaolinite, dickite, nacrite, and halloysite (dioctahedral), and lizardite, crysotile, and antigorite (trioctahedral).

2) Mica group: 2:1 layer (T-O-T)

True micas: (layer charge $x > 0.85$) e.g., muscovite (dioctahedral), and biotite and phlogopite (trioctahedral).

Brittle micas: (layer charge $1.8 < x < 2.0$) e.g., chernykhite (dioctahedral), and clintonite (trioctahedral).

Interlayer deficient micas: (layer charge $0.6 \leq x < 0.85$) e.g., illite and glauconite (dioctahedral).

3) Chlorite group: 2:1 layer (T-O-T, +polymer interlayer) e.g., chamosite and clinochlore.

4) Vermiculite (Swelling Clay) group: 2:1 layer (layer charge $0.6 < x < 0.9$, T-O-T, expandable interlayer).

5) Smectite (Swelling Clay) group: 2:1 layer (layer charge $0.2 < x < 0.6$, T-O-T, expandable interlayer) e.g., montmorillonite, nontronite, and beidellite (dioctahedral), and saponite, and hectorite (trioctohedral).

6) Talc-Pyrophyllite group: 2:1 layer (layer charge $x \approx 0$, T-O-T, non-expansive) e.g., pyrophyllite (dioctahedral), and talc (trioctohedral).

The clay mineral type produced is dependent upon the source material composition (affecting solution chemistry), and also reflects differences in temperature, pressure, and the water-to-rock ratio during clay formation. Because of this, differences in clay species may help us define environments of clay formation on Mars. For example, clay mineralogy on Earth has been used as an indicator of paleoclimatic conditions. *Price et al.* [2000] found in the Speeton Clay Formation, kaolinite was the dominant clay mineral when paleotemperatures were high (representing humid conditions), and smectite was the dominant clay mineral when paleotemperatures were low (representing arid conditions). However, many clay minerals may be produced in a number of environments (e.g. montmorillonite can be found in sedimentary tropical climates through alteration of feldspar, as well as hydrothermal environments forming from volcanic glasses and tuffs).

2.0 SPECTROSCOPY OF PHYLLOSILICATES

In the visible and near-infrared wavelength region (λ=0.3-5 μm), clay minerals have absorption features due to water that is loosely bound in their structures (~1.4 and 1.9 μm) and the cation-hydroxyl bond in the octahedral layers (e.g. Al-OH in kaolinite).

Variations in the shape and wavelength of the ~2.2-2.3-μm X-OH bond absorption feature are due to the stretching plus bending vibrations due to specific cation(s) bonded to the hydroxyl. The precise wavelength position of the absorption feature depends on the type of octahedral cation and mineral structure. Al-OH by itself typically displays an absorption feature around 2.2 μm and varying degrees of Fe and Mg exchange lead to the absorption feature shifting to around 2.3 μm. The position of the OH overtone ~1.4 μm shifts from 1.38 to 1.42 μm for phyllosilicates based on the type of octahedral cation (Mg, Al, Fe) [*e.g.*, *Bishop et al.*, 2002].

In the thermal infrared wavelength (λ=5-50 μm), the primary spectral absorption feature for phyllosilicates derives from the fundamental vibrational mode of tetrahedral sheet Si-O stretching, resulting in a broad absorption feature between 900-1300 cm^{-1} (11.1–7.7 μm) [Keller and Pickett, 1950]. For most clay minerals, the Si-O stretching absorptions center at 1000-1100 cm^{-1} (9-10 μm) and the Si-O bending absorption feature is centered around 470 cm^{-1} (21 μm) [*Michalski et al*., 2006].

3.0 INITIAL DETECTION OF PHYLLOSILICATES ON MARS

The presence of phyllosilicates on Mars was first suggested by near-infrared ground-based spectral observations, which showed a weak but distinct 2.3-μm absorption feature, interpreted to be Mg-rich clay [*e.g.*, *McCord et al.*, 1982; *Singer et al.*, 1984; *Singer* 1985]. Also observed was a 2.2-μm absorption feature, interpreted as poorly crystalline aluminous phyllosilicate [*Murchie et al.*, 1993]. However, analysis of these features indicates crystalline clays are not a dominant component of the Martian surface [*Soderblom*, 1992]. Magnetic property experiments on Pathfinder suggested that dust in

the Martian atmosphere is consistent with claylike particle aggregates stained or cemented by iron oxides [*Hviid et al.*, 1997]. Viking 1 & 2 X-ray fluorescence spectroscopy suggested the presence of up to 80% Fe-rich clay [*Baird et al.*, 1976], consistent with nontronite [*Toulmin et al.*, 1977]. *In situ* measurements of the Martian meteorite collection reveal preterrestrial Fe-rich montmorillonite [*Gooding et al.*, 1991], Al-rich illite [*Gooding*, 1992], and smectites [*Treiman et al.*, 1993; *Bridges et al.*, 2001]. Clay (and other hydrated) minerals may explain the significant abundances of hydrogen mapped at low latitudes by the Mars Odyssey gamma ray and neutron experiments [*Boynton et al.*, 2002; *Feldman et al.*, 2002; *Bish et al.*, 2003] because shallowly buried liquid water or ice would not be stable under present conditions at these latitudes even when accounting for slopes [*e.g.*, *Aharonson and Schorghofer*, 2005]. Spectral data from the Thermal Emission Spectrometer (TES) on board the Mars Global Surveyor indicate the surface of Mars can be broadly divided into two spectral units: Surface Type 1 (ST1) and Surface Type 2 (ST2) [*Bandfield et al.*, 2000]. ST2 materials have been deconvolved with comparable fidelity using model compositions of basaltic andesite [*Bandfield et al.*, 2000] and [*Hamilton et al.*, 2001], and partly weathered basalt that includes a significant clay component [*Wyatt and McSween*, 2002]. Finally, the Mars Exploration Rover Spirit was used to identify major, minor, and trace element compositions, as well as spectroscopic signatures consistent with montmorillonite and kaolinite-type Al-rich phyllosilicates (or their compositional equivalents) in the Columbia Hills [*Clark et al.*, 2007; *Wang et al.*, 2006].

4.0 ESTABLISHED PHYLLOSILICATE MINERAL GROUPS ON MARS

The Observatoire pour la Mineralogie, l'Eau, les Glaces et l'Activité (OMEGA) on board the Mars Express spacecraft [*Bibring et al.*, 2004] and the Compact Reconnaissance Imaging Spectrometer for Mars (CRISM) on board the Mars Reconnaissance Orbiter [*Murchie, et al.,* 2007], have been used to identify the following phyllosilicates on Mars: Fe-rich smectite (e.g. nontronite), Al smectite (e.g. montmorillonite), Fe/Mg smectite (e.g. saponite), Al mica (e.g. muscovite or illite), chlorite group minerals, and kaolin group minerals [*Bibring et al*., 2009]. Serpentine and prehnite have been identified as well [*Ehlmann et al.*, 2009; *Ehlmann et al.* 2010]. The wavelengths of absorption features associated with these particular phyllosilicate species (as described in section 2.0) were used to identify each of the phases. The diversity of these weathering products implies wide-ranging environments of formation and source materials. For example, Fe-rich smectite (nontronite), as found in Nili Fossae, may be produced from olivine-rich source materials [*Hoefen et al*., 2003], whereas Al-rich clay members, in general, are thought to result from more pervasive alteration of basalt, or a more Al-rich igneous source [*Schiffman et al*., 2000].

5.0 COMPARISON OF INSTRUMENTS

THEMIS and TES are a multispectral imager and a spectrometer (respectively) operating in the thermal infrared at 672-1473 cm^{-1} and 200-1667 cm^{-1} (6.79-14.88 μm and 6-50 μm), respectively. The Mars Global Surveyor TES observed the planet for ~10 years, and Mars Odyssey THEMIS has been observing since 2002. Both OMEGA and CRISM detect in the visible and near-infrared portions of the spectrum (0.362-9.92 μm

and 0.35-5.2 μm, respectively). Mars Express OMEGA began its science phase in 2004, and Mars Reconnaissance Orbiter CRISM in 2006. TES and THEMIS have superior global coverage of the Martian surface compared to high resolution OMEGA and CRISM imagery for several reasons: the footprints of CRISM scenes are much smaller (due to higher spatial resolution) and CRISM and OMEGA data volumes are very high (due to the higher number of bands). TES has a spatial resolution of 3x5 km/pixel and 144 bands (72 of which are useful for surface science after data have been corrected). THEMIS has much better spatial resolution, 100 m/pixel, but a lower spectral resolution, with only 8 unique bands that are sensitive to the surface. The OMEGA instrument has a spatial resolution ranging from 350-10000 m/pixel, due to its elliptical orbit, and a spectral resolution of 352 bands or 400 bands. CRISM can be targeted with a high spatial resolution of 18 or 36 m/pixel and has a survey mode at 100 or 200 m/pixel. While CRISM coverage in survey mode is over half the planet, the coverage at a resolution of 18 or 36 m/pixel is less than 5%, thus far. The spectral resolution is comparable to OMEGA, at 72 bands or 544 bands. 470 cm^{-1} (21 μm) [*Michalski et al*., 2006].

6.0 DATASET DISCREPANCIES AND MOTIVATION

Phyllosilicates observed on Mars thus far have been well mapped in ~10 km^2 locations with high-resolution CRISM data, yet less than 5% of the globe has been covered. The extent of phyllosilicate-bearing outcrops mapped at <100 m/pixel resolution is not well established as coverage is limited. The locations of phyllosilicate-bearing outcrops that have been identified may be used to calibrate an index for mapping the full extent of phyllosilicates at 100 m/pixel with the THEMIS instrument. As

THEMIS and TES detect in the thermal infrared wavelength range, spectral endmembers mix linearly and thus abundance may be determined. Modeling of phyllosilicate-bearing material with the TES dataset results in abundances at or near the instrument limit of detection [*e.g.*, *Michalski and Fergason*, 2009]. This discrepancy is perhaps due to the spatial resolution (~3 km/pixel) of the TES instrument, and not characteristics of the phyllosilicates themselves (see Chapter 3). Therefore, the 100 m/pixel spatial resolution of the THEMIS instrument may be utilized to determine abundance of phyllosilicate-bearing deposits. Finally, the composition of the phyllosilicates may be further determined by analysis of spectral features, particularly those in the visible and near-infrared wavelength range. In Chapter 4, phyllosilicate minerals associated with metamorphic phases in the Nili Fossae region are further characterized and mapped by using spectral ratios that emphasize absorption features present in phyllosilicates measured in the laboratory setting. Determining specific clay species helps to constrain environment of formation, and in this case metamorphic conditions.

REFERENCES

Baird, A. K., et al. (1976), Mineralogic and Petrologic Implications of Viking Geochemical Results from Mars - Interim-Report, Science, 194(4271), 1288-1293.

Bandfield, J. L., et al. (2000), A global view of Martian surface compositions from MGS-TES, Science, 287(5458), 1626-1630.

Banin, A., and J. Rishpon (1979), Smectite Clays in Mars Soil - Evidence for Their Presence and Role in Viking Biology Experimental Results, Journal of Molecular Evolution, 14(1-3), 133-152.

Banin, A., et al. (1988), Laboratory Investigations of Mars - Chemical and Spectroscopic Characteristics of a Suite of Clays as Mars Soil Analogs, Origins of Life and Evolution of the Biosphere, 18(3), 239-265.

Bibring, J. P., et al. (2004), OMEGA: Observatoire pour la Mineralogie, l'Eau, les Glaces, et l'Activite, in Mars Express: The Scientific Payload, Wilson, A. (Ed.), ESA Publications Division, Noordwijk, 37-49.

Bibring, J. P., et al. (2006), Global mineralogical and aqueous mars history derived from OMEGA/Mars express data, Science, 312(5772), 400-404.

Bibring, J. P., et al. (2009), Martian Phyllosilicates: Recorders of Aqueous Processes: Discussion Summary, Institut d'Astrophysique Spatiale, http://www.ias.upsud.fr/Mars_Phyllosilicates/phyllo/5.%20Thursday%20morning/Phyllo_Discussion_summary.ppt

Bishop, J. L., E. Murad, and M. D. Dyar (2002), The influence of octahedral and tetrahedral cation substitution on the structure of smectites and sperpentines as observed through infrared spectroscopy, Clay Miner., 37, 617-628.

Bishop, J. L., et al. (2008), Phyllosilicate diversity and past aqueous activity revealed at Mawrth Vallis, Mars, Science, 321(5890), 830-833.

Buczkowski, D. L., et al. (2008), CRISM analyses of Argyre Basin, LPSC XXXIX, #1030.

Clark, B. C. et al. (2007), Evidence for montmorillonite or its compositional equivalent in Columbia Hills, Mars, J. Geophys. Res, 112, E06S01, doi:10.1029/2006JE002756.

Ehlmann, B. L., et al. (2008), Clay minerals in delta deposits and organic preservation potential on Mars, Nature Geoscience, 1(6), 355-358.

Ehlmann, B. L., et al. (2009), Identification of hydrated silicate minerals on Mars using MRO-CRISM: Geologic context near Nili Fossae and implications for aqueous alteration, *J. Geophys. Res.*, *114*, E00D08, doi:10.1029/2009JE003339.

Ehlmann, B. L., J. F. Mustard, and S. L. Murchie (2010), Geologic setting of serpentine deposits on Mars, Geophys. Res. Lett., 37, L06201, doi:10.1029/2010GL042596.

Gooding, J. L., et al. (1991), Aqueous Alteration of the Nakhla Meteorite, Meteoritics, 26(2), 135-143.

Gooding, J. L. (1992), Soil Mineralogy and Chemistry on Mars - Possible Clues from Salts and Clays in Snc Meteorites, Icarus, 99(1), 28-41.

Hamilton, V. E., et al. (2001), Analysis of terrestrial and Martian volcanic compositions using thermal emission spectroscopy - 2. Application to Martian surface spectra from the Mars Global Surveyor Thermal Emission Spectrometer, Journal of Geophysical Research-Planets, 106(E7), 14733-14746.

Hoefen, T. M., et al. (2003), Discovery of Olivine in the Nili Fossae Region of Mars, Science, 302(5645), 627-630.

Michalski, J. R., et al. (2006), Emission spectroscopy of clay minerals and evidence for poorly crystalline aluminosilicates on Mars from Thermal Emission Spectrometer data, Journal of Geophysical Research-Planets, 111(E3).

Michalski, J. R. and R. L. Fergason (2009), Composition and thermal inertia of the Mawrth Vallis region of Mars from TES and THEMIS data, *Icarus*, *199*, 25-48.

Murchie, S., et al. (2007), Compact Reconnaissance Imaging Spectrometer for Mars (CRISM) on Mars Reconnaissance Orbiter (MRO), Journal of Geophysical Research-Planets, 112(E5).

Murchie, S. L., et al. (2009), A synthesis of Martian aqueous mineralogy after 1 Mars year of observations from the Mars Reconnaissance Orbiter, J. Geophys. Res., 114, E00D06, doi:10.1029/2009JE003342.

Mustard, J. F., et al. (2007), Mineralogy of the Nili Fossae region with OMEGA/Mars Express data: 1. Ancient impact melt in the Isidis Basin and implications for the transition from the Noachian to Hesperian, Journal of Geophysical Research-Planets, 112(E8).

Mustard, J. F., et al. (2008), Hydrated silicate minerals on mars observed by the Mars reconnaissance orbiter CRISM instrument, Nature, 454(7202), 305-309.

Osterloo, M. M., et al. (2008), Chloride-bearing materials in the southern highlands of Mars, Science, 319(5870), 1651-1654.

Pelkey, S. M. et al. (2007), CRISM observations of hydrated crater deposits in Tyrrhena Terra, Mars, LPSC XXXVIII, #1994.

Poulet, F., et al. (2005), Phyllosilicates on Mars and implications for early martian climate, Nature, 438(7068), 623-627.

Price, G.D., et al. (2000), Isotopic evidence for temperature variation during the early Cretaceous (late Ryazaniann-mid-Hauterivian), Journal of the Geological Society, London, 157, 335-343.

Schiffman, P. et al. (2000), Controls on palagonitization versus pedogenic weathering of basaltic tephra: Evidence from the consolidation and geochemistry of the Keanakako'i Ash Member, Kilauea Volcano, Geochemistry Geophysics Geosystems, 1(18), 1040-1056.

Toulmin, P., et al. (1977), Geochemical and Mineralogical Interpretation of Viking Inorganic Chemical Results, Transactions-American Geophysical Union, 58(8), 828-828.

Wattel-Koekkoek, E. J. W., et al. (2003), Mean residence time of soil organic matter associated with kaolinite and smectite, European Journal of Soil Science, 54(2), 269-278.

Wang, A., et al. (2006), Evidence of phyllosilicates in Wooly Patch, an altered rock encountered at West Spur, Columbia Hills, by the Spirit rover in Gusev crater, Mars, J. Geophys. Res., 111, E0216, doi:10.1029/2005JE002516.

Wray, J. et al. (2008), Hydrated mineral exposures in the Southern Highlands, Workshop on Martian Phyllosilicates: Recorders of Aqueous Processes?, #7018.

Wyatt, M. B., and H. Y. McSween (2002), Spectral evidence for weathered basalt as an alternative to andesite in the northern lowlands of Mars, Nature, 417(6886), 263-266.

Part 2
A Technique for Mapping Fe/Mg-rich Phyllosilicates on Mars using THEMIS Multispectral Thermal Infrared Images

This part is a reformatted version of a paper of the same name submitted to the Journal of Geophysical Research (Planets) in October, 2011. Christina Viviano and Jeff Moersch wrote this paper.

Viviano, C. E. and Moersch, J. M. (submitted) A Technique for Mapping Fe/Mg-rich Phyllosilicates on Mars using THEMIS Multispectral Thermal Infrared Images, *J. Geophys. Res*.

Abstract

We present a method for mapping exposures of Fe/Mg-rich phyllosilicates on the Martian surface using THEMIS daytime multispectral thermal infrared images. The primary utility of this technique comes from the fact that THEMIS coverage is near-global at 100 m/pixel, so it offers the opportunity to extend and improve upon phyllosilicate maps created using CRISM and/or OMEGA near-infrared data alone. The spectral index formulation used for this mapping consists of a sum of spectral band ratios, weighted in different proportions. An initial formulation of the index was determined using a suite of synthetic spectra containing varying proportions of a Martian basalt spectrum and a laboratory phyllosilicate spectrum. A scene-specific formulation was then optimized by exploiting the correlation between pixels the initial formulation flags in each THEMIS scene as containing phyllosilicates and those identified in overlapping CRISM data. Once the optimal formulation of the index is determined, it is applied to the entire THEMIS scene, extending the map of phyllosilicates beyond the area of overlapping CRISM coverage. The method is illustrated using 12 THEMIS scenes from the Mawrth Vallis and Nili Fossae regions. The new THEMIS-derived maps of Fe/Mg-rich phyllosilicates in these two regions have approximately double the coverage provided by CRISM data. The cross-wavelength and cross-instrument approach we use to derive phyllosilicate indices for THEMIS data could potentially be used to define

spectral indices for mapping other compositions of interest on Mars that possess spectral features in more than one spectral region.

1.0 INTRODUCTION

In the past three decades, missions to Mars have revealed surface compositions through *in situ* and remotely sensed observations. Because liquid water is unstable in the current Martian surface temperature and pressure regime, the spectral identification of hydrated minerals has been a key piece of evidence for the presence of liquid water on the surface of Mars early in its history. The implications of such minerals for past climate conditions on Mars are not well constrained: was liquid water stable at the surface on geologic timescales, or was it ephemeral? Was persistent water interaction a widespread phenomenon, or was the extent of this activity limited spatially? The nature, abundance, and distribution of hydrated minerals, such as clay minerals, preserve evidence for the conditions that existed in the ancient Martian environment. The identification and mapping of these minerals allows us to better understand the geologic context of their formation (*e.g.*, in long-standing surface water, or hydrothermal alteration in the subsurface) and reveals whether formation processes were localized or global. Furthermore, terrestrial clay minerals are known to have long crustal residence times, low permeability upon burial, and binding properties that can trap organic molecules to charged surfaces, important for the preservation of biosignatures [*e.g.*, *Farmer and Des Marais*, 1999], so understanding their distribution on Mars can guide future exploration of sites where potential biosignatures may be preserved. Generally, clay minerals (a hydrous aluminum-bearing subset of phyllosilicates, generally <2 μm) result from

alteration of silicate-rich rocks by aqueous solutions. Significant phyllosilicate deposits constrain past Martian environments because their presence indicates long-term contact between liquid water and rock [*e.g.*, Velde et al. 1995].

1.1. Near-infrared identification of phyllosilicates from orbit

In the visible and near-infrared wavelength region (λ = 0.3-5.0 μm), clay minerals have absorption features (~1.4 and 1.9 μm) due to water that is loosely bound in their structures and the cation-hydroxyl bond in the octahedral layers (*e.g.*, Al-OH in kaolinite). Variations in the shape and wavelength of the ~2.2-2.3-μm X-OH absorption feature and the ~1.4-μm X-OH overtones are due to the specific cation(s) (X) bonded to the hydroxyl. Al-OH by itself typically displays an absorption feature around 2.2 μm and varying degrees of Fe and Mg exchange lead to the absorption feature shifting to ~2.3 μm [*e.g.*, *Clark et al.*, 1990; *Bishop et al.*, 2002].

The distribution and compositions of phyllosilicates on Mars is currently being mapped and measured using the Observatoire pour la Mineralogie, l'Eau, les Glaces et l'Activité (OMEGA) [*Bibring et al.*, 2004] instrument on board Mars Express, and the Compact Reconnaissance Imaging Spectrometer for Mars (CRISM) on board the Mars Reconnaissance Orbiter [*Murchie, et al.*, 2007a]. Both OMEGA and CRISM include the visible and near-infrared portions of the spectrum (0.362-9.92 μm and 0.35-5.2 μm, respectively). The OMEGA instrument has a spatial resolution ranging from 350-10,000 m/pixel (targeted vs. survey mode) and a spectral resolution of 352 bands or 400 bands. CRISM can acquire data in a targeted mode with a high spatial resolution of 18 or 36 m/pixel in 544 bands, or in one of two survey modes at 100 or 200 m/pixel in 72 bands.

While CRISM's 200 m/pixel survey mode has mapped over half the planet, less than 5% has been covered at better spatial resolution thus far.

OMEGA and CRISM have been used to identify several sites bearing evidence for phyllosilicates. One of the largest exposures of clay minerals is found in Mawrth Vallis, where initially OMEGA was used to detect Fe/Mg- and Al-rich smectites [*Poulet et al.*, 2005; *Loizeau et al.*, 2007]. These detections were confirmed by CRISM spectral observations, which showed evidence for kaolinite, hectorite, and hydrated silica [*e.g.*, *Bishop et al.*, 2008]. OMEGA-identified Fe-rich phyllosilicates, specifically smectites, have also been observed in a large exposure around the Nili Fossae region [*e.g.*, *Poulet et al.*, 2005; *Mangold et al.*, 2007]. CRISM observations have been used to identify other phyllosilicate species in this region, such as chlorite, kaolinite, illite (or muscovite), prehnite, and serpentine [*e.g.*, *Mustard et al.*, 2008; *Ehlmann et al.*, 2008; *Ehlmann et al.*, 2009; *Ehlmann et al.*, 2010].

1.2. Thermal infrared detection of phyllosilicates

In the thermal infrared (TIR) (λ = 2000-200 cm^{-1} or 5-50 μm), the primary spectral absorption feature for phyllosilicates derives from the fundamental vibrational mode of tetrahedral sheet Si-O stretching, resulting in a broad absorption feature at 1300-900 cm^{-1} (7.7-11.1 μm) [*Keller and Pickett*, 1950]. For most phyllosilicates, the Si-O stretching absorptions center at 1100-1000 cm^{-1} (9.1-10 μm) and the Si-O bending absorption feature is centered near 470 cm^{-1} (~21 μm) [*Michalski et al.*, 2006b].

The Mars Global Surveyor Thermal Emission Spectrometer (TES) [*Christensen et al.*, 2001] operated in the TIR from 1667-200 cm^{-1} (6-50 μm). The TES experiment provided ~10 Earth years of data and global coverage of Mars. TES had a spatial

resolution of ~3x5 km/pixel and 144 bands (72 of which are useful for inferring surface compositions after the data have been atmospherically corrected). Analyses of TES data indicate that the surface of Mars can be broadly divided into two spectral units known as Surface Type 1 (ST1) and Surface Type 2 (ST2) [*Bandfield et al.*, 2000]. ST1 material has been shown to be consistent with basalt and is largely located in the southern highlands [*e.g.*, *Bandfield et al.*, 2000]. ST2 materials, mainly found in the northern lowlands, have been deconvolved using model compositions of basaltic andesite [*Bandfield et al.*, 2000; *Hamilton et al.*, 2001], or alternatively using weathered basalt that includes a significant clay component and high-silica volcanic glass [*Wyatt and McSween*, 2002]. However, silica-rich and poorly crystalline phases [*Wyatt and McSween*, 2002], palagonitic alteration [*Morris et al.*, 2003], silica-rich rock coatings [*Kraft et al.*, 2003], zeolites [*Ruff*, 2004] and poorly crystalline aluminosilicates [*Michalski et al.*, 2005] have also been proposed as possible explanations for the spectrally amorphous component of the TES ST2 spectrum. The clay mineral doublet absorption feature at 530 and 465 cm^{-1} (18.9 and 21.5 μm) has been used to develop two spectral indices for mapping dioctahedral smectites on Mars using TES data [*Ruff and Christensen*, 2007].

The Mars Odyssey THermal Emission Imaging System (THEMIS) [*Christensen et al.*, 2004] is a 100 m/pixel multispectral imager that observes the surface in eight unique bands in the TIR at 1473-672 cm^{-1} (6.79-14.9 μm). THEMIS has greater (near-global) coverage of the Martian surface compared to CRISM, especially CRISM data at comparable or better spatial resolution than THEMIS. Though THEMIS spectra have not been used to uniquely identify phyllosilicates on Mars, *McDowell and Hamilton* [2009]

showed that THEMIS spectra of material in Nili Fossae displays characteristics consistent with a mixture including a phyllosilicate phase. It has also been shown that a decorrelation stretch (DCS) [*Gillespie et al.*, 1986] of THEMIS data reveals subtle compositional variation between the OMEGA- and CRISM-identified phyllosilicate-bearing terrain and surrounding material within Mawrth Vallis and Nili Fossae [*Michalski et al.*, 2006a; *Michalski and Fergason*, 2009; *McDowell and Hamilton*, 2009]. A DCS maximizes the variation within a single band, but only utilizes 3 bands for a given stretch, not the full THEMIS spectrum. Furthermore, the result of a DCS is rather qualitative and provides no indication of confidence in a particular observation, such as a threshold value to indicate presence or absence of a particular phase. While these studies have noted THEMIS spectral discriminability in phyllosilicate-bearing terrain, the present study is the first to quantify this behavior on a regional scale in Mawrth Vallis and Nili Fossae, and utilize it to map the presence or absence of phyllosilicates with the THEMIS instrument. This provides a one-to-one comparison with CRISM phyllosilicate mapping results, which allows for better assessment of the correlation between the two datasets and spectral regions.

1.3. Motivation

The objective of this study is to derive an optimal method for mapping phyllosilicates on the Martian surface using THEMIS data. This objective is accomplished through derivation of custom-tailored spectral indices that are sensitive to the presence of phyllosilicates in different THEMIS scenes. Areas where CRISM has detected phyllosilicates are used as "training areas" to help guide the derivation of these THEMIS spectral indices. The general formulation of an index is referred to here as a

THEMIS Phyllosilicate Index (*TPI*). The motivation for developing these indices is that they will enable regional-scale mapping of phyllosilicates on Mars, utilizing the near-global coverage of THEMIS. Regional distribution maps of phyllosilicates on Mars at 100 m/pixel would better constrain the age and location of materials that were once in environments suitable for producing these minerals (assuming they are produced in-place, or can be traced back to their source materials). These maps would help address the hypothesis that the history of Mars included an early "phyllosian" era, dominated by nonacidic aqueous alteration [*Bibring et al.*, 2006]. The detection of new locations of phyllosilicate-rich materials within a particular region would also provide information useful for future landing site assessments and targeting of higher spatial/spectral-resolution spectroscopy. Although TES has a much higher spectral resolution than THEMIS and is able to resolve different mineral species more readily, the high spatial resolution of THEMIS is useful for phyllosilicate detection because small exposures of phyllosilicates surrounded by other surface materials can be too spectrally muted to detect at the coarser spatial resolution of TES. Sub-pixel mixing of phyllosilicate-rich and poor surfaces with differing temperatures may account for discrepancies between the TES and OMEGA/CRISM detections of phyllosilicates [*Michalski and Fergason*, 2009] and THEMIS spatial resolution may be useful in addressing this factor [*Viviano and Moersch*, 2011]. Furthermore, as the thermal infrared is mostly sensitive to the Si-O stretching absorptions in the tetrahedral sheet of a phyllosilicate, whereas the near-infrared is sensitive to X-OH bonds in the octahedral sheet, high resolution thermal infrared mapping of phyllosilicates comparable to existing near-infrared mapping provides a larger picture of the mineralogic structure of phyllosilicate on Mars.

2.0 DATA AND METHODS

2.1. Thermal infrared data processing

*TPI*s were developed using THEMIS infrared scenes from within the Mawrth Vallis and Nili Fossae regions of Mars, where the OMEGA and CRISM datasets reveal strong detections of phyllosilicates. TES spectra of the same regions are used to remove atmospheric contributions from THEMIS data [*Bandfield et al.*, 2004a] because the atmospheric removal process for TES data is well understood and aided by higher spectral resolution of TES. This correction was implemented using the jENVI software package (http://arsia.gg.utk.edu/~utmars/jenvi), which performs the atmospheric correction technique outlined by *Bandfield et al.*, [2004a]. The correction works by calculating scaling and offset factors for each band that make THEMIS spectra of a spectrally homogeneous training area match an atmospherically-corrected TES surface spectrum (deconvolved to THEMIS bandpasses) of the same area. These scaling and offset factors are then applied to the entire THEMIS scene to remove the effects of the atmosphere. This procedure assumes a relatively constant elevation and atmospheric opacity across the scene [*e.g.*, *Bandfield et al.* 2004a], so training areas were chosen at similar elevation to phyllosilicate-bearing terrain. THEMIS daytime infrared images with the highest temperatures (a minimum of 240 K) and the lowest atmospheric dust and water ice opacities (both less than 0.15), were chosen to maximize the signal-to-noise ratios in the scenes.

2.2. Visible and near-infrared data processing

CRISM full-resolution targeted (FRT) and multispectral/push-broom survey (MSP) 200 m/pixel data were processed and read using the CRISM Analysis Toolkit

(CAT) interface (http://pds-geosciences.wustl.edu/missions/mro/crism.htm#Tools). Data were converted to I/F (a ratio of measured radiance to the incoming solar flux) using the procedures described by *Murchie et al.* [2007a, 2007b]. The I/F values were divided by the cosine of the incidence angle as a simple photometric correction to provide an approximation of reflectance. The data were atmospherically corrected by comparing the depth of the atmospheric 2-μm CO_2 feature in the scene to that of an atmospheric transmission spectrum derived from a ratio of the spectra from the top and base of Olympus Mons. The 2-μm feature in the scene is fitted to the Olympus Mons atmospheric spectrum and extrapolated to determine the atmospheric transmission at all wavelengths using the automated CAT interface. The supplemental materials in *Langevin et al.* [2006] give a full discussion of this correction. A spectral and spatial noise removal routine was also applied to the data [after *Parente*, 2008]. Spectral parameters from *Pelkey et al.* [2007] were applied to the corrected CRISM images to map phyllosilicates. These spectral indices are particularly sensitive to the 1.9-μm water feature, as well as the X-OH spectral features between 2.1-2.4 μm (where X is typically Al^{3+}, Mg^{2+}, Fe^{2+}, or Fe^{3+}). Specific clay species (Fe/Mg-OH vs. Al-OH) were identified using the D2300 parameter (drop at 2.3 μm) and the BD2210 parameter (band depth at 2.21 μm) [*Pelkey et al.*, 2007].

2.3. Development of THEMIS phyllosilicate indices

Our desire to develop spectral indices using THEMIS data is prompted by recognition of the fact that phyllosilicates have significant spectral features in the TIR portion of the spectrum (see section 1.2) resolvable at THEMIS spectral resolution. Figure A1c shows a suite of synthetic spectra computed by adding together Mars

background material (for this we use TES spectral type ST1) with varying amount of representative Fe/Mg-smectites. ST1 (basalt-like) material provides a reasonable composition for background material as it dominates the southern highlands [*e.g.*, *Bandfield et al.*, 2000], where the Mawrth Vallis and Nili Fossae regions are located. ST2 material is mostly highly concentrated in areas associated with the phyllosilicate-bearing areas identified by OMEGA and CRISM detections in the Mawrth Vallis region [*Rodgers and Bandfield*, 2010]. Thus, ST2 material was similarly mixed with varying amounts of representative smectite spectra for comparison. The result when using a mixture of smectite with ST2 material versus a mixture of smectite with ST1 material was not significantly different. The spectra used to derive these representative Fe/Mg-smectite spectra were computed from an average of all coarse-grained lab spectra of these families of smectites, from the Arizona State University (ASU) Thermal Emission Spectroscopy Laboratory Spectral Library [*Christensen et al.*, 2000] and all the fine-grained Fe/Mg-smectite spectra taken in bidirectional mode from the Johns Hopkins University (JHU) Mineral Spectral Library [*Salisbury et al.*, 1991] (converted to reflectance using Kirchhoff's Law, $\varepsilon = 1 - R$), resampled using the THEMIS band [*Christensen et al.*, 2004]. Strictly speaking, Kirchoff's Law is only valid for directional hemispherical data [*Salisbury et al.*, 1992]; however, *Mustard and Hays* [1997] have shown that bidirectional measurements are comparable to directional hemispherical for fine particle sizes. Thus, fine particles sizes from the JHU library were used. The following six samples from the ASU and JHU library were used: nontronite 589 (WAR-5108), smectite 592 (SWa-1), saponite 579, nontron.1, smectite.1, and saponite.1 (shown in Figure A1a and A1b).

The synthetic suite exhibits an increase in slope between band 6 (10.21 μm) and band 7 (11.04 μm) with the addition of smectite, as previously described by *McDowell and Hamilton* [2009], as well as an increase in slope between band 5 (9.35 μm) and band 6. Absorption related to X-OH bonds (where X=Fe^{2+}, Fe^{3+} Al^{3+}, and Mg^{2+}) in the octahedral sheet fall between 10.5-33 μm and can be used to distinguish between major spectral classes of clay (magnesian, aluminous, or ferruginous) at TES spectral resolution [*Michalski et al.*, 2006b]. The Fe-OH absorption features falls at ~12.2 μm (between band 8 and 9) and ~10.6-10.9 μm (between band 6 and 7), respectively [*e.g., Madejová and Komadel*, 2001], accounting for the subtle differences in the trends between both suites at THEMIS resolution. Complicating this relationship is the structure of the clay minerals. Ferruginous and magnesian clays may be either di- or trioctahedral, whereas aluminous clays are solely dioctahedral. If the clay is dioctahedral, the Si-O stretching absorption occurs at longer wavelengths than trioctahedral clays. For example, the Si-O stretching absorption of nontronite spectra occur at longer wavelength than the other Fe/Mg-rich smectite spectra plotted in Figure A1a, since nontronite is a dioctahedral smectite. Tetrahedral substitution of Al for Si results in a similar effect, shifting the Si-O stretching absorption to longer wavelengths [*e.g.*, *Michalski et al.*, 2005]. These two factors may not be resolvable, particularly at THEMIS spectral resolution. Since the near-infrared is only sensitive to octahedral sheet chemistry, relatively little is known about the tetrahedral sheet chemistry of Martian clays at high spatial resolution. With this limitation in mind, we have chosen both dioctahedral and trioctahedral samples to incorporate into our representative Fe/Mg-rich smectite spectra.

2.3.1. General formulation of a THEMIS spectral index

Our objective is to derive a spectral index consisting of different band ratios (each weighted by a different coefficient) that, when applied to an unknown THEMIS spectrum, indicates the presence or absence of phyllosilicates. This equation thus has the general mathematical form of:

$$Index = \sum_{i=1}^{n-1} \sum_{j=i+1}^{n} C_{(i,j)} \frac{\varepsilon_i}{\varepsilon_j} , \quad (1)$$

where ε_i or ε_j is the emissivity of a spectrum at a particular band and *n* is the number of bands. Equation 1 is the summation of all possible unique ratios of different bands, each with its own weighting coefficient $C_{(i,j)}$. In practical usage, a subset of the terms in equation 1 is used for THEMIS spectral indices; B1, B2, B3 and B10 are excluded because those bands are either too noisy, used as a normalization in the atmospheric correction, or insensitive to the spectral nature of the surface. Thus, the spectral index takes the following form:

$$THEMIS\ Index = \sum_{i=4}^{8} \sum_{j=i+1}^{9} C_{(i,j)} \frac{\varepsilon_i}{\varepsilon_j} . \quad (2)$$

Equation 2 is the summation of 15 terms consisting of band ratios from the usable THEMIS bands multiplied by their associated unique weighting coefficients. In section 2.3.2, we further restrict our formulation to only include those terms that are demonstrably sensitive to the presence of phyllosilicates.

A two-step process was used to find the band ratios (and their associated weighting coefficients) that are statistically sensitive to the presence of the group of phyllosilicates under consideration. An initial formulation (section 2.3.2) was made

using an evaluation of laboratory spectra synthetically mixed with Mars background material (shown in Figure A1c). Analysis of the variability of band ratios for these spectra allowed us to determine which band ratios were useful. This formulation was used as a "seed" in the second step (section 2.3.3), in which the weighting coefficients for these band ratios were mathematically optimized using real THEMIS spectra from Mars.

2.3.2. Initial formulation of a *TPI* based on analysis of lab spectra

Our first task was to determine which band ratios, and in what weighting, best characterize the spectral shapes of the two types of smectites as expressed in a mixture with "typical" Martian material. To evaluate the potential utility of a candidate band ratio, we compared the variability of that band ratio in laboratory spectra of a family of smectites (*e.g.*, all Fe/Mg-rich smectites) to the total variability of the same band ratio in the synthetic suite of Mars spectra shown in Figure A1c. If the total variability of the candidate band ratio in the synthetic suite is greater than the variability of the same ratio in the family of lab spectra, we considered this ratio significant in characterizing the shape of a mixed spectrum containing that type of smectite, and included that band ratio as a term in our formulation of the spectral index. To avoid undue influence by "outliers" in the family of lab spectra, we used the standard deviation of a candidate band ratio as our representation of that ratio's variability. The standard deviation helps to ensure that only those band ratios that are characteristic of the smectite family, as opposed to individual samples, were used in the formulation of the index. Initial weighting coefficients for the selected band ratios were set to the total variability of the band ratios in the suite of synthetic Mars spectra, and then were normalized so that the sum of all weighting coefficients equals one.

Table 1 shows the results of the approach described above for the initial formulation of *TPI* sensitive to Fe/Mg-rich smectite, hereafter referred to as ${}^{0}TPI_{Fe/Mg}$. Column 2 reports the total variability for each candidate band ratio in the synthetic suite of Mars spectra, for the mixture of ST1 with Fe/Mg-rich smectite. Column 3 indicates the 1-σ standard deviation of each possible band ratio's variability in the lab spectra for the family of smectite. Values in column 3 that are greater than the associated value for column 2 are shown in bold, indicating these ratios are characteristic of that family of clay spectra. The values in bold are then normalized to one and used as weighting coefficients for ${}^{0}TPI_{Fe/Mg}$ (reported in column 4). The result of this laboratory-based analysis is an initial *TPI* consisting of the summation of the band ratios weighted with the values reported in column 4 of this table. This initial formulation was used as a "seed", or initial guess, for optimization of the band ratio weighting coefficients using the iterative technique described in the following section.

2.3.3. Optimization of weighting coefficients with THEMIS spectra from Mars

While ${}^{0}TPI_{Fe/Mg}$ is determined through an analysis of laboratory spectra, we found that the subtle differences in actual spectral shapes of clays mixed with other compositions on the Martian surface significantly affect the weighting coefficients needed to optimally identify clays in THEMIS spectra. The left panel of Figure A2 presents an example map of Fe/Mg-rich phyllosilicates using ${}^{0}TPI_{Fe/Mg}$ described in section 2.3.2. The middle panel of Figure A2 presents a map of the same region using a refined formulation, referred to as $TPI_{Fe/Mg}$, optimized as described below. A visual comparison of these two THEMIS-based results to a CRISM D2300 parameter map of the same area (Figure A2, right panel) illustrates the improvement in sensitivity gained by

optimizing the weighting coefficients using actual spectra from a particular region of Mars, as described below.

Optimization of the weighting coefficients was achieved by maximizing the correlation between *TPI* values resulting from a trial formulation and associated CRISM D2300 values for the same locations. CRISM MSP scenes and THEMIS scenes were paired by location, as listed in Table 2, and filtered to include only the regions that have geographic overlap between the two datasets. For the most robust results, we only used THEMIS images with dust and water ice opacities below 0.15, average surface temperatures greater than 245 K, and preferred images with high image quality ratings (5 or greater) in the PDS database (http://themis-data.asu.edu). The THEMIS scenes were spatially degraded to 200-m/pixel resolution, the resolution of the CRISM MSPs. MSP data were used rather than higher resolution FRT data because MSP data have greater geographic coverage of both clay-rich and clay-poor surfaces to compare with each THEMIS scene, and to provide more data (allowing for better statistics) for each THEMIS-CRISM pairing. Coefficients for the band ratios in $TPI_{Fe/Mg}$ were optimized by reference to the CRISM D2300 parameter. Following the method of *Ehlmann et al.* [2009] we have linearly scaled the CRISM D2300 parameter maps to account for non-compositional factors that vary from scene to scene. We have set our scaling values such that a D2300 parameter value of zero or less corresponds to no detection of clay, based on visual examination of the 2.3 μm band depth relative to band-to-band noise for 3-5 regions of interest for each CRISM scene.

Our optimization method relies on correlating the magnitude of the CRISM D2300 value to the output of a candidate $TPI_{Fe/Mg}$ formulation. The method is dependent

upon the assumption that higher CRISM D2300 values ought to correspond to locations where values of an optimized $TPI_{Fe/Mg}$ are also higher. The process is iterated with many candidate $TPI_{Fe/Mg}$ formulations until an optimal combination of band ratio coefficients for $TPI_{Fe/Mg}$ is achieved – *i.e.*, the correlation with the CRISM D2300 values is maximized. This optimization may be thought of in graphical terms as a scatter plot of points, each point in the plot representing a physical location on the surface. The locations are ordered along the abscissa according to increasing D2300 parameter values. The ordinate values of the points are the values of a given by a trial $TPI_{Fe/Mg}$ formulation for the same locations (see example, Figure A3a). A steeper slope of points (with relatively low scatter) on this plot indicates a better-optimized trial formulation of $TPI_{Fe/Mg}$. An automated routine iterates with variable magnitudes of band ratio coefficients until an optimized formulation of $TPI_{Fe/Mg}$ is achieved (see description below of 'MPFIT').

For each iteration of the optimization process, a trial formulation of $TPI_{Fe/Mg}$ is used to calculate an index value for each pixel in the THEMIS scene. These values were plotted on an ordered scatter plot as described above. The index variable x is used to represent the position of a given THEMIS pixel in this ordering. An example of one of these ordered scatter plots can be seen in Figure A3a, which shows that for a given THEMIS scene ${}^{0}TPI_{Fe/Mg}$ values increase when ordered by increasing D2300 value. A similar plot was created for all of the THEMIS scenes listed in Table 2.

Our first step in maximizing the slope of points (optimizing the correlation) in the scatter plot for a given THEMIS scene was to determine which points represent CRISM detections of phyllosilicates – *i.e.*, to find the index value x_0 above which the D2300

value is greater than zero. Below x_0, a correlation between $TPI_{Fe/Mg}$ and x is not expected, so these data are fit to a horizontal line. Above x_0, $TPI_{Fe/Mg}$ should increase monotonically with x. We empirically determined that the trend of the points on the plot greater than x_0 is well represented by a quadratic function. Thus, the modeled trend can be expressed as:

$$Initial\_Model(x) = \begin{cases} a(x)^2 + b(x) + c, & for \; x > x_0 \\ a(x_0)^2 + b(x_0) + c, & x \le x_0 \end{cases}. \quad (3)$$

As expressed in the above equation, for values less than x_0, the fit is a horizontal line with the value of the quadratic fit at $x = x_0$.

Next, we vary the coefficients of $TPI_{Fe/Mg}$, providing different trial formulations, using ${}^0TPI_{Fe/Mg}$ (section 2.3.2) as a 'seed' for a computationally intensive optimization. The desired optimized formulation will feature not only a strong positive trend of $TPI_{Fe/Mg}$ values with increasing index value x, but also tight clustering of the points along the trend. This latter stipulation is important because we have found that formulations that give exceptionally steep trends also display unacceptably large scatter about that trend. Minimization of scatter about the trend is achieved by an automated optimization routine, known as MPFIT [*Markwardt*, 2008]. However, this routine requires a user-supplied model curve as a target for the optimization. Thus, our overall optimization process consisted of first picking a model target curve, providing this to MPFIT to find a trial formulation of $TPI_{Fe/Mg}$ that minimized scatter about that target curve, then incrementing the quadratic coefficient of the model target curve by a small amount, and re-running MPFIT using the results from the previous trial formulation of $TPI_{Fe/Mg}$ as the

seed. This two-tiered, nested optimization was repeated up until the point where the scatter about the target curve became unacceptable, as described below.

MPFIT uses a robust non-linear least squares curve fitting function, which minimizes the total chi-square value,

$$\chi^2 = \sum \frac{Target\_Model(x) - TPI_{Fe/Mg}(C_{(i,j)},x)}{error}, \quad (4)$$

by optimizing the coefficients $C_{(i,j)}$ for the band ratios in a trial formulation of $TPI_{Fe/Mg}$ (equation 2). For the variable *error* (the measurement error), we used the minimum noise equivalent delta emissivity (NEΔε) of 0.007 for a THEMIS band at surface temperatures from 245-270 K, as reported by *Christensen et al.* [2004]. A measurement error of 0.038 was also tested (the maximum NEΔε for a THEMIS band [*Christensen et al.* 2004]), and $TPI_{Fe/Mg}$ coefficient results were identical to three decimal places.

For the first run of MPFIT, we provided a target model (referred to as *Target_Model*(*x*)) derived by incrementing the quadratic coefficient of *Initial_Model*(*x*), *a*, by 0.01 (schematically indicated by the arrows in Figure A3a). In subsequent runs of MPFIT, *a* was further incremented by the same amount. This succession of incrementing the model and fitting the points to the new 'target' was repeated until the standard deviation of the trial $TPI_{Fe/Mg}$ values reached an upper limit of 0.00963. This value was chosen as an upper limit because it is the 1-σ variability of ${}^{0}TPI_{Fe/Mg}$ values for the family of lab clay spectra. It is the upper limit of variability that would be the expected for the $TPI_{Fe/Mg}$ value based solely on the spectral diversity of Fe/Mg-rich clays. The resulting scatter plot from a final optimized $TPI_{Fe/Mg}$ formulation for a single THEMIS-CRISM

scene pair is shown in Figure A3b. A similar optimization was performed for all the other scene pairs in Table 2, providing 12 uniquely optimized formulations of $TPI_{Fe/Mg}$.

An attempt was also made to derive an index sensitive to Al-rich phyllosilicates (TPI_{Al}) using a similar approach to that described above for $TPI_{Fe/Mg}$. However, the sensitivity of the final formulation of TPI_{Al} to the CRISM D2300 parameter was not statistically significant (see section 3.1).

2.3.4. Calculation of a *TPI* threshold value

In order to map THEMIS occurrences of phyllosilicates, a threshold value of $TPI_{Fe/Mg}$ was determined by comparison to the CRISM D2300 detection threshold. The $TPI_{Fe/Mg}$ threshold value, c^*, was determined for each individually optimized $TPI_{Fe/Mg}$ pairing listed in Table 2. This value was calculated using the final iteration of the *Target_Model*(x) at the point along the fit where the D2300 parameter equals zero (x_0), such that $c^* = Target\_Model(x_0)$. The 1-σ and 2-σ standard deviation of the fit of the final *Target_Model*(x) to the data points can be used to indicate more stringent threshold levels at c^*+1-σ and c^*+2-σ (see Figure A3b). The 1-σ and 2-σ threshold levels may be used to more accurately map phyllosilicates than c^*, as the $TPI_{Fe/Mg}$ values are not perfectly correlated with x.

3.0 RESULTS

3.1. Assessing the significance of a *TPI*

To evaluate the significance of the *TPI* fit for a THEMIS-CRISM pairing, the quadratic coefficient of the model, a in equation 3, was assessed for statistical significance. The *TPI* coefficients ($C_{(i,j)}$) resulting from the optimized *Target_Model*(x)

were considered significant if the 95% confidence limits (or ~2-σ) surrounding the *a* value were entirely positive. This indicates 95% confidence in a positive *a* value for the fit between the *TPI* and the ordered D2300 parameter values. Using these criteria, 10 of the 12 $TPI_{Fe/Mg}$-D2300 pairings did display a significant positive quadratic coefficient (see Table 2), but none of the TPI_{Al}-BD2210 pairings did the same. There are at least two potential reasons that would explain our inability to derive a statistically meaningful THEMIS spectral index for Al-rich phyllosilicates. The areal extent of Al-bearing phyllosilicate exposures in the Mawrth Vallis area is considerably less than that of Fe/Mg-rich phyllosilicate exposures [*e.g.*, *Loizeau et al.* 2007]. Also, *Poulet et al*. [2008] have used radiative transfer modeling of OMEGA data from Mawrth Vallis to determine that the Al-rich phyllosilicate kaolinite is only present at the ~20% level, whereas the Fe/Mg-rich phyllosilicate nontronite is present in modal abundances up to 65%. Lower areal extent and/or modal abundance of Al-rich phyllosilicates would both diminish the detectability of these minerals using the technique described here.

3.2. Final $TPI_{Fe/Mg}$ formulations for Mawrth Vallis and Nili Fossae

Optimized weighting coefficient for band ratios in the $TPI_{Fe/Mg}$ formulation for each scene is plotted in Figure A4. The coefficients for each THEMIS-CRISM scene pair in Mawrth Vallis were plotted separately from those in Nili Fossae, as the values appear to be location-specific. This is most likely because the background (non-phyllosilicate) compositions are different in these two locations. Overlapping scenes (*e.g.* I01199005 and I19047008) appear to have very similar coefficient values, even though there is considerable spread between scenes in the same region (Figure A4a). This suggests the range of $C_{(i,j)}$ values within the same region can be attributed to the

compositional variability between each scene, and is location, not scene, dependent. Therefore, it is necessary to make an individual *TPI* optimization for each scene when utilizing the technique presented here.

$TPI_{Fe/Mg}$ values for each scene pair were mapped at two threshold levels and compared to the D2300 parameter in overlapping regions (Figure A5 and A6). Threshold values, rather than the magnitudes of these parameters, were plotted since the relationship between the two datasets is nonlinear and it is easiest to evaluate more comparable results. Visual inspection reveals correspondence between the THEMIS and CRISM detections of Fe/Mg-rich phyllosilicates. Figure A7 and A8 demonstrate the major advantages our approach offers in mapping phyllosilicates, namely the extended coverage and improved spatial resolution provided by THEMIS relative to CRISM MSP data. The images in these figures are not limited to areas of overlap between the two datasets, but instead apply the $TPI_{Fe/Mg}$ formulations derived for areas of overlap to the entirety of each THEMIS scene. Mapping with THEMIS data roughly doubles the areal coverage relative to CRISM MSP coverage, and improves the spatial resolution from 200 m/pixel to 100 m/pixel.

4.0 DISCUSSION

4.1. Discrepancies between THEMIS vs. TES detections of phyllosilicates

The correlations between our THEMIS-based mapping of phyllosilicates and CRISM-based mapping are notable in the context of previous cross-instrumental, cross-wavelength comparisons that have been attempted. *Poulet et al.* [2008] found significant clay (30-65% modal abundance) in Mawrth Vallis using OMEGA data, whereas

Michalski and Fergason [2009] found no evidence for phyllosilicates above detection limits in TES data (~15%) in the same area. As previously mentioned, this apparent discrepancy may be accounted for by appealing to sub-pixel mixing of clay-rich and clay-poor surfaces with differing temperatures [*Michalski and Fergason*, 2009]. In this hypothesis, the cooler clay-rich material will contribute less to the overall radiance, and therefore emissivity. In THEMIS data, exposures of cooler clay-rich material that are sub-pixel sized in TES data may span several 100-m pixels, thus avoiding the tendency for nearby warmer surfaces to dominate the overall radiance in a pixel [*Viviano and Moersch*, 2011], and may account for the ability to map clays with the $TPI_{Fe/Mg}$ method discussed here. THEMIS data could also provide the spatial resolution needed to overcome the reduction in spectral contrast associated with small sub-pixel exposures of phyllosilicates (without thermal heterogeneity) at the ~3km resolution of TES.

4.2. Potential false positives – Laboratory spectra

While it is not possible to evaluate the potential for false positive detections using THEMIS spectra from unknown surfaces on Mars, it is possible to make an evaluation of our general approach by testing for false positives with the ${}^{0}TPI_{Fe/Mg}$ formulation (which was derived using laboratory spectra of phyllosilicates) using pure (unmixed) laboratory spectra of other potentially confounding minerals. Detection of a particular phase is considered to be a false positive if, when ${}^{0}TPI_{Fe/Mg}$ is applied to its spectrum, the resulting value is higher than 1.071, which is the ${}^{0}TPI_{Fe/Mg}$ value for a laboratory spectrum of a pure Fe/Mg-rich smectite (SWa-1). All of the other Fe/Mg-rich smectites in the ASU spectral library yield ${}^{0}TPI_{Fe/Mg}$ values within 0.05 of this value. This approach compares pure laboratory clay (not mixed with ST1) The resulting potential false positives are

described below; these phases should be considered as potential alternate explanations for high $TPI_{Fe/Mg}$ values when mapping phyllosilicates by the method described here.

4.2.1. Well-crystalline, non-phyllosilicate felsic minerals

When applied to laboratory spectra, the ${}^{0}TPI_{Fe/Mg}$ equation yields higher values for a handful of non-phyllosilicate minerals than it does when applied to a laboratory spectrum of pure smectite. Of 50 non-phyllosilicate mineral spectra from the ASU spectral library [*Christensen et al.* 2000] tested, only 5 minerals yielded false positive detections for Fe/Mg-rich phyllosilicates: albite (WAR-0612), apatite (P1, P2), jadeite (WAR-9909), microcline (BUR-3460), and spodumene (HS-210.4B) (Figure A9). The spectra of all these phases are broadly similar to the spectrum of Fe/Mg-rich smectite at the relatively low spectral resolution of THEMIS. Except for apatite (a minor accessory mineral, unlikely to be a spectrally significant phase on Mars), these minerals are felsic silicates. It is unlikely that this misidentification would be a widespread issue when using $TPI_{Fe/Mg}$, as only a few, localized areas on Mars have been found to contain dominantly felsic compositions [*Bandfield et al.* 2004b; *Ehlmann et al.* 2009; *Smith et al.*, 2011]. The most likely confounding mineral is albite; however, TES abundance maps [*Milam et al.*, 2010] indicate few (if any) identifications of this phase.

4.2.2. Phyllosilicates (non-smectites)

Although the index was initially formulated using Fe/Mg-rich smectite compositions, it is also sensitive to a variety of other, dominantly Fe/Mg-rich phyllosilicates. Hence, the index is referred to as the THEMIS *Phyllosilicate* Index, rather than a Smectite Index (although, for completeness, we note that it is not sensitive to one Fe/Mg-rich non-smectite phyllosilicate, palygorskite). ${}^{0}TPI_{Fe/Mg}$ yields values

higher than 1.071 for the following (non-smectite) phyllosilicates: biotite (BUR-840), chlorite (WAR-1924), clinochlore (BUR-1340), kaolinite (KGa-1b), muscovite (WAR-5474), serpentine (HS-8.4B), phlogopite (HS-23.3b), and talc (BUR-4640C) from the ASU spectral library [*Christensen et al.* 2000].

4.2.3. False positive testing of other candidate Martian materials

We also applied ${}^{0}TPI_{Fe/Mg}$ to spectra of a variety of materials suggested in the literature as candidate components of the Martian surface to identify other potential false positives. The ${}^{0}TPI_{Fe/Mg}$ values obtained by applying the index to opal and silica polymorphs [*Michalski et al.*, 2003] suggest that the index yields false positives for more-crystalline opaline phases (samples 02-031, 02-020, and 02-015; not Opal-A), as well as synthesized coesite (unlabelled) and quartz (ASU Library, BUR-4120) (Figure A10). Upon visual inspection of the spectra, it appears that a stronger weighting of the b4/b5 ratio could help discriminate between these phases and Fe/Mg-rich phyllosilicate. It is possible that if any of these Si-rich phases and Fe/Mg-rich phyllosilicates were both present in a THEMIS scene, the optimization routine would produce an index that could discriminate between them. This illustrates the importance of using actual THEMIS spectra to refine the weighting coefficients used in the final $TPI_{Fe/Mg}$ formulation for a given scene.

Because zeolites have been noted for their spectral similarities to phyllosilicates, [*e.g.*, *Ruff*, 2004] we also evaluated the spectra of analcime, chabazite, erionite, heulandite, and mordenite from the JHU spectral library [*Salisbury et al.*, 1991] as potential false positives, but all of these phases yielded ${}^{0}TPI_{Fe/Mg}$ values below 1.071. Spectra of other candidate Martian materials were also tested. Meteorite basalt proxy,

TES basalt proxy, TES andesite proxy, andesite interstitial glass, dacite interstitial glass [*Minitti and Hamilton*, 2010] and quenched basalt [*Wyatt et al.*, 2001], all yield ${}^{0}TPI_{Fe/Mg}$ values below that of smectite (*i.e.*, were not false positives). The spectra of alkali (Si-Al-K-Na) glass and pure SiO_2 glass [*Wyatt et al.*, 2001] both yield ${}^{0}TPI_{Fe/Mg}$ values above that of 100% smectite. The alkali glass is completely indiscernible from the smectite and must be considered a significant source of false identifications with $TPI_{Fe/Mg}$.

4.2.3. Grain size effects

Fine particles show significant spectral differences from coarse-grained particles or massive samples. This has been well recognized and modeled in the thermal infrared [*e.g.*, *Conel*, 1969; *Moersch and Christensen*, 1995; *Ramsey and Christensen*, 1998]. The increase in porosity that accompanies a decrease in grain size creates multiple surface reflections, and causes a decrease in the spectral contrast of fundamental mode absorption features and the development of new spectral features. Spectral differences also arise with temperature gradients that develop at the surface, particularly in fine particles [*Henderson and Jakosky*, 1996]. To test the sensitivity of ${}^{0}TPI_{Fe/Mg}$ to particle size effects, we applied the index to the spectra of two samples consisting of the same composition as SWa-1, but in smaller grain sizes (Figure A11). These two samples yield ${}^{0}TPI_{Fe/Mg}$ values under 1.071 (Figure A11, right). Thus, the method described here may not be appropriate for mapping disaggregated, fine-grained exposures of clays.

4.3. Discrepancies between THEMIS vs. CRISM detections of phyllosilicates

Visible discrepancies between the resulting D2300 parameter and $TPI_{Fe/Mg}$ mapping are expected for a number of likely reasons beyond the candidate false-positive phases described above. As discussed in section 2.3, the near-infrared and thermal

infrared portion of the spectrum are sensitive to different parts of the phyllosilicate structure. While the X-OH bond in the octahedral layer has absorptions in both wavelength ranges, whether the clay is di- or trioctahedral and whether Al substitution is occurring the tetrahedral sheet may have confounding effects in the thermal infrared spectra that are not apparent in the near-infrared. It is impossible to disentangle these effects from other phenomenon that may cause a discrepancy, as the complete chemistry of Martian phyllosilicates has yet to be characterized.

The transmission spectrum of atmospheric dust is very similar to the spectral shape of phyllosilicates [*e.g.*, *Ruff*, 2004], particularly at THEMIS spectral resolution, and could possibly be a source for discrepancies. Atmospheric dust is fairly uniform across a single THEMIS scene, and thus the calibration of an individual $TPI_{Fe/Mg}$ to the D2300 index would likely negate any scene-wide false-positives. However, scenes that have considerably variable topography may be susceptible to the influence of this factor. $TPI_{Fe/Mg}$ identifications of phyllosilicates in particularly low elevations within a scene would be more susceptible to this factor, as the dust contribution through a thicker section of atmosphere is greater. For example, atmospheric dust may account for false-positive $TPI_{Fe/Mg}$ detections in the mouth of the Mawrth Vallis channel (~26º N, 20.5º W), which lies ~1 km below the phyllosilicate-bearing deposits surrounding the channel (Figure A5 and A7). This also likely accounts for false-positive $TPI_{Fe/Mg}$ detections at the lowest elevations in the Nili Fossae region, within the fossae themselves (*e.g.*, ~22.5º N, 77.6º E).

5.0 CONCLUSIONS

We have developed a statistically optimized band ratio technique for mapping phyllosilicates at a regional scale on Mars with THEMIS daytime thermal infrared data, using the CRISM-mapped occurrences of these minerals in Mawrth Vallis and Nili Fossae as examples. The near-global coverage of the THEMIS dataset, paired with its 100-m/pixel spatial resolution, can be utilized to extend and improve mapping of Fe/Mg-rich phyllosilicates beyond the coverage currently afforded by CRISM MSP data. There is significant correlation between the phyllosilicate detections mapped by CRISM via the D2300 parameter and those mapped by THEMIS using our $TPI_{Fe/Mg}$ spectral index. The optimized coefficients of $TPI_{Fe/Mg}$ vary from one THEMIS scene to another, and between the two example regions, likely because of differences in background (non-phyllosilicate) surface compositions. The application of this approach for an individual THEMIS scene relies on the presence of co-occurring CRISM coverage.

A sensitivity analysis of a laboratory-derived version of the index ($^{0}TPI_{Fe/Mg}$) shows little potential for false positives from most materials considered relevant to the Martian surface. Materials that can give false positive detections include felsic silicates, alkali glass, and high-Si crystalline and glass phases. Reduced spectral contrast associated with particle size effects also diminishes $TPI_{Fe/Mg}$ sensitivity to phyllosilicates.

The cross-instrument, cross-wavelength strategy we have used to develop a spectral index sensitive to phyllosilicates in this study may be useful in future work for creating indices sensitive to other compositions of interest, thereby extending the mapping of those phases on Mars beyond what is currently available with a single instrument or spectral region.

REFERENCES

Bandfield, J. L., V. E. Hamilton, P. R. Christensen (2000), A global view of Martian surface compositions from MGS-TES, *Science*, *287*, 1626-1630.

Bandfield, J. L. (2002), Global mineral distributions on Mars, *J. Geophys. Res.*, *107*(E6), doi:10.1029/2001JE001510.

Bandfield, J. L., D. R. Rogers, M. D. Smith, and P. R. Christensen (2004a), Atmospheric correction and surface spectral unit mapping using Thermal Emission Imaging System data, *J. Geophys. Res.*, *109*, E10008, doi:10.1029/2004JE002289.

Bandfield, J. L., V. E. Hamilton, P. R. Christensen, and H. Y. McSween Jr. (2004b), Identification of quartzofeldspathic materials on Mars, *J. Geophys. Res.*, *109*, E10009, doi:10.1029/2004JE002290.

Bibring, J. P., *et al.* (2004), OMEGA: Observatoire pour la Minéralogie, l'Eau, les Glaces, et l'Activité, in *Mars Express: the scientific payload*, edited by A. Wilson, pp. 37-50, Eur. Space Agency, Noordwijk, Netherlands.

Bibring, J. P., *et al.* (2006), Global mineralogical and aqueous mars history derived from OMEGA/Mars express data, *Science*, *312*, 400-404, doi:10.1126/science.1122659.

Bishop, J.L., E. Murad, and M. D. Dyar (2002), The influence of octahedral and tetrahedral cation substitution on the structure of smectites and serpentines as observed through infrared spectroscopy, *Clay Mineral*, *37*, 617-628.

Bishop, J. L., E. Z. Noe Dobrea, N. K. McKeown, M. Parente, B. L. Ehlmann, J. R. Michalski, R. E. Milliken, F. Poulet, G. A. Swayze, J. F. Mustard, S. L. Murchie, and J. –P. Bibring (2008), Phyllosilicate diversity and past aqueous activity revealed at Mawrth Vallis, Mars, *Science*, *321*, 830-833, doi:10.1126/science.1159699.

Buczkowski, D. L., S. Murchie, R. Clark, K. Seelos, F. Seelos, E. Malaret, and C. Hash (2010), Investigation of an Argyre basin ring structure using Mars Reconnaissance Orbiter/Compact Reconnaissance Imaging Spectrometer for Mars, *J. Geophys. Res.*, *115*, E12011, doi:10.1029/2009JE003508.

Carter, J., F. Poulet, J. –P. Bibring, and S. Murchie (2010), Detection of hydrated silicates in crustal outcrops in the northern plains of Mars, *Science*, *328*, doi: 10.1126/science.1189013.

Chevrier, V., and P.E. Mathé (2007), Mineralogy and evolution of the surface of Mars: A review, *Planetary and Space Science*, *55*, 289-314, doi:10.1016/j.pss.2006.05.039.

Christensen, P.R., N.S. Gorelick, G.L. Mehall, and K.C. Murray, THEMIS Public Data Releases, Planetary Data System node, Arizona State University, <http://themis-data.asu.edu>.

Christensen, P. R., J. L. Bandfield, V. E. Hamilton, D. A. Howard, M. D. Lane, J. L. Piatek, S. W. Ruff, and W. L. Stefanov (2000), A thermal emission spectral library of rock-forming minerals, *J. Geophys. Res.*, *105*(E4), 9735 – 9739.

Christensen, P. R., *et al.* (2001), Mars Global Surveyor Thermal Emission Spectrometer experiment: Investigation description and surface science results, *J. Geophys. Res.*, *106*(E10), 23,823-23,872.

Christensen, P. R., *et al.* (2004), The THermal Emission Imaging System (THEMIS) for the Mars 2001 Odyssey mission, *Sp. Sci. Rev.*, *110*, 85-130.

Clark, R. N., T. V. V. King, M. Klejwa, G. A. Swayze, and N. Vergo (1990), High spectral resolution reflectance spectroscopy of minerals, *J. Geophys. Res.*, *95*, 12653 – 12680.

Conel, J. E. (1969), Infrared emissivities of silicates: Experimental results and a cloudy atmosphere model of spectral emission from condensed particulate mediums, *J. Geophys. Res.*, *74*, 1614 – 1634.

Ehlmann, B. L., J. F. Mustard, C. I. Fassett, S. C. Schon, J. W. Head, D. J. Des Marais, J. A. Grant, and S. L. Murchie (2008), Clay minerals in delta deposits and organic preservation potential on Mars, *Nature Geoscience*, *1*(6), 355-358, doi:10.1038/ngeo207.

Ehlmann, B. L. *et al.* (2009), Identification of hydrated silicate minerals on Mars using MRO-CRISM: Geologic context near Nili Fossae and implications for aqueous alteration, *J. Geophys. Res.*, *114*, E00D08, doi:10.1029/2009JE003339.

Ehlmann, B. L., J. F. Mustard, and S. L. Murchie (2010) Geologic setting of serpentine deposits on Mars, *Geophys. Res. Lett.*, *37*, L06201, doi:10.1029/2010GL042596.

Farmer, C. B., and P.E. Doms (1979), Global and seasonal variation of water vapor on Mars and the implications for permafrost, *J. Geophys. Res.*, *84*, 2881-2888.

Farmer, J. D., and D. J. Des Marais (1999), Exploring for a record of ancient Martian life, *J. Geophys. Res.*, *104*(E11), 26,977-26,995.

Gillespie, A. R., A. B. Kahle, and R. E. Walker (1986), Color enhancement of highly correlated images: I. Decorrelation and HSI contrast stretches, *Remote Sens. Environ.*, *20*, 209-235, doi: 10.1016/0034-4257(86)90044-1.

Grant, J. A. *et al.* (2008), HiRISE imaging of impact megabreccia and sub-meter aqueous strata in Holden Crater, Mars, *Geology*, *36*(3), 195-198, doi: 10.1130/G24340A.1.

Hamilton, V. E., M. B. Wyatt, H. Y. McSween, and P. R. Christensen (2001), Analysis of terrestrial and Martian volcanic compositions using thermal emission spectroscopy. 2.

Application to Martian surface spectra from the Mars Global Surveyor Thermal Emission Spectrometer, *J. Geophys. Res.*, *106*(7), 14,733-14,746.

Henderson, B. G. and B. M. Jakosky (1994), Near-surface thermal gradients and their effects on mid-infrared emission spectra of planetary surfaces, *J. Geophys. Res.*, *99*(E9), 19063–19073.

Henderson, B. G., P. G. Lucey, and B. M. Jakosky (1996), New laboratory measurements of mid-IR emission spectra of simulated planetary surfaces, *J. Geophys. Res.*, *101*(E6), 14969-14975.

Henderson, B. G., B. M. Jakosky (1997), Near-surface thermal gradients and mid-IR emission spectra: a new model including scattering and application to real data, *J. Geophys. Res.*, *102* (E3), 6567–6580.

Keller, W. D., and E. E. Pickett (1950), Absorption of infra-red radiation by clay minerals, *Am. J. Sci.*, *248*, 264-273.

Kraft, M. D., J. R. Michalski, and T. G. Sharp (2003), Effects of pure silica coatings on thermal emission spectra of basaltic rocks: considerations for martian surface mineralogy, *Geophys. Res. Lett.*, *30*(24), 2288, doi:10.1029/2003GL018848.

Leighton, R. B., and B. C. Murray (1966), Behavior of CO_2 and other volatiles on Mars, *Science*, *153*, 136-144.

Levenberg, K. (1944), A method for the solution of certain non-linear problems in least squares, *Quart. Appl. Math.*, *2*, 164–168.

Langevin, Y., S. Douté, M. Vincendon, F. Poulet, J. –P. Bibring, B. Gondet, B. Schmitt, and F. Forget (2006), No signature of clear CO2 ice from the 'cryptic' regions in Mars' south seasonal polar cap, *Nature*, *447*, 790-792, doi:10.1038/nature05012.

Loizeau, D., N. Mangold, F. Poulet, J. –P. Bibring, A. Gendrin, V. Ansan, C. Gomez, B. Gondet, Y. Langevin, P. Masson, and G. Neukum (2007), Phyllosilicates in the Mawrth Vallis region of Mars, *J. Geophys. Res.*, *112*, E08S08, doi:10.1029/2006JE002877.

Madejová and Komadel (2001), Baseline studies of the clay minerals society source clays: Infrared methods, *Clays and Clay Minerals*, *49*, 410-432.

Mangold, N., F. Poulet, J. F. Mustard, J. –P. Bibring, B. Gondet, Y. Langevin, V. Ansan, Ph. Masson, C. Fassett, J. W. Head, H. Hoffmann, and G. Neukum (2007), Mineralogy of the Nili Fossae region with OMEGA/Mars Express data: 2. Aqueous alteration of the crust, *J. of Geophys. Res.*, *112*, E08S04, doi:10.1029/2006JE002835.

Marquardt, D. (1963), An algorithm for least-squares estimation of nonlinear parameters, *SIAM J. Appl. Math.*, *11*, 431–441, doi:10.1137/0111030.

Markwardt, C. B. (2008), Non-linear least squares fitting in IDL with MPFIT, paper presented at Astronomy Data Analysis Software and Systems XVIII, Quebec, Canada, ASP Conference Series, vol. 411, edited by D. Bohlender, P. Dowler, and D. Durand, pp. 251-254, Astronomical Society of the Pacific: San Francisco, CA.

McDowell, M. L. and V. E. Hamilton (2009), Seeking phyllosilicates in thermal infrared data: A laboratory and Martian data case study, *J. Geophys. Res.*, *114*, E06007, doi:10.1029/2008JE003317.

Michalski, J. R., M. D. Kraft, T. G. Sharp, L. B. Williams, and P. R. Christensen (2005), Mineralogical constraints on the high-silica martian surface component observed by TES, *Icarus*, *174*, 161-177, doi:10.1016/j.icarus.2004.10.022.

Michalski, J. R., S. W. Ruff, and P. R. Christensen (2006a), TES and THEMIS analysis of Martian clay-bearing deposits discovered by Mars Express OMEGA, paper presented at *Lunar Planet. Sci. XXXVII*, Abstract 1242.

Michalski, J. R., M. D. Kraft, T. G. Sharp, L. B. Williams, and P. R. Christensen (2006b), Emission spectroscopy of clay minerals and evidence for poorly crystalline

aluminosilicates on Mars from Thermal Emission Spectrometer data, *J. Geophys. Res.*, *111*, E03004, doi:10.1029/2005JE002438.

Michalski, J. R. and R. L. Fergason (2009), Composition and thermal inertia of the Mawrth Vallis region of Mars from TES and THEMIS data, *Icarus*, *199*, 25-48.

Minitti, M. E., and V. E. Hamilton (2010), A search for basalt-to-intermediate glasses on Mars: assessing martian crustal mineralogy, *Icarus*, *210*, 135–149, doi:10.1016/j.icarus.2010.06.028.

Milam, K. A., McSween, H. Y., Moersch, J., and Christensen, P. R. (2010) Distribution and variation of plagioclase compositions on Mars: *Journal of Geophysical Research*, v. 115, E09004, doi:10.1029/2009JE003495.

Moersch, J. E., and P. R. Christensen (1995), Thermal emission from particulate surfaces: A comparison of scattering models with measured spectra, *J. Geophys. Res.*, *100*, 7465 – 7477.

Morris, R. V., T. G. Graff, S. A. Mertzman, M D. Lane, and P. R. Christensen (2003), Palagonitic (not andesitic) Mars: evidence from thermal emission and VNIR spectra of palagonitic alteration rinds on basaltic rock. *Sixth Int. Conf. Mars*, Pasadena, CA, Abstract 3211.

Murchie, S. L., et al. (2007a), Compact Reconnaissance Imaging Spectrometer for Mars (CRISM) on Mars Reconnaissance Orbiter (MRO), *J. Geophys. Res*, *112*, E05S03, doi:10.1029/2006JE002682.

Murchie, S. L., E. Guinness, and S. Slavney (2007b), CRISM data product software interface specification, ftp://pds-geosciences.wustl.edu/mro-crism/mro-m-crism-2-edr-v1/mrocr_0001/document/crism_dpsis.pdf, *NASA Planet. Data Syst.*, Greenbelt, Md., 17 Aug.

Murchie, S. L. (2009), A synthesis of Martian aqueous mineralogy after 1 Mars year of observations from the Mars Reconnaissance Orbiter, *J. Geophys. Res.*, *114*, E00D06, doi:10.1029/2009JE003342.

Mustard, J. F., *et al.* (2008), Hydrated silicate minerals on Mars observed by the Mars Reconnaissance Orbiter CRISM instrument, *Nature*, *454*, 305-309, doi:10.1038/nature07097.

Mustard, J. F. and J. E. Hays (1997), Effects of hyperfine particles on reflectance spectra from 0.3 to 15 μm, *Icarus*, *125*, 145-163.

Noe Dobrea, E.Z, J. Moore, A. Howard, D. Catling, and J. Grant (2008), Spectral and geomorphic evidence for a past inland sea in Eridania Basin, Mars, paper presented at AGU Fall Meeting, Abstract P32B-03.

Osterloo, M. M., *et al.* (2008), Chloride-bearing materials in the Southern Highlands of Mars, *Science*, *319*, 1651-1654.

Parente, M. (2008), A new approach to denoising CRISM images, paper presented at Lunar Planet. Sci., XXXIX, Abstract 2528.

Pelkey, S. M. *et al.* (2007), CRISM multispectral summary products: Parameterizing mineral diversity on Mars from reflectance, *J. Geophys. Res.*, *112*, E08S14, doi:10.1029/2006JE002831.

Piatek, J. L., and J. E. Moersch (2006), A strategy for atmospheric correction of THEMIS infrared data, paper presented at Lunar Planet. Sci., XXXVII, Abstract 1158.

Poulet, F., J. –P. Bibring, J. F. Mustard, A. Gendrin, N. Mangold, Y. Langevin, R. E. Arvidson, B. Gondet, C. Gomez, and the Omega Team (2005), Phyllosilicates on Mars and implications for early martian climate, *Nature*, *438*, 623-627, doi:10.1038/nature04274.

Poulet, F., N. Mangold, D. Loizeau, J. –P. Bibring, Y. Langevin, J. Michalski, and B. Gondet (2008), Abundance of minerals in the phyllosilicate-rich units on Mars, *Astron. Astrophys.*, *487*, L41-L44, doi:10.1051/0004-6361:200810150.

Ramsey, M. S., and P. R. Christensen (1998), Mineral abundance determination: Quantitative deconvolution of thermal emission spectra, *J. Geophys. Res.*, *103*, 577 – 596.

Roach, L. H., *et al.* (2010), Hydrated mineral stratigraphy of Ius Chasma, Valles Marineris, *Icarus*, *206*, 253-268 doi: 10.1016/j.icarus.2009.09.003.

Rogers, A. D., and J. L. Bandfield (2009), Mineralogical characterization of Mars Science Laboratory candidate landing sites from THEMIS and TES data, *Icarus*, *203*, 437-*453* doi: 10.1016/j.icarus.2009.04.020.

Ruff, S. W., and P. R. Christensen (2002), Bright and dark regions on Mars: Particle size and mineralogical characteristics based on Thermal Emission Spectrometer data, *J. Geophys. Res.*, *107*(E12), 5127, doi:10.1029/2001JE001580.

Ruff, S. W. (2004), Spectral evidence for zeolite in the dust on Mars, *Icarus*, *168*, 131-143, doi:10.1016/j.icarus.2003.11.003.

Ruff, S. W., and P. R. Christensen (2007), Basaltic andesite, altered basalt, and a TES-based search for smectite clay minerals on Mars, *Geophys. Res. Lett.*, *34*, L10204, doi:10.1029/2007GL029602.

Salisbury, J. W., L. S. Walter, N. Vergo, and D. M. D'Aria (1991), Infrared (2.1–25 μm) *Spectra of Minerals*, 267 pp., Johns Hopkins Univ. Press, Baltimore, MD.

Salisbury, J. W., L. S. Walter, N. Vergo, and D M. D'Aria, (1992), *Infrared (2.1-25μm) Spectra of Minerals,* Johns Hopkins Univ. Press, Baltimore, Md.

Smith, M. R., J. L. Bandfield, and A. Gillespie (2010), Geologic history of a felsic and hydrated mineral suite in Syrtis Major, paper presented at 2010 Fall Meeting, AGU, San Francisco, Calif., Abstract P53C-1530.

Viviano, C. E. and J. E. Moersch (2011), Using THEMIS to address discrepancies between OMEGA/CRISM and TES detections of phyllosilicates, paper presented at Lunar Planet. Sci., XLII, Abstract 2551.

Velde, B., Righi, D., Meunier, A., Hillier, S., and A. Inoue (1995) Composition and mineralogy of clay minerals, in *Origin and mineralogy of clays: clays and the environment*, edited by B. Velde, pp. 8-42, Springer, Berlin.

Wray, J. J., S. L. Murchie, S. W. Squyres, F. P. Seelos, and L. L. Tornabene (2009), *Geology*, *37*(11), 1043–1046, doi: 10.1130/G30331A.1.

Wyatt, M. B., V. E. Hamilton, H. Y. McSween, P. R. Christensen, and L. A. Taylor (2001), Analysis of terrestrial and martian volcanic compositions using thermal emission

spectroscopy: 1. Determination of mineralogy, chemistry, and classification strategies, *J. Geophys. Res.*, *106*(E7), 14,711-14,732.

Wyatt, M. B., and H. Y. McSween (2002), Spectral evidence for weathered basalt as an alternative to andesite in the northern lowlands of Mars, *Nature*, *417*, 263-266.

Appendix A

Table A1. Determination of Band Ratios and Initial Weighting Coefficient Values for Potential Fe/Mg-rich THEMIS Phyllosilicate Indices[a]

Candidate Band Ratio	Total variability of ratio in synthetic suite of Mars spectra	1-σ variability of ratio in family of lab spectra[b]	Normalized weighting coefficients for initial *TPI*[c]
b4/b5	0.0359	**0.0223**	**0.1550**
b4/b6	0.0241	**0.0221**	**0.1040**
b7/b4	0.0030	0.0218	
b4/b8	0.0017	0.0216	
b4/b9	0.0039	0.0215	
b6/b5	0.0108	**0.0006**	**0.0468**
b7/b5	0.0359	**0.0008**	**0.1553**
b8/b5	0.0310	**0.0008**	**0.1339**
b9/b5	0.0287	**0.0008**	**0.1242**
b7/b6	0.0256	**0.0129**	**0.1108**
b8/b6	0.0208	**0.0128**	**0.0898**
b9/b6	0.0186	**0.0128**	**0.0803**
b7/b8	0.0046	0.0201	
b7/b9	0.0067	0.0200	
b8/b9	0.0021	0.0212	

[a]See section 2.3.1 for a description of this determination.
[b]Values in this column are bolded if less than the associated value in the second column.
[c]Blank rows in this column indicate a candidate band ratio that was not used.

Table A2. Selected THEMIS and CRISM MSP Scene Pairings Used in Optimization of $TPI_{Fe/Mg}$ Coefficients for Each Scene

THEMIS product ID	Paired CRISM MSP product IDs
	Mawrth Vallis
I01199005	MSP00005994_03, MSP000061e8_01, MSP00005399_01, MSP0000388d_07, MSP000031bc_01
I01561006	MSP00005994_03, MSP000061e8_01, MSP00005399_01, MSP0000388d_07, MSP000031bc_01
I03783002	MSP00003a40_07, MSP0000556b_01, MSP00007942_03, MSP000034d8_05
I04582010	MSP000075de_05, MSP0000481d_05, MSP00012e32_01, MSP00003a40_07, MSP0000556b_01
I19047008	MSP00003a40_07, MSP0000556b_01, MSP00007942_03, MSP000034d8_05
I37153009[a]	MSP00012e32_01, MSP00003a40_07, MSP0000556b_01, MSP00007942_03, MSP000034d8_05
I38039006[a]	MSP00012e32_01, MSP00003a40_07, MSP0000556b_01, MSP00007942_03, MSP000034d8_05
I39449009	MSP00005994_03, MSP000061e8_01, MSP00005399_01, MSP0000388d_07, MSP000031bc_01
	Nili Fossae
I01645007	MSP0000c752_01, MSP000106bc_03, MSP00008dee_01, MSP00013755_01, MSP00014007_01, MSP0000397f_05, MSP00012f58_01
I01982006	MSP00008dee_01, MSP00013755_01, MSP00014007_01, MSP0000397f_05, MSP00012f58_01
I02007009	MSP000106bc_03, MSP00008dee_01, MSP00013755_01, MSP00014007_01, MSP0000397f_05
I02731002	MSP000106bc_03, MSP00008dee_01, MSP00013755_01, MSP00014007_01, MSP0000397f_05, MSP00012f58_01
I02756002	MSP0000c752_01, MSP000106bc_03, MSP00008dee_01, MSP00013755_01, MSP00014007_01

[a]THEMIS and CRISM pairs were not statistically correlated (see section 3.1).

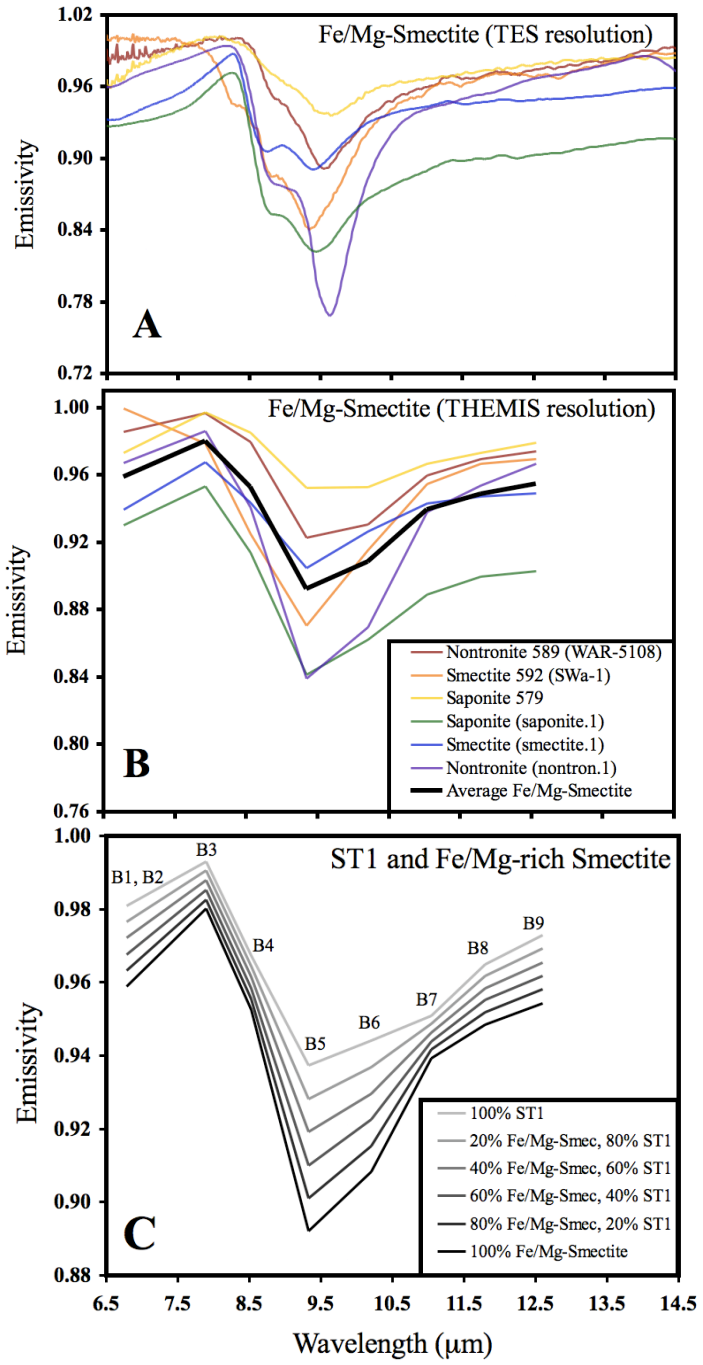

Figure A1. Laboratory spectra of Fe/Mg-rich smectites at different spectral resolution and in mixtures. (a) JHU and ASU laboratory spectra of Fe/Mg-rich smectite spectra at TES spectral resolution. (b) The same spectra at THEMIS spectral resolution. Also shown is an averaged laboratory Fe/Mg-rich smectite spectrum of all the samples plotted. (c) Mixing of TES Surface Type 1 (ST1) spectrum with varying amounts of (averaged) laboratory Fe/Mg-rich smectites. Annotations above the ST1 spectrum indicate THEMIS band numbers and apply to all subsequent figures showing THEMIS resolution spectra. See section 2.3 for descriptions of the components in the averaged phyllosilicate spectra.

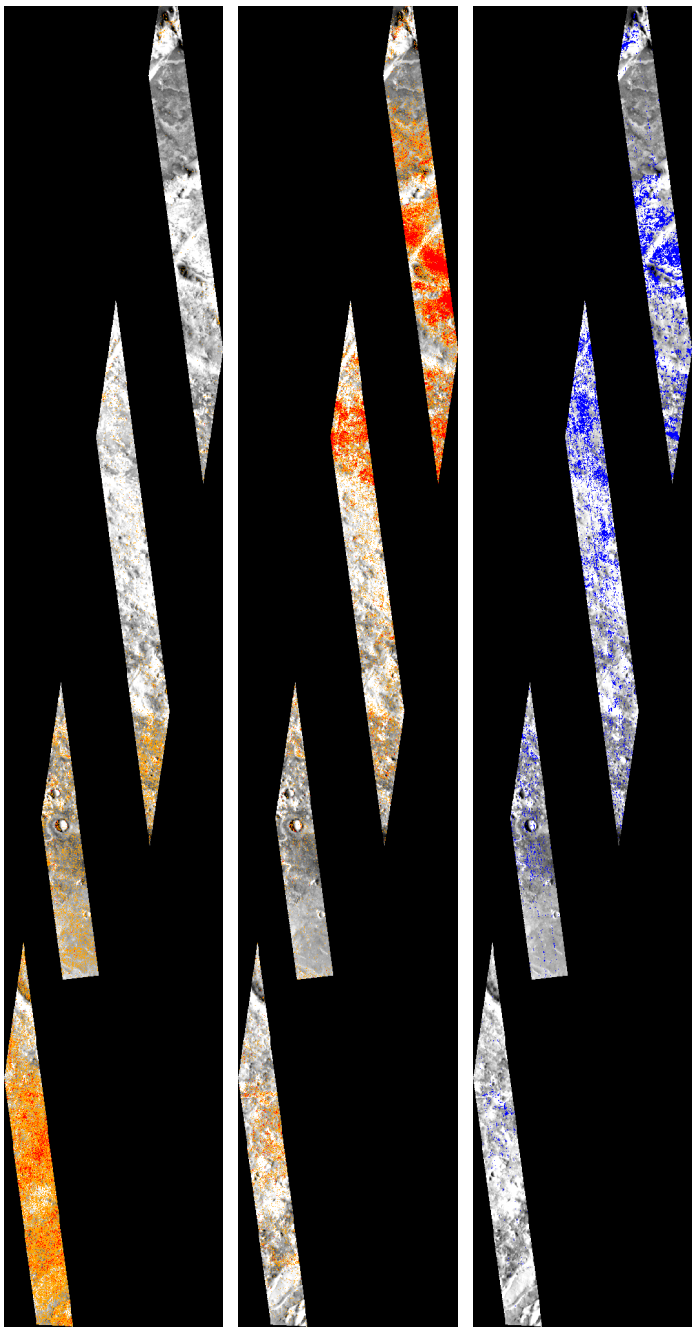

Figure A2. Example of phyllosilicate mapping in the Nili Fossae region, showing improvement from ${}^{0}TPI_{Fe/Mg}$ to the optimized $TPI_{Fe/Mg}$ as compared to CRISM detections. The THEMIS brightness temperature image (background) covers the area of intersection between THEMIS daytime infrared and CRISM MSP data. (left) ${}^{0}TPI_{Fe/Mg}$ map: orange indicates values above the threshold value plus the 1-σ value for the fit of the model; red indicates the threshold value plus 2-σ (see section 2.3.4. for description). (middle) Optimized $TPI_{Fe/Mg}$ map using the same color classification. (right) Scaled CRISM D2300 parameter map: blue indicates values greater than 0 (no CRISM detection of clay).

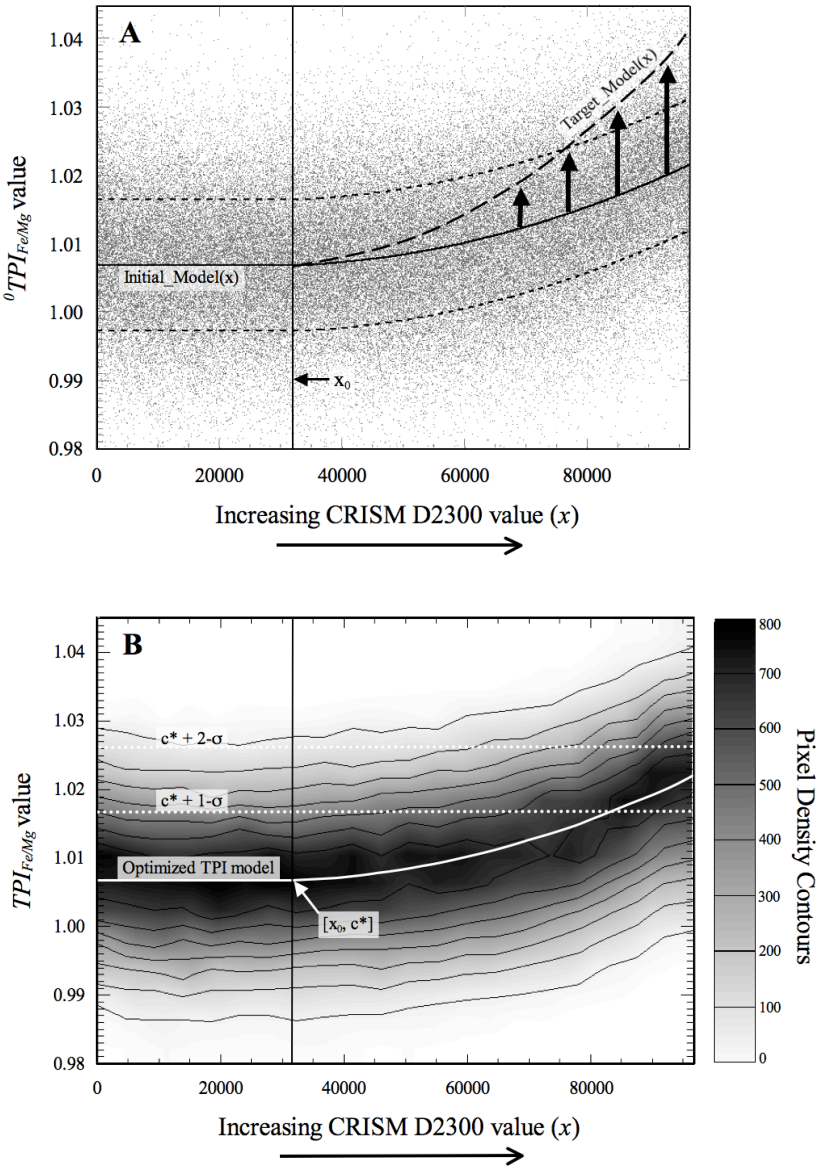

Figure A3. Example plot of values from the overlapping areas of the THEMIS scene I01199005 and the associated CRISM MSP D2300 parameter. D2300 values are ordered by increasing band drop value and given the index variable x (section 2.3.3), which is associated with a particular co-located THEMIS pixel. The x_0 position corresponds to the index value associated with a D2300 value of zero. The index variables are plotted against (a) the associated $^0TPI_{Fe/Mg}$ value of that THEMIS pixel. Solid black line indicates *Initial_Model*(x), (see equation 3, section 2.3.3), and arrows schematically show displacement of the trend toward an incremented *Target_Model*(x), indicated by long-dashed line. The short-dashed lines delineate the 1-σ standard deviation for the entire population of points provided by $^0TPI_{Fe/Mg}$. (b) Optimized $TPI_{Fe/Mg}$ value plotted against the associated ordered D2300 parameter, x. In this plot, pixel density is shown in grayscale (bin width of $x = 500$) rather than individual points, to highlight clustering towards the optimized model. In this case, the threshold value (see section 2.3.4) c*=1.00682, c*+1-σ=1.0164, and c*+2-σ=1.0260.

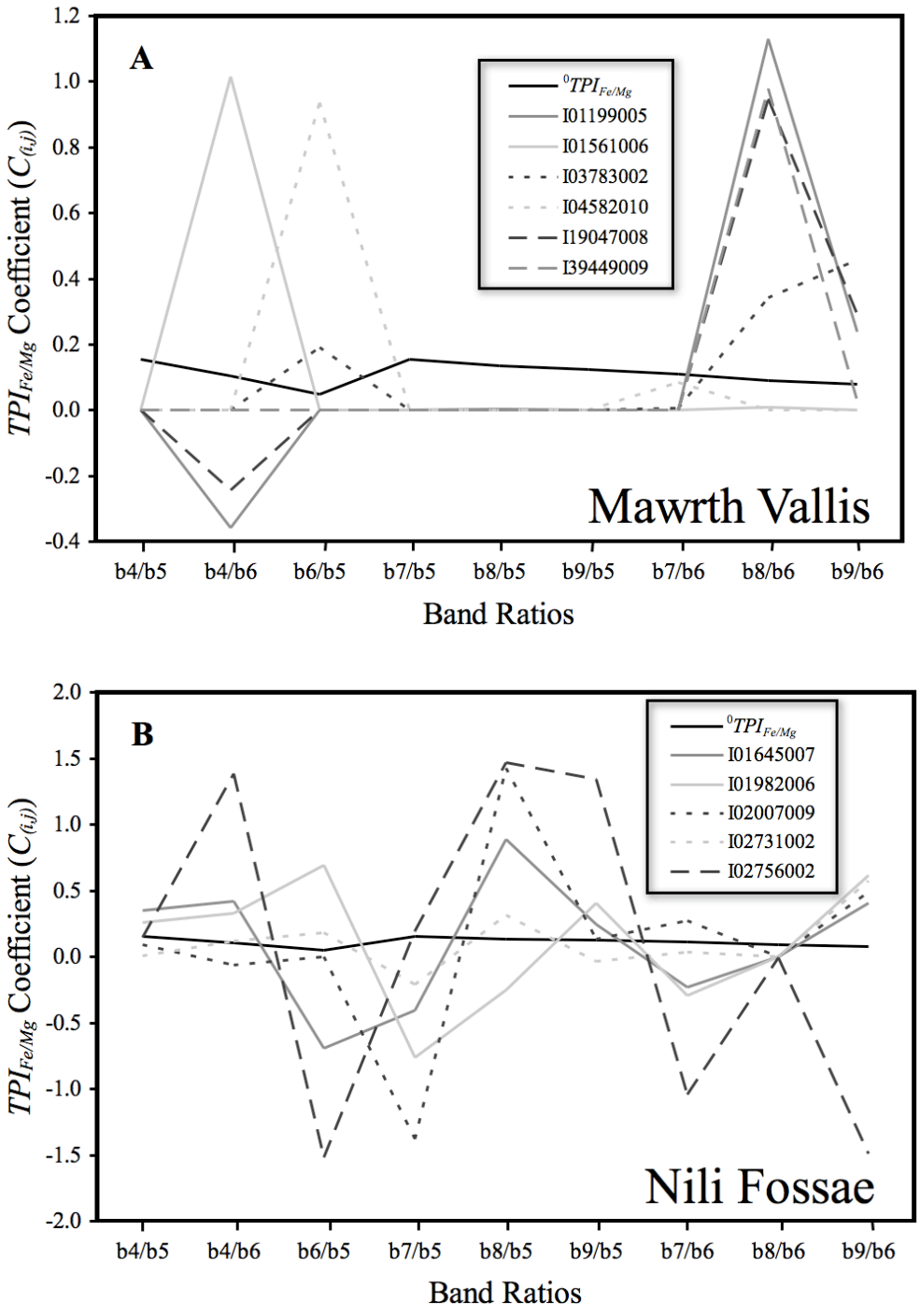

Figure A4. Optimized weighting coefficients of $TPI_{Fe/Mg}$ band ratios for individual THEMIS scenes, with $^0TPI_{Fe/Mg}$ coefficient values plotted for comparison. (a) $TPI_{Fe/Mg}$ coefficients for the Mawrth Vallis THEMIS scenes used in this study. (b) $TPI_{Fe/Mg}$ coefficients for the Nili Fossae THEMIS scenes used in this study. A potential explanation for the discrepancies between the two regions is discussed in section 3.2.

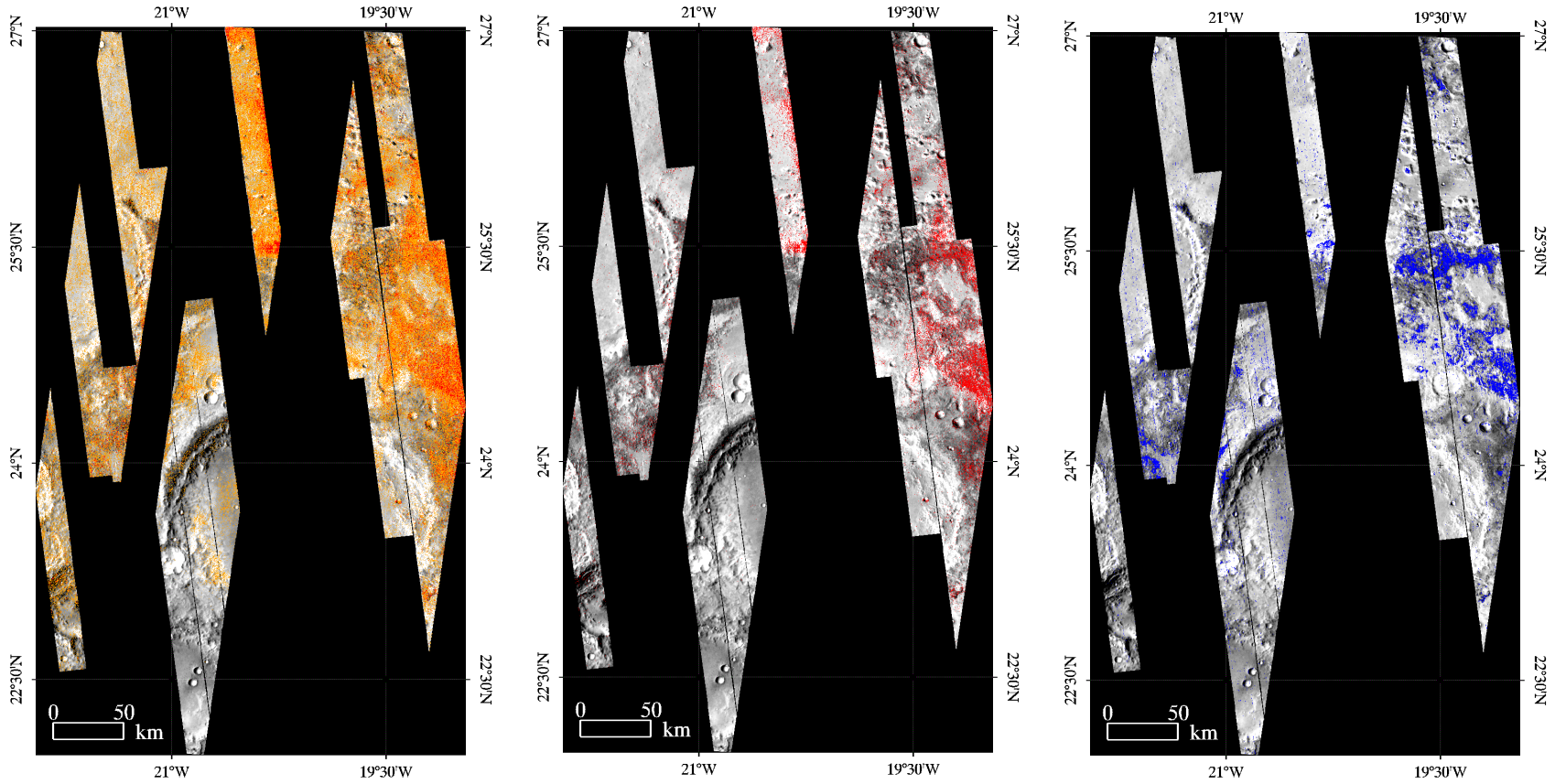

Figure A5. Comparison of $TPI_{Fe/Mg}$ and CRISM D2300 parameter mapping for the Mawrth Vallis region. The THEMIS brightness temperature image (background) covers the area of intersection between THEMIS daytime infrared and CRISM MSP data. (left) $TPI_{Fe/Mg}$ map: orange indicates values above ($c^* + 1\text{-}\sigma$), red indicates values above ($c^* + 2\text{-}\sigma$). (middle) only those pixels (red) with values above ($c^* + 2\text{-}\sigma$) are shown. (right) CRISM D2300 greater than zero (positive clay Fe/Mg-rich clay detections) are indicated in blue.

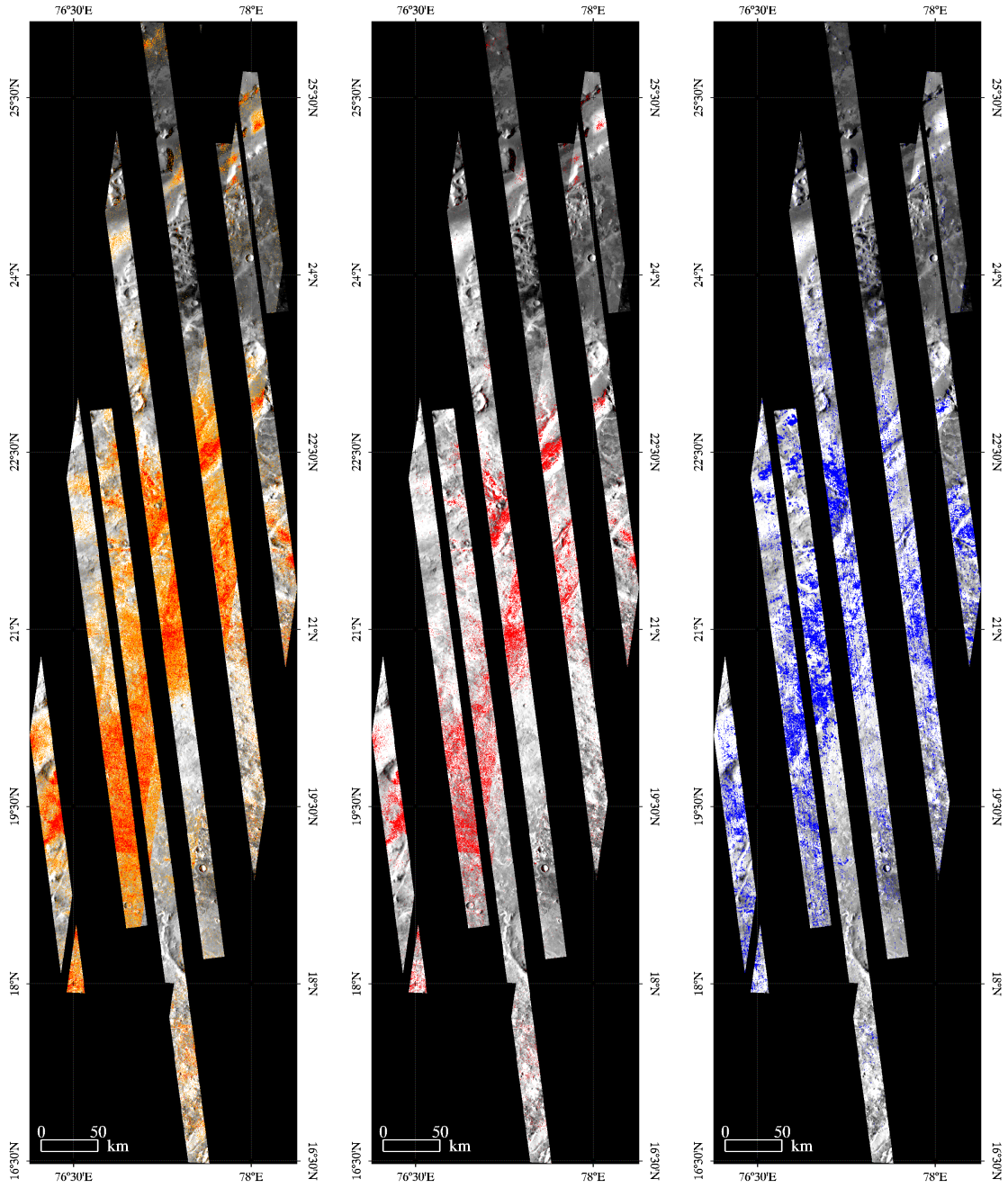

Figure A6. Comparison of $TPI_{Fe/Mg}$ and CRISM D2300 parameter mapping for the Nili Fossae region. The THEMIS brightness temperature image (background) covers the area of intersection between THEMIS daytime infrared and CRISM MSP data. (left) $TPI_{Fe/Mg}$ map: orange indicates values above ($c^* + 1\text{-}\sigma$), red indicates values above ($c^* + 2\text{-}\sigma$). (middle) only those pixels (red) with values above ($c^* + 2\text{-}\sigma$) are shown. (right) CRISM D2300 greater than zero (positive clay Fe/Mg-rich clay detections) are indicated in blue.

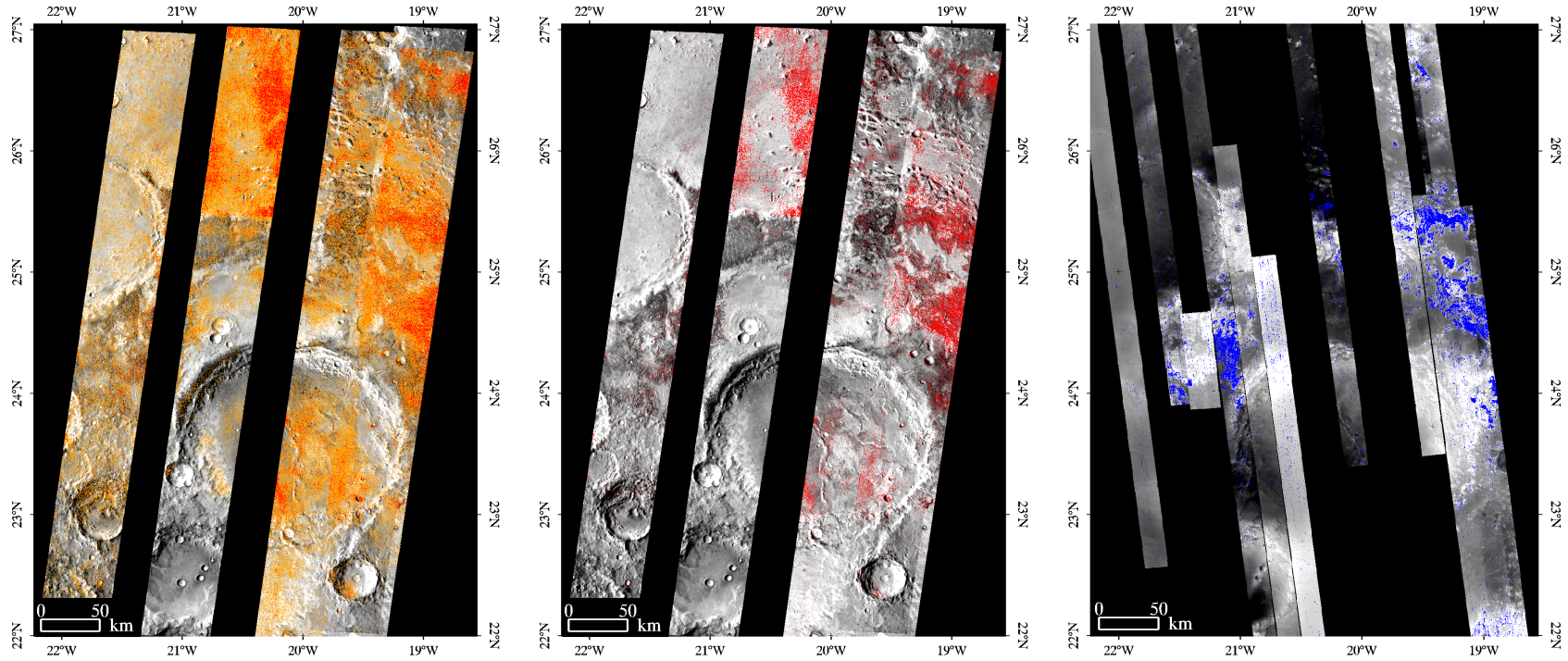

Figure A7. Extended mapping of the $TPI_{Fe/Mg}$ results for the Mawrth Vallis region. The entirely of all THEMIS brightness temperature images are used as a background (as opposed to just the areas of intersection with CRISM data). (left) $TPI_{Fe/Mg}$ map: orange indicates values above ($c^* + 1\text{-}\sigma$), red indicates values above ($c^* + 2\text{-}\sigma$). (middle) only those pixels (red) with values above ($c^* + 2\text{-}\sigma$) are shown. (right) CRISM D2300 greater than zero (positive clay Fe/Mg-rich clay detections) are indicated in blue; infrared albedo CRISM parameter [*Pelkey et al.*, 2007] used as background.

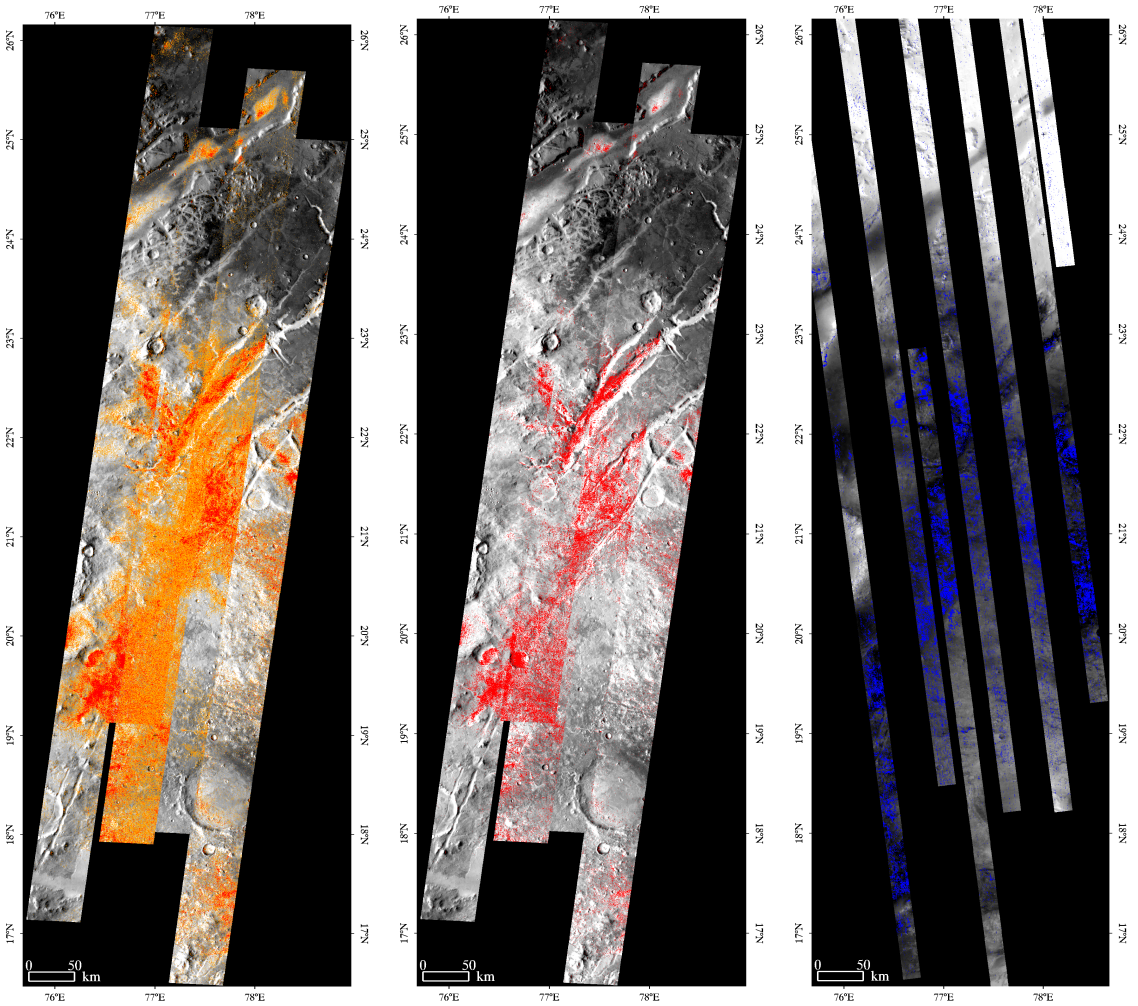

Figure A8. Extended mapping of the $TPI_{Fe/Mg}$ results for the Nili Fossae region. The entirely of all THEMIS brightness temperature images are used as a background (as opposed to just the areas of intersection with CRISM data). (left) $TPI_{Fe/Mg}$ map: orange indicates values above ($c^* + 1\text{-}\sigma$), red indicates values above ($c^* + 2\text{-}\sigma$). (middle) only those pixels (red) with values above ($c^* + 2\text{-}\sigma$) are shown. (right) CRISM D2300 greater than zero (positive clay Fe/Mg-rich clay detections) are indicated in blue; infrared albedo CRISM parameter [*Pelkey et al.*, 2007] used as background.

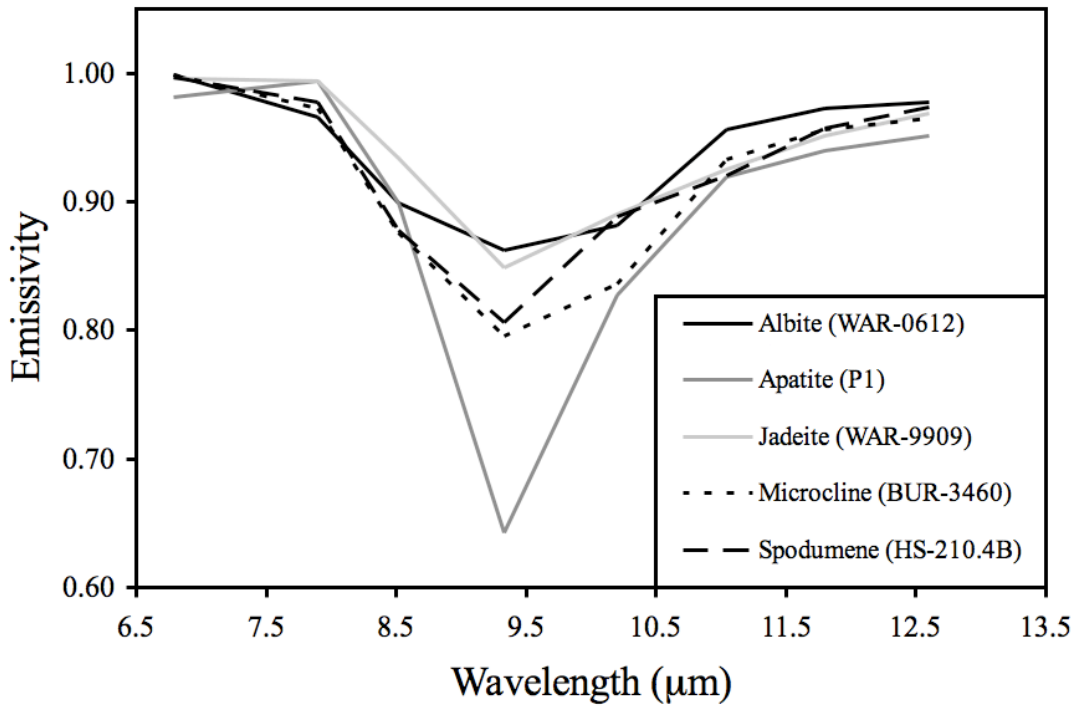

Figure A9. ASU library spectra [*Christensen et al.* 2000] of well-crystalline non-phyllosilicate minerals that yielded false positive detections as Fe/Mg-rich phyllosilicates with the ${}^{0}TPI_{Fe/Mg}$.

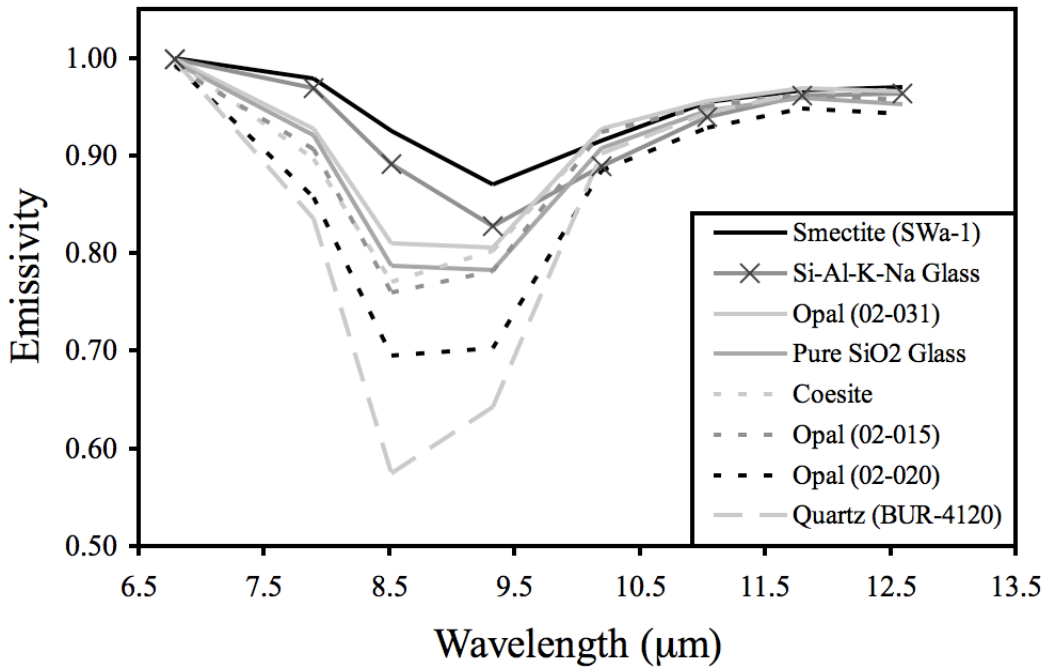

Figure A10. Laboratory spectra of high-Si phases [*Michalski et al.*, 2003], quartz [*Christensen et al.*, 2000], and glasses [*Wyatt et al.*, 2001] that qualify as false positives by the criterion described in section 4.2.

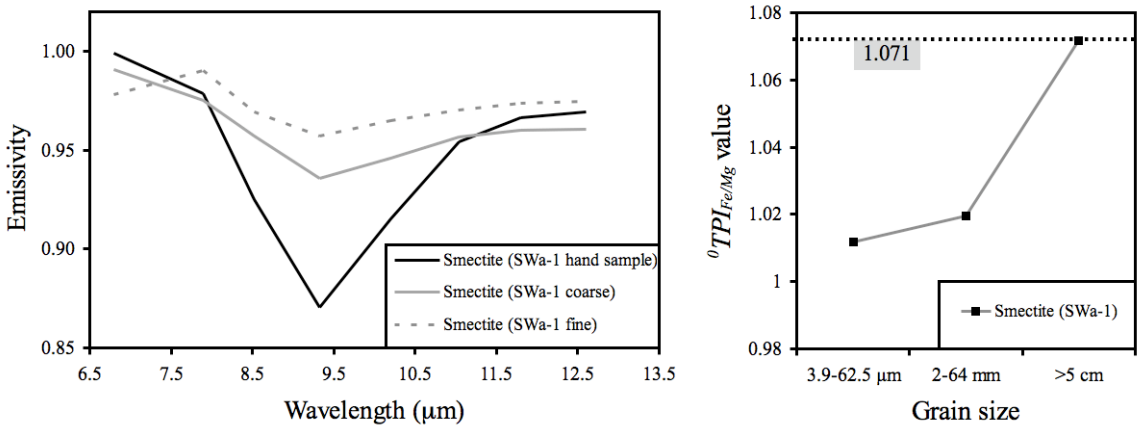

Figure A11. ASU library spectra of smectite at three grain-sizes (fine=silt-sized powder, coarse=coarse particulate, and hand sample). (left) Library spectra resampled to THEMIS bandpasses. Grain-size dependent spectral contrast is also resolvable at this spectral resolution. (b, right) Grain-size dependence of $^{0}TPI_{Fe/Mg}$ value, showing that fine and course grained smectite falls below the detection value (1.071).

Part 3
Using THEMIS resolution to resolve the discrepancy between CRISM/OMEGA and TES modeled phyllosilicate abundance in Mawrth Vallis

ABSTRACT

Here we explore the effects of spatial resolution on the detectability of phyllosilicates in the thermal infrared dataset from the Mars Global Surveyor Thermal Emission Spectrometer (TES). Data from the Mars Odyssey Thermal Emission Imaging System (THEMIS) instrument is used to resolve spatial resolution driven discrepancies between detection of phyllosilicates in the infrared and visible/near-infrared wavelength range. We show that the 100 m/pixel spatial resolution offered by THEMIS, even with its limited spectral resolution, significantly improves the likelihood of phyllosilicate detection. Furthermore, we use spectral unit mapping techniques to provide the first phyllosilicate abundance maps of the Mawrth Vallis phyllosilicate-bearing units and evaluate the proposed formation mechanisms for clay in this region using the geochemical evidence presented here.

1.0 INTRODUCTION

Characterizing the history of water on the surface of Mars is an important key to understanding the potential for past habitability of Mars. The recent availability of visible and near-infrared hyperspectral orbital data resulted in the identification and mapping of many examples of phyllosilicate-rich deposits [*e.g.*, *Poulet et al.*, 2005; *Bibring et al.*, 2006; *Loizeau et al.*, 2007; *Mustard et al.*, 2008], including smectite-rich material that is diagenetically unaltered [*Milliken et al.*, 2010]. On Earth, Fe/Mg-rich are not found in ancient rocks, as they transform to more stable phases such as illite or chlorite. The long-term stability of smectites on ancient terrains of Mars suggests that in the absence of plate tectonic activity, these less stable phases remain for much longer time periods than on Earth [*e.g.*, *Bish and Vaniman*, 2008]. While identifying the presence and areal distribution of these phyllosilicates reveals information about their environment of formation, quantifying their abundances in a deposit may further constrain past Martian environments, because significant phyllosilicate abundance suggests long-term contact between liquid water and rock to allow for the alteration of primary silicates into clays [*e.g.*, Velde et al. 1995].

The distribution and compositions of phyllosilicates on Mars have been mapped and measured using the Observatoire pour la Mineralogie, l'Eau, les Glaces et l'Activité (OMEGA) [*Bibring et al.*, 2004] instrument on board Mars Express, and the Compact Reconnaissance Imaging Spectrometer for Mars (CRISM) on board the Mars Reconnaissance Orbiter [*Murchie, et al.*, 2007a], both of which operate in the visible and near-infrared wavelength portion of the spectrum (0.362-9.92 μm and 0.35-5.2 μm for the two instruments, respectively). Recent work has also established the utility of using

thermal infrared (TIR, ~5-50 μm) spectroscopic orbital data to identify and map phyllosilicates on the surface [*e.g. Michalski and Fergason*, 2009; *Ruff & Christensen,* 2007; *Viviano & Moersch,* 2011]. *Ruff and Christensen* [2007] used data from the Mars Global Surveyor Thermal Emission Spectrometer (TES) [*Christensen et al.*, 2001] to map dioctahedral smectites via the presence of a doublet absorption feature at 530 and 465 cm^{-1} (18.9 and 21.5 μm). *Viviano and Moersch* [submitted 2011] showed that multispectral thermal infrared data from the Mars Odyssey THermal Emission Imaging System (THEMIS) [*Christensen et al.*, 2004] can also be used to map Fe/Mg-rich phyllosilicate distributions at moderate spatial resolution (100 m/pixel) via a THEMIS phyllosilicate index (TPI). The TES and THEMIS spectral index methods are useful for determining phyllosilicate distributions, but do not provide quantitative abundances of these phases. Abundance estimates have been made using both near-infrared [*e.g. Poulet et al.*, 2008] and thermal infrared data [*e.g.*, *Michalski and Fergason*, 2009] for phyllosilicate exposures in Mawrth Vallis, but the reported values do not agree. The purpose of the present work is to attempt to resolve this discrepancy by modeling the effects of different known or plausible instrument and surface properties on the reported abundances of phyllosilicates.

Previous work [*Michalski and Fergason*, 2009] has provided several theoretical hypotheses to explain the discrepancy between CRISM- and TES-derived abundances, but the large disparity in spatial resolution between these datasets left ambiguity as to which was the correct explanation. THEMIS multispectral infrared data provide a potential bridge for understanding this discrepancy because THEMIS utilizes the same spectral range as TES and has a spatial resolution closer to that of CRISM. The work

presented here consists of two parts. In the first part, we seek to understand the source of the significant discrepancy between phyllosilicate abundances reported from analysis of TES spectra and OMEGA/CRISM spectra. We examine the effects of surface temperature variability and scale of compositional mixing as observed at THEMIS spatial resolution to attempt to distinguish between the hypotheses provided by *Michalski and Fergason* [2009]. In the second part, we map the abundance of phyllosilicates in Mawrth Vallis from THEMIS multispectral data in order to assess the degree of alteration that occurred. Note that our work does attempt to resolve open questions about the presence or absence of phyllosilicates in TES Surface Type 2 (ST2) material [*Bandfield et al.*, 2000], where near-infrared datasets show no evidence for phyllosilicates but TES thermal infrared may (see *Michalski et al.* [2006] and *Ruff and Christensen* [2007] for a discussion of this topic). Rather, our work focuses on understanding the low TES-reported abundances of phyllosilicates in areas where CRISM and OMEGA show outcrops of phyllosilicate-bearing materials with strong absorption features.

1.1. Geologic context: Mawrth Vallis

The Mawrth Vallis region, located west of Arabia Terra, surrounds the Mawrth Vallis outflow channel, which dissects surrounding Noachian [*Scott and Tanaka*, 1986; *Edgett and Parker*, 1997] cratered terrain (Figure B1). Mawrth Vallis terminates at the Martian dichotomy boundary (hashed line, Figure B1) on the border of Chryse Planitia, the lowland plains to the north. The light-toned layered rock in this region was first suggested to be primitive outcrop of Martian crust based on Viking and Mars Observer Camera (MOC) image data (*Edgett and Parker* [1997], and *Malin and Edgett* [2000]; *Edgett and Malin* [2002], respectively). More recently, the mineralogy and

geomorphology of this region have been thoroughly characterized using CRISM, OMEGA, THEMIS, High Resolution Stereo Camera (HRSC), and Mars Orbiter Laser Altimeter (MOLA) topographic data [*e.g.*, *Loizeau et al.*, 2007; *Michalski and Noe Dobrea*, 2007; *Bishop et al.*, 2008; *Wray et al.*, 2008; *Michalski and Fergason*, 2009]. Two mineralogically distinct phyllosilicate-rich layers in the Noachian terrain have been identified: a lower unit containing Fe/Mg-rich smectite and an overlying unit containing Al-rich smectite [*Poulet et al.*, 2005; *Loizeau et al.*, 2007]. Both of these units are overlain by a spectrally-indistinct and physically resistant capping unit [*Loizeau et al.*, 2007]. The southern wall of the Mawrth Vallis channel exposes the stratigraphic relationships of these units, and their distinctive morphologies. The Al-rich smectite-bearing materials exhibits polygonal fracturing indicative of desiccation and/or thermal contraction, whereas the Fe/Mg-rich smectite-bearing unit is densely fractured and has possible remnants of impact craters [*Loizeau et al.*, 2007; *Wray et al.*, 2008]. In some locations the Fe/Mg-smectite bearing unit appears deformed, which has been interpreted as evidence for soft sediment deformation or folding of weaker layers as a result of strain [*Wray et al.*, 2008].

The phyllosilicate-bearing units have been interpreted to predate the formation of the Mawrth Vallis channel, and to be sedimentary and/or pyroclastic in origin [*Loizeau et al.*, 2007; *Michalski and Noe Dobrea*, 2007]. Alternatively, these units have also been suggested to drape the Mawrth Vallis channel [*Howard and Moore*, 2007], indicating they postdate the formation of the channel. *Wray et al.*, [2008] refined this interpretation, arguing that only the Al-clay bearing unit definitively drapes the channel (as determined by measuring the orientation of the Al-clay bearing unit across the region), and that the

lower Fe/Mg-clay bearing unit has an unknown orientation (as there is no observable contact between it and underlying units). The unresolved relationship between the Fe/Mg-clay bearing and underlying units leaves an ambiguity as to the timing of the deposition of the Fe/Mg-clay unit relative to the formation of this channel. The formation mechanism of the Al-clay bearing deposit also remains unresolved. If the Al-rich phyllosilicates formed *in situ*, their presence would be consistent with a zone of leaching and alteration [*e.g.*, *Noe Dobrea et al.*, 2008]. The Al-rich phyllosilicates may have also formed elsewhere and are sedimentary or pyroclastic in origin [*e.g.*, *Wray et al.*, 2008]. In this work, we aim to address these two hypotheses by characterizing the modal mineralogy of these units on a regional scale to identify whether the phases present are consistent or inconsistent with an alteration front [*e.g.*, *Noe Dobrea et al.*, 2008]. Regardless of the formation mechanism and relative age of unit emplacement, the abundance of phyllosilicates in these rocks and low abundance of primary minerals [*e.g. Poulet et al.* 2008] may reflect a high degree of alteration. The presence of two compositionally distinct clay-bearing units further implies heterogeneous environmental conditions (spatial and/or temporal) regardless of the formation mechanism.

1.2. Abundances of phyllosilicates from visible and near-infrared data

Poulet et al. [2008] modeled OMEGA spectra using Shkuratov radiative transfer theory [*Shkuratov et al.*, 1999], which accounts for the nonlinear multiple scattering that occurs in the near-infrared portion of the spectrum. Their results indicate up to 65% modal abundance of phyllosilicates (with an estimated accuracy of about +/- 10%) in outcrops in the Mawrth Vallis region. These abundances are comparable to preliminary estimates for phyllosilicates in the Mars Science Laboratory candidate Mawrth Vallis

landing ellipse, utilizing CRISM [*Ehlmann et al.*, 2011a] and OMEGA data [*Poulet and Carter*, 2011]. *Poulet et al.* [2008] have calculated the following ranges of phyllosilicate mineral abundances at ten locations in the Mawrth Vallis region: nontronite (not detected to 65%), montmorillonite (not detected to 20%), kaolinite (not detected to 20%), and illite (not detected to 15%). Other non-phyllosilicate components within the phyllosilicate-rich outcrops include ferrihydrite (5 to 25%), plagioclase (15 to 35%), dust (5 to 30%), and pyroxene (not detected to 15%) [*Poulet et al.*, 2008]. These OMEGA-derived abundances will be compared to the THEMIS-derived abundances presented here.

Variable states of hydration and hydroxylation in phyllosilicates affect spectra of these materials differently in the visible/near-infrared versus the thermal infrared wavelength regions. As phyllosilicate minerals are heated, adsorbed water is first driven from the interlayers; at higher temperatures dehydroxylation occurs. The near-infrared portion of the spectrum of phyllosilicates include absorption features due to both the hydroxide ion and adsorbed water, and therefore spectral changes occur when these minerals are heated to relatively low temperatures. For example, *Milliken and Mustard*, [2005] have shown that a sample of montmorillonite heated from room temperature to 100º C exhibits a decrease in spectral band depth in the 1.9 μm H_2O feature of ~50% due to the loss of adsorbed water. In the thermal infrared portion of the spectrum, absorptions due to the cation-OH bond are strong, whereas features associated with adsorbed water are weak [*Michalski et al.*, 2006] and appear at wavelengths shortward of the useful spectral range for TES and THEMIS. Thus, only those clays that have been heated to relatively higher temperatures display spectral changes observable by these instruments. For example, data presented by *Che et al.* [2011] show that a sample of montmorillonite

heated from room temperature to 100º C exhibits little change in spectral shape in the 1400-200 cm^{-1} wavelength range. Significant spectral changes only become apparent when the sample has been heated to ~500-600º C, the temperature at which spectral features in the thermal infrared begin to change due to dehydration and/or dehydroxylation for this sample. The difference in spectral behavior with heating for phyllosilicates in the near-infrared versus thermal infrared suggests that abundances determined from spectral unmixing of thermal infrared data may be more reliable for materials that have only experienced mild heating. *Ehlmann et al.* [2011b] have noted that the variability of phyllosilicate spectra with hydration state may contribute to inaccuracies in modeling of abundances in the near-infrared. In particular, problems could arise if the hydration states of the phyllosilicates used in the spectral library for modeling are different from the hydration states of phyllosilicates in the CRISM data.

1.3. Discrepancy between phyllosilicate abundances determined using visible/near-infrared and thermal infrared data

There are significant discrepancies between spectral interpretations of surfaces in the visible and near-infrared when compared to thermal infrared observations. *Ruff and Christensen* [2007] used absorption features at 465 and 530 cm^{-1} to suggest the presence of dioctahedral smectite in Mawrth Vallis. However, spectral unmixing of TES data from this region results in clay abundances near the TES threshold of detection (~15%) [*Michalski and Fergason,* 2009]. As described in the previous section, *Poulet et al.* [2008] have modeled 40-65% clay using OMEGA data in this same region. Potential factors that may account for this discrepancy are described by *Michalski and Fergason* [2009]:

Hypothesis 1) *Sub-pixel temperature differences (at TES spatial resolution) in phyllosilicate-rich and phyllosilicate-poor surfaces.* When a multi-compositional surface is isothermal within a TES pixel, the spectral radiance contributions of each component will be proportional their sub-pixel areal abundances. However, if sub-resolved phyllosilicate-rich surfaces are cooler than their surroundings, they will under-contribute to the total radiance relative to their areal abundance. This potential temperature discrepancy can result in significant under-reporting of modeled phyllosilicate abundances because of the strong dependence of radiance on surface temperature. THEMIS provides evidence that clay-rich surfaces in Mawrth Vallis are indeed significantly cooler than their surroundings. THEMIS scene I01199005 (centered ~25º N, 19º W), for example, shows phyllosilicate-rich surfaces with an average temperature of 248 K and surrounding material with an average temperature of 256 K. Even this small difference in temperature is sufficient to provide a factor of 1.17 difference in peak radiance emitted by the two surfaces. *Michalski and Fergason* [2009] suggest the resulting under-reporting of TES abundances for sub-resolved, cooler phyllosilicate exposures would be sufficient to account for the discrepancy between TES and OMEGA/CRISM abundances. THEMIS data, with its superior spatial resolution to TES, may be used to evaluate whether such temperature heterogeneities occur at a scale >100 m/pixel, favoring this hypothesis.

Hypothesis 2) *Low absolute phyllosilicate abundance (at TES spatial resolution)*. The relatively low clay mineral abundances reported from TES spectral unmixing (described above) may be attributed to either ***a)*** *low but evenly distributed phyllosilicate abundance within deposits* (intimate mixing), or ***b)*** *sub-pixel mixing of relatively high-*

abundance phyllosilicate materials interspersed amongst predominantly phyllosilicate-poor material (checkerboard mixing). *Hypothesis 2b* can be addressed using the higher spatial resolution THEMIS data to look for checkerboard mixing at the >100 m scale.

Michalski and Fergason [2009] also present a *Hypothesis 3*, suggesting that the surface texture of the clay-bearing unit may oppositely affect detectability in the two wavelength regions [*e.g.*, *Cooper and Mustard*, 2002]. In the near-infrared, fine-grained surface textures promote multiple scattering, leading to deeper absorption features that enhance detectability. In the thermal infrared, absorption features lose spectral contrast with decreasing grain size as the size becomes comparable to the wavelength of emitted light [*e.g.*, *Vincent and Hunt*, 1968; *Moersch and Christensen*, 1995; *Mustard and Hayes*, 1997]. This relationship between grain size and spectral contrast is equally true for TES and THEMIS data as they both utilize the same wavelength range, and therefore THEMIS data provide no addition information for testing *Hypothesis 3*.

On the other hand, THEMIS data may be used to test *Hypotheses 1*, *2a* and *2b*. Although TES data have a much higher spectral resolution than THEMIS data and can be used to discriminate different mineral species more readily, the high spatial resolution of THEMIS is useful for phyllosilicate detection because less mixing of phyllosilicate-bearing outcrop and surrounding materials occurs at the 100-m scale. To test *Hypotheses 1*, *2a*, and *2b*, we model sub-pixel temperature variations and quantify the observational biases produced by the different spatial resolutions of CRISM, THEMIS, and TES on modeled abundances of phyllosilicates, which allows us to estimate the increased sensitivity to phyllosilicates THEMIS may provide over TES. *Hypothesis 2b* (checkerboard mixing) describes a baseline effect of simple "blurring" at lower spatial

resolution, which is unavoidable, but may not be enough to explain the discrepancy itself. *Hypotheses 1* and *2a* include additional effects that would act to further decrease the phyllosilicate abundances reported by TES.

1.4. Deconvolution of thermal infrared spectra for mapping mineral abundances

Results from modeling the detectability of phyllosilicates from the first part of our work provides confidence in using THEMIS data for spectral unmixing, particularly in Mawrth Vallis. While phyllosilicate abundances in this area have been estimated using visible and near-infrared spectroscopy (section 1.2), one key advantage of thermal infrared spectroscopy is the fact that spectra of mixtures can be modeled as a linear combination of their individual components [*e.g.*, *Thomson and Salisbury*, 1993; *Ramsey and Christensen*, 1998; *Feely and Christensen*, 1999; *Hamilton and Christensen*, 2000]. *Thomson and Salisbury* [1993] showed linear deconvolution on laboratory resolution spectra of particulate mixtures could be used to quantitatively determine mineral abundances within ~5%. Linear deconvolution of laboratory spectra of whole rocks has also been confirmed and is accurate to 5-10% [*e.g.*, *Feely and Christensen*, 1999; *Hamilton and Christensen*, 2000; *Wyatt et al.*, 2001; *Hamilton et al.*, 2001]. *Feely and Christensen* [1999] successfully determined the mineral composition and abundance for 96 unpolished and uncut igneous and metamorphic rocks within 8-14% for different mineral phases. This analysis was replicated using 10-band THEMIS-like resolution for the same hand samples, demonstrating that mineral abundance could still be determined within 15% using only 10 spectral bands [*Christensen et al.*, 2004]. However, deconvolutions of multispectral data are mathematically limited to reporting abundances for N candidate endmember spectra, where N is the number of useful spectral bands [*e.g.*,

Ramsey and Christensen, 1998]. Spectral unit maps of each MSL candidate landing site, including the Mawrth Vallis region, have been made using THEMIS data by *Rogers and Bandfield* [2009]. Rather than using laboratory spectra of known minerals in their unmixing, they used image endmembers derived from THEMIS emissivity data, identified as mappable units with decorrelation stretching [*Gillespie et al.*, 1986]. Thus, the resultant abundance maps were for abundances of scene-derived spectral endmembers, not specific mineral phases. To determine the mineralogic composition of these scene-derived endmembers, *Rogers and Bandfield* [2009] averaged TES spectra for the same areas that they used to define the THEMIS spectral endmembers. Their TES unmixing results were comparable to those of *Michalski and Fergason* [2009], which are inconsistent with OMEGA/CRISM observations (see section 1.3). The *Rogers and Bandfield* [2009] approach to spectral unmixing of THEMIS data is fundamentally different from the method we use in that our unmixing makes use of laboratory spectra rather than image spectra as endmembers. Because mineral identifications in the *Rogers and Bandfield* [2009] study were based on deconvolution of TES data at 3 km/pixel, they were unable to resolve the presence of phyllosilicates in any of their endmembers.

2.0 DATA AND METHODS

2.1. THEMIS data processing

THEMIS daytime infrared images were converted to emissivity and atmospherically corrected using the jENVI software package (http://arsia.gg.utk.edu/~utmars/jenvi/), which implements a custom TES-derived multiplicative correction utilizing the approach described in [*Bandfield et al.*, 2004a].

Only those images with the highest average temperatures (a minimum of 245 K) and the lowest average atmospheric dust and water ice opacities (less than 0.15) were used. Scenes were also filtered to exclude those with significant localized atmospheric dust and water ice contributions (as determined with a linear unmixing of the scene using TES derived canonical spectral endmembers of *Bandfield* [2000]) over the phyllosilicate-rich deposits. For our study of phyllosilicates in Mawrth Vallis, the following THEMIS daytime infrared images met these criteria: I01199005, I01561006, I19047008, and I39449009.

2.2. CRISM data processing

CRISM full-resolution targeted (FRT) data and multispectral/push-broom survey (MSP) data were processed with the CRISM Analysis Toolkit (CAT) interface (http://pds-geosciences.wustl.edu/missions/mro/crism.htm#Tools). Data were converted to I/F (a ratio of measured spectral radiance to the incoming solar flux) and photometrically corrected using the procedures described by *Murchie et al.* [2007a, 2007b]. The data were atmospherically corrected utilizing the 2-μm CO_2 feature as described in the supplemental materials from *Langevin et al.* [2006]. A spectral and spatial noise removal routine was also applied to the data [after *Parente*, 2008]. Spectral parameters from *Pelkey et al.* [2007] were applied to the corrected CRISM images to map hydrated minerals. Specific clay species (Fe/Mg-OH vs. Al-OH) were identified using the D2300 parameter (drop at 2.3 μm) and the BD2210 parameter (band depth at 2.21 μm) [*Pelkey et al.*, 2007].

2.3. Phyllosilicate detection discrepancy modeling

To test *Hypotheses 1*, surface temperatures were modeled using THEMIS image I01199005, chosen for its low atmospheric opacity, significant coverage over the phyllosilicate-rich outcrops in Mawrth Vallis, and past successful use in resolving spectral variations in the phyllosilicate-rich material [*e.g.*, *Viviano and Moersch*, 2011]. The image was initially processed using the techniques described in section 2.1, and subset to the area overlapping with CRISM Full Resolution Targeted (FRT) image frt0000b643_07. This FRT scene was processed using the techniques outlined in section 2.2, and the D2300 parameter for that scene was calculated and mapped. For ease of spatial resolution degradation, the typical bow-tie shape of the CRISM FRT stamp and the parallelogram shape of the THEMIS scene were simply cropped to a rectangle that included the overlapping regions.

To evaluate *Hypothesis 1* (sub-pixel temperature differences), the D2300 parameter map from a CRISM scene was used to create a mask for a realistic spatial distribution of phyllosilicates at an 18-m/pixel scale. Wherever the D2300 parameter detected phyllosilicates in the CRISM scene, the surface was spectrally modeled in the thermal infrared as 30% Surface Type 1 (ST1) [*Bandfield et al.*, 2000] and 70% nontronite (SWa-1, Arizona State University (ASU) spectral library [*Christensen et al.*, 2000a]). Our spectra model utilizes the highest abundance of nontronite modeled by *Poulet et al.* [2008], and therefore provides the most conservative test of the hypothesis (see section 3.1). All other (non-phyllosilicate) pixels in the scene were modeled as 100% ST1. In order to test the effects of sub-pixel temperature mixing in the thermal infrared, radiance spectra were generated for the two surfaces, using a temperature of 248

K for the phyllosilicate-rich (70% nontronite, 30% ST1) surfaces and 256 K for the non-phyllosilicate (100% ST1) surfaces. These temperatures were derived from averaged temperatures for areas corresponding to phyllosilicate-rich and non-phyllosilicate surfaces in scene I01199005. Using the mask of phyllosilicate distribution and radiance spectra appropriate for the compositions and temperatures described above, we created a model thermal infrared radiance image cube at 10 cm^{-1} spectral resolution and 18 m/pixel spatial resolution (Figure B1, row 1, left panel). This model radiance image cube was spatially degraded from CRISM spatial resolution to THEMIS spatial and spectral resolutions (Figure B1, row 1, center panel) and to TES spatial resolution (Figure B1, row 1, right panel). The model radiance image cubes were subsequently converted to emissivity by the maximum brightness temperature approximation method [*e.g.*, *Christensen et al.*, 2001; *Bandfield et al.*, 2004]. This conversion is achieved by dividing the radiance spectrum by a Planck curve fit to the maximum brightness temperature calculated from the radiance spectrum. The resulting emissivity cubes were linearly unmixed (see section 2.2 for a description of this technique) to derive modeled abundances of ST1 and nontronite at each tested resolution. The abundances derived from unmixing were compared to the abundances used in the input (18 m/pixel) image cube to assess the degree to which cooler components of the surface (phyllosilicates, in this case) are underrepresented when observed at the lower spatial and/or spectral resolutions of THEMIS and TES.

To model *Hypothesis 2a* (intimate mixing, with no variation in surface temperature), the measured band drop of the 2.3-μm absorption feature (the CRISM D2300 parameter) was used to crudely approximate weight percent of phyllosilicates for

a model consisting of mixtures of nontronite (45 μm) and basalt (45 μm), using the relationship presented in *Ehlmann et al.* [2011a]. This approximation is admittedly crude because it does not take into account actual particle size distributions; nevertheless, it is a useful assumption for providing a first-order assessment of the viability of *Hypothesis 2a*. When the *Ehlmann et al.* [2011a] relationship was applied to CRISM scene frt0000b643_07 phyllosilicate abundances ranging from 0 to 55% were mapped (B 2, row 2, left panel). These abundances were used to create a model thermal infrared image cube at 18 m/pixel spatial resolution, using spectra of ST1 and nontronite at 10 cm^{-1} spectral resolution. This model image cube was spatially degraded to THEMIS and TES spatial resolutions and linearly unmixed to map phyllosilicate abundances as they would be reported at these lower resolutions (Figure B1, row 2, center and right panels). These results were compared to the input abundances to evaluate the effects of sub-pixel abundance variations on the THEMIS- and TES-reported abundances.

Finally, to evaluate the baseline *Hypothesis 2b* (simple "blurring" due to sub-pixel checkerboard mixing), a model image cube was created with the same compositions and abundances used in testing *Hypothesis 1* (100% ST1 for non-phyllosilicate surfaces, and 70% nontronite, 30% ST1 for phyllosilicate-rich surfaces), but with no temperature variations (Figure B2, row 3, left panel). This model image cube was spatially degraded to THEMIS and TES spatial resolutions and linearly unmixed to map phyllosilicate abundances (Figure B2, row 3, center and right panels). The *Hypothesis 2b* models provide an assessment of the degree to which phyllosilicate abundances are underreported at these lower spatial resolutions in the absence of any other effects.

2.2. THEMIS spectral unmixing of phyllosilicate-bearing units

The goal of the second part of this work is to use THEMIS thermal infrared multispectral data to map phyllosilicate abundances in Mawrth Vallis. THEMIS emissivity images can be modeled using a least square linear mixing routine to give abundances of surface components. This unmixing technique has been successfully applied to laboratory spectra of mineral mixtures and rocks to determine modal mineralogy (see section 1.4). Linear spectral unmixing is limited to modeling N spectral components, where N is the number of unique spectral bands; unmixing includes a blackbody endmember. For THEMIS, there are six unique bands; bands 1, 2, 3, and 10 are excluded because those bands are either too noisy, used as a normalization in the atmospheric correction, or insensitive to the spectral nature of the surface. THEMIS emissivity scenes were subset to those regions identified as phyllosilicate-rich by CRISM MSP data and OMEGA mapping from *Loizeau et al.*, [2007], which are co-located with the light-toned unit identified in *Michalski and Fergason* [2009]. We identified individual mineral spectra to act as proxies for the endmember mineral groups used by *Michalski and Fergason* [2009]: feldspars, pyroxenes, high-silica phases, clay minerals, zeolites, and 'other'. In their work, *Michalski and Fergason* [2009] identified the spectrally dominant components of the light-toned unit by modeling several trial compositions, all identical except for the absence of a different single component in each one. Components were judged to be spectrally important if the spectrum of the light-toned unit was poorly modeled when that component was not included. The results from their modeling of endmembers are presented in Table B1.

For our abundance modeling in Mawrth Vallis, we chose representative minerals, mostly from the Arizona State University (ASU) Thermal Emission Spectroscopy Laboratory Spectral Library [*Christensen et al.*, 2000a] resampled using the THEMIS bandpasses [*Christensen et al.*, 2004], as proxies for each of the mineral groups identified by *Michalski and Fergason* [2009]. Labradorite (BUR-3080A, ASU spectral library) is representative of the feldspar group, as *Milam et al.* [2010] identified that ~An_{60} is the most dominant phase on Mars, virtually identical in ST1 and ST2 terrains. Although *Michalski and Fergason* [2009] modeled feldspar best with an average of oligoclase in these units, our initial unmixing with this endmember resulted in relatively poor modeling of the THEMIS spectra. Augite (HS-119.4B) was used for the pyroxene group as TES compositional mapping identifies high-calcium pyroxene in this region [*Bandfield*, 2002]. *Michalski and Fergason* [2009] favor the hypothesis that the high-silica phase, consistent with felsic glass or aluminous opaline silica, is likely the former, as OMEGA and CRISM analysis do not show significant hydrated-silica phases in the light-toned rocks. Therefore, we used alkali glass [*Wyatt et al.*, 2001] as our proxy spectral endmember. Both montmorillonite and nontronite (SWy-2 and WAR-5108, ASU spectral library) were used as two separate clay endmembers, representing the aluminous and ferruginous phyllosilicates in Mawrth Vallis first identified by *Poulet et al.*, [2005]. Heulandite from the Johns Hopkins University (JHU) Mineral Spectral Library [*Salisbury et al.*, 1991] (converted to reflectance using Kirchhoff's Law, $\varepsilon = 1 - R$) was used as the zeolite endmember as it was also well modeled in TES unmixing [*Michalski and Fergason*, 2009]. The 'other' mineral group was characterized by average Martian surface dust [*Bandfield and Smith*, 2003].

An assessment of the dominant spectral components in THEMIS scenes I01199005, I01561006, I19047008, and I39449009 from Mawrth Vallis was made using the same approach as *Michalski and Fergason* [2009] use for TES data, *i.e.*, multiple models using the same endmember set minus a different trial component in each to evaluate which components were most important. This operation was necessary since it is only possible to linearly unmix 6 endmembers with THEMIS data. The assessment was performed for two different endmember sets, one using montmorillonite as the phyllosilicate endmember and the other using nontronite. A blackbody endmember was also included to account for variations in spectral contrast. However, this phase was not incorporated into the actual abundance calculation, which was normalized to 100% using just the six endmembers.

2.3. Assessing the significance of spectral linear unmixing result

Eliminating a single endmember from each unmixing trial allows for the assessment of the relative importance of that endmember, by comparing the error between the measured emissivity spectrum and the modeled spectrum. Typically, the residual error from a spectral linear deconvolution can be expressed as the root-mean-square (RMS) error. For an instrument with m wavelength channels, RMS error is expressed as:

$$RMS = \sqrt{\sum_{j=1}^{m} (\varepsilon_{j\_measured} - \varepsilon_{j\_\mathrm{mod}eled})^2 / m},$$

where ε_j is the emissivity at a particular wavelength channel, j [Ramsey and Christensen, 1998]. We note that it has been shown that the RMS error may be misleading when considering spectra with different spectral contrast, as higher contrast spectra result in

higher RMS values for the same fit [*e.g.*, *Koeppen and Hamilton*, 2005]. Therefore, the mean percent error (MPE) of each phase modeled is also reported here, as it measures relative error, independent of spectral contrast. This measurement of error is expressed as:

$$MPE = \frac{1}{m}\sum_{j=1}^{m}\frac{\left|\varepsilon_{j\_\mathrm{mod}eled} - \varepsilon_{j\_measured}\right|}{\varepsilon_{j\_measured}},$$

again where ε_j is the emissivity at a particular wavelength channel, j, for an instrument with m wavelength channels.

3.0 RESULTS

3.1. Phyllosilicate detection discrepancy modeling results

Figure B2 shows the effects of different sub-pixel characteristics (those considered in *Hypotheses 1*, *2a*, and *2b*) on abundances of phyllosilicates reported at THEMIS and TES resolutions. As expected, simple checkerboard mixing or "blurring" (*Hypothesis 2b*) associated with the lower spatial resolutions of THEMIS and TES (relative to CRISM) results in a significant decrease in reported phyllosilicate abundances. Of all three tested hypotheses, the spatially degraded model image cube for *Hypothesis 2b* results in the greatest likelihood of detection at the TES resolution (Figure B2, row 3, right panel), where five pixels in the model exhibit phyllosilicate abundances greater than the TES limit of detection (15%). The maximum abundance modeled for a single pixel at THEMIS resolution (63%) and TES resolution (46%) provides a baseline value for comparison with abundances modeled for *Hypotheses 1* and *2a*, as the effects of "blurring" are present in the modeling used to test all three hypotheses. These values are

underreported by 7% and 24% (for THEMIS and TES, respectively) compared to the input model abundances at CRISM spatial resolution.

By modeling the effects of temperature variations on the surface (*Hypothesis 1*), and crudely approximated abundance distributions of phyllosilicates (*Hypothesis 2a*), we can assess which of these two factors is most important in causing additional underreporting of phyllosilicate abundances in the TES data. The results of our model of sub-pixel temperature heterogeneities (Figure B2, row 1), which include the same spatial resampling, have reported phyllosilicate abundances at THEMIS and TES spatial resolutions that are only slightly less than those obtained when only the effects of spatial resolution are considered (Figure B2, row 3). On the other hand, modeling of sub-pixel phyllosilicate abundance variations (*Hypothesis 2a*) reveals significantly greater underreporting of phyllosilicate abundances with decreasing spatial resolution. In our model, no phyllosilicate abundance exceeds 10% at TES spatial resolution, below the TES limit of detection of ~15% [*Christensen et al.*, 2000b]. There are some pixels in the THEMIS resolution model that remain above the THEMIS detection limit, lending credibility to the idea that THEMIS data could be used to map phyllosilicates in areas where TES data reveal none.

3.2. Phyllosilicate abundance map for Mawrth Vallis

The detailed THEMIS unmixing results averaged over all the light-toned materials are organized by THEMIS scene and reported in Tables B2-B5. The exclusion of zeolite provided the most consistently low RMS and MPE values, indicating the phase is least important in modeling the THEMIS emissivity spectrum. Conversely, the exclusion of feldspar or 'other' (surface dust) provided the highest RMS and MPE values,

indicating they are important phases for modeling. We also present these mineral proportions graphically in Figure B3 as pie charts, including the TES spectral unmixing results [*Michalski and Fergason*, 2009] for comparison. Each group was averaged from all of the unmixing trials for one scene (leaving out the trial that excluded the particular endmember being calculated) and was normalized to 100%. This averaging was done separately for the trials that used nontronite as the clay endmember, versus those that used montmorillonite. Averaged from all of the unmixing trials for *all* of the scenes (leaving out those that excluded clay), nontronite was modeled as 17.8(±10.9)% and montmorillonite as 11.4(±6.9)%. This average, and the averages from the individual scenes (presented in Figure B3) are consistent with TES unmixing results within error, and are very near or below the TES limit of detection.

While scene averages are reported in Tables B2-B5 and Figure B3, individual pixels of each THEMIS scene were unmixed and the results for the clay group are presented in Figure B4. The left panel of this figure reveals the distribution and abundance of nontronite, modeled for those areas identified as phyllosilicate-rich using OMEGA or CRISM data. Although averages reported in Tables B2-B5 and Figure B3 indicate nontronite modeled at the limit of detection, mapping of individual pixels utilizes the full advantage of THEMIS resolution, indicating significant amounts of nontronite in the 40-60% abundance range. This result may be compared to the center panel, revealing the abundance of montmorillonite modeled. As with the averaged data, the unmixed individual pixels reveal lower abundance montmorillonite than nontronite, with the upper range falling between 20-40%.

4.0 DISCUSSION

4.1. Resolution of discrepancies in CRISM/OMEGA versus TES reported phyllosilicate abundances

The results presented in section 3.1 show that spatial resolution effects alone are insufficient to explain the significant discrepancy in reported abundances of phyllosilicates from the OMEGA/CRISM experiments and TES. The model used to test *Hypothesis 2b* shows that several TES pixels in Mawrth Vallis should have revealed phyllosilicates above the threshold of detectability if the discrepancy was solely due to spatial resolution effects. Further, our model of sub-pixel temperature heterogeneities also resulted in several positive detections at TES resolution, indicating that this effect is insufficient to explain the discrepancy. Reported TES phyllosilicate abundances only fall below the limit of detectability when sub-pixel modal abundance variations in the phyllosilicate-rich unit are considered (*Hypothesis 2a*).

The analysis above suggests that *Hypotheses 1* and *2b* of *Michalski and Fergason* [2009] are insufficient to explain the OMEGA/CRISM and TES discrepancy in reported phyllosilicate abundances, leaving *Hypotheses 2a* and *3* as the remaining possible explanations. *Hypothesis 3* is not explicitly tested in our modeling study, however some THEMIS pixels in the second part of our study (section 3.2) show phyllosilicate abundances well above the limit of detection. These occurrences suggest that particle size effects are not the reason TES fails to detect phyllosilicates because these effects would be the same in TES and THEMIS data. So, by the process of elimination, *Hypothesis 2a* of *Michalski and Fergason* [2009] is the most likely explanation for the lack of phyllosilicate detections in TES data.

4.2. Potential advantages for THEMIS phyllosilicate abundance mapping

Comparison of the left, center, and right columns in Figure B2 suggests advantages may be realized in using THEMIS data to map phyllosilicate abundances. For all three of the effects modeled, abundances reported at THEMIS resolution are ~20% higher than those reported at TES resolution. In each case, the THEMIS-reported abundances are much closer to the input abundances. The comparable abundance distributions suggest that the 100-m spatial resolution of THEMIS is sufficient to resolve the characteristic length scale of phyllosilicate heterogeneity on Mars, whereas the 3-km spatial resolution of TES is not.

In general, the detectability of phyllosilicates depends on the sub-pixel areal abundance of phyllosilicate-bearing materials, as well as the modal abundance of phyllosilicates in the phyllosilicate-bearing materials. Both THEMIS and TES have modal abundance limits of detection at ~15% when their pixels are completely filled with a homogenous composition. The modal abundance of phyllosilicates necessary for detection increases when the phyllosilicate-rich materials fill only a portion of a pixel. These relationships are represented graphically in Figure B5, modified from *Michalski and Fergason* [2009]. The solid-filled area in this plot shows the range of phyllosilicate modal abundances and areal coverage that would be detectable in TES data. The hashed area shows the improvement in detectability offered by the higher spatial resolution of THEMIS data. Although both THEMIS and TES are insensitive to units with less than 15% clay modal abundance, as that abundance increases, the THEMIS detectability improves significantly as compared to TES. Increased sensitivity is particularly noticeable in the case of units that fill small portions of a TES pixel, but are relatively

clay-rich. Note that the fields shown in Figure B5 only indicate detection vs. non-detection of phyllosilicates. The modeling work previously discussed demonstrates that even in areas where detections are made, phyllosilicate abundances may be underreported.

The analysis above suggests that THEMIS data are superior for mapping phyllosilicates, however, the lower spectral resolution of THEMIS offsets some of the advantages offered by its higher spatial resolution. The 15% THEMIS detection limit considered above was derived from a laboratory study [*Christensen et al.*, 2000a] that utilized all 10 THEMIS spectral bands; in practical application only 6 THEMIS bands are useful, limiting the number of spectral endmembers that can be used to linearly unmix the spectra. With so few bands, the importance of selecting the correct endmember spectra for unmixing becomes critical. Cross-wavelength analyses that use CRISM and TES data to identify specific mineral endmembers and THEMIS data to quantitatively determine abundances may provide the most robust results.

4.3. Abundance of phyllosilicates modeled by THEMIS

As described in section 3.2, the overall average of each clay component modeled with THEMIS unmixing (17.8(±10.9)% nontronite and 11.4(±6.9)% montmorillonite), and the averages from the individual scenes (Figure B3) are identical to TES unmixing results within error, and are very near or below the TES limit of detection. This trend is consistent with our modeling of the diminishing detectability with decreasing spatial resolution, as averaging together all of the THEMIS unmixing results is the same as lowering the resolution (*e.g.*, to TES pixel size). The consistency between the averaged

modeled THEMIS unmixing results and the TES modeled abundance of clay provides further confidence in the THEMIS unmixing results at the pixel level.

The abundance of clay components mapped at the THEMIS pixel level (100 m/pixel) reveals differences between the Fe/Mg-rich clay endmember (nontronite) and the Al-rich clay endmember (montmorillonite) used in the modeling. In the nontronite map (Figure B4, left) there is a significant number of pixels that fall within the 40-60% abundance range, whereas in the montmorillonite map (Figure B4, center) most fall within the 20-40% range. These results appear consistent with those few tested areas reported by *Ehlmann et al.* [2011], *Poulet and Carter* [2011], and *Poulet* [2008], as determined by modeling CRISM and OMEGA data (see section 1.2). The straightforwardness of unmixing thermal infrared spectra allows us to map the abundance over the full THEMIS coverage and assess clay abundance with geologic context.

The clay abundance observed by CRISM and OMEGA and now verified using THEMIS observations across the clay-rich deposits may help to explain the water equivalent hydrogen derived by *Feldman et al.* [2004] enhancement in Arabia Terra. Bish *et al.* [2003] calculated the current possible water content that would be stable in montmorillonite. Modeling by *Fialip et al.* [2005] indicated Al-rich smectites would have to be present in abundances of 30-40% to account for this enhancement. Mg-rich smectites have not been modeled for stability of water due to limited thermodynamic data for these phases, but *Bish et al.* [2003] reports that Mg-rich smectites could hold more water. This clay rich unit appears to occur over a broad (~1000 x 1000 km) spatial extent in western Arabia Terra [*Dobrea et al.*, 2010]. And, as suggested by *Dobrea et al.* [2010] based on point location calculations of abundance, this clay-rich unit (which is often dust-

covered west of Mawrth Vallis) may be responsible for the increase in water-equivalent hydrogen in this area. Our observations of abundance with THEMIS across these clay-rich units support this hypothesis.

4.4. Geochemical assessment of the Mawrth Vallis stratigraphy

The origin of the Fe/Mg-phyllosilicate bearing and overlying Al-phyllosilicate bearing units in the Mawrth Vallis Noachian terrain remains fairly unconstrained. Both a sedimentary and/or volcanic origin for these deposits continue to remain possible with observed phases and morphologies via the deposition of fluvial and/or lacustrine sediments, or the deposition and subsequent alteration of mafic and/or felsic volcanic materials [*Loizeau et al.*, 2007; *Michalski and Noe Dobrea*, 2007; *Wray et al.*, 2008; *Noe Dobrea et al.*, 2010]. The draping Al-rich unit may have also formed in place and represent a zone of leaching and alteration [*Noe Dobrea et al.*, 2008; *Noe Dobrea et al.*, 2010]. While the THEMIS mapped clay-abundance alone cannot be used to distinguish between a sedimentary or volcanic origin, abundance maps can be used to help assess, if they are volcanic in origin, whether alteration occurred in place. To test this hypothesis, we assume a starting composition of an average of four derived chemistries for TES ST1 material from *Bandfield et al.* [2000], *Hamilton et al.* [2001], *Wyatt and McSween* [2002], and *McSween et al.* [2003]. We use the following major element oxides for the comparison: SiO_2, Al_2O_3, FeO, MgO, and CaO. Major element oxides derived from a representative mineral formula for each endmember present in Mawrth Vallis can be used to determine the bulk oxides for phyllosilicate-bearing material, by utilizing the volume percent abundances determined in this study. Comparing the major element oxides of both allow us to test whether alteration occurred in a closed system, where the bulk

composition of products detectable on the surface in Mawrth Vallis is equivalent to the starting average basalt composition. A ratio of the calculated bulk element oxides for Mawrth Vallis to the average TES-derived ST1 composition is shown in Figure B7. The relative enrichment in SiO_2 and depletion in FeO, MgO, and CaO are consistent with the transportation of mobilized elements through leaching. The relative enrichment in Al_2O_3 is also consistent with leaching, although the variability in TES-derived ST1 Al_2O_3 abundances renders interpretations from this phase alone indeterminate. The depletion in FeO and CaO may be attributed to hematite and bassanite (Ca-sulfate), respectively, as both minerals have been identified in the Mawrth Vallis region [*e.g.*, *Wray et al.*, 2008; *Wray et al.*, 2010]. Hematite has been observed in association with the Al-bearing phyllosilicates [*Wray et al.*, 2008], or at the contact between the Fe/Mg- and Al- bearing phyllosilicate units [*McKeown et al.*, 2009]. Bassanite has been observed on the Mawrth Vallis outflow channel floor, underlying the phyllosilicate-bearing units [*Wray et al.*, 2010]. These minerals are unaccounted for in the bulk composition calculation of Mawrth Vallis material as endmembers are limited during unmixing, and these phases are relatively minor. Although the phases may not be abundant in Mawrth Vallis, the concentration of FeO available from hematite and CaO from bassanite, respectively, may be enough to account for the depletion in the bulk composition calculation. The depletion in MgO, however, cannot be explained with the current spectroscopic observations of Mawrth Vallis mineralogy. This result indicates that alteration did not occur in a completely closed system in Mawrth Vallis and, as evidenced by hematite and bassanite, alteration minerals have experienced significant transportation from their

source. Regardless of the origin of these units, these widely abundant, phyllosilicate-rich rocks reflect a significant degree of alteration may have occurred in the past.

5.0 CONCLUSIONS

The results of this study indicate that discrepancies between OMEGA/CRISM observations of phyllosilicates and the at-detection-limit observations by TES could realistically be attributed to surface temperature discrepancies and/or intimate mixing of phyllosilicates at the surface, based on measured values at our example location. Due to limitations from a low spatial resolution for the TES instrument, and problems associated with non-linear mixing along the OMEGA/CRISM wavelength range, using THEMIS may be the most reliable approach to determining phyllosilicate modal abundance in well-characterized regions. Utilizing this approach in the Mawrth Vallis region, we have broadly mapped Fe/Mg-bearing phyllosilicates at 40-60% and Al-bearing phyllosilicates at 20-40%. These abundances are consistent with those calculated through non-linear mixing of OMEGA/CRISM data of several locations in this region. Because of the straightforward nature of determining mineral abundance in the thermal infrared, the full spatial distribution of clay abundance can be mapped with THEMIS. Results of this mapping and geochemical analyses are inconsistent with a clay formation model solely dependent upon a closed system of in-place alteration. This conclusion implies that if these deposits are volcanic in origin (rather than sedimentary) and clay formation occurred in-place, transportation of alteration products and/or leaching of chemical components occurred in an open system. The geochemical assessment performed here

does not preclude clay formation prior to deposition in a sedimentary and/or pyroclastic environment.

REFERENCES

Bandfield, J. L., V. E. Hamilton, P. R. Christensen (2000), A global view of Martian surface compositions from MGS-TES, *Science*, *287*, 1626-1630.

Bandfield, J. L. (2002), Global mineral distributions on Mars, *J. Geophys. Res.*, *107*(E6), doi:10.1029/2001JE001510.

Bandfield, J. L., and M. D. Smith (2003), Multiple emission angle surface–atmosphere separations of Thermal Emission Spectrometer data, *Icarus*, *161*, 47–65.

Bandfield, J. L., D. R. Rogers, M. D. Smith, and P. R. Christensen (2004a), Atmospheric correction and surface spectral unit mapping using Thermal Emission Imaging System data, *J. Geophys. Res.*, *109*, E10008, doi:10.1029/2004JE002289.

Bandfield, J. L., V. E. Hamilton, P. R. Christensen, and H. Y. McSween Jr. (2004b), Identification of quartzofeldspathic materials on Mars, *J. Geophys. Res.*, *109*, E10009, doi:10.1029/2004JE002290.

Bibring, J. P., et al. (2004), OMEGA: Observatoire pour la Minéralogie, l'Eau, les Glaces, et l'Activité, in *Mars Express: the scientific payload*, edited by A. Wilson, pp. 37-50, Eur. Space Agency, Noordwijk, Netherlands.

Bibring, J. P., et al. (2006), Global mineralogical and aqueous mars history derived from OMEGA/Mars express data, *Science*, *312*, 400-404, doi:10.1126/science.1122659.

Bish, D. and D. Vaniman (2008), What can clay mineralogy tell us about alteration environments on Mars?, Martian Phyllosilicates: Recorders of Aqueous Processes, Paris, France.

Bishop, J. L., E. Z. Noe Dobrea, N. K. McKeown, M. Parente, B. L. Ehlmann, J. R. Michalski, R. E. Milliken, F. Poulet, G. A. Swayze, J. F. Mustard, S. L. Murchie, and J. – P. Bibring (2008), Phyllosilicate diversity and past aqueous activity revealed at Mawrth Vallis, Mars, *Science*, *321*, 830-833, doi:10.1126/science.1159699.

Christensen, P. R., J. L. Bandfield, V. E. Hamilton, D. A. Howard, M. D. Lane, J. L. Piatek, S. W. Ruff, and W. L. Stefanov (2000a), A thermal emission spectral library of rock-forming minerals, *J. Geophys. Res.*, *105*(E4), 9735 – 9739,.

Christensen, P. R., et al. (2000b), Identification of a basaltic component on the Martian surface from Thermal Emission Spectrometer data, *J. Geophys. Res.*, *105*, 9609-9621, doi:10.1029/1999JE001127.

Christensen, P. R., et al. (2001), Mars Global Surveyor Thermal Emission Spectrometer experiment: Investigation description and surface science results, *J. Geophys. Res.*, *106*(E10), 23,823-23,872.

Christensen, P. R., et al. (2004), The THermal Emission Imaging System (THEMIS) for the Mars 2001 Odyssey mission, *Sp. Sci. Rev.*, *110*, 85-130.

Cooper, C.D., Mustard, J.F. (2002) Spectroscopy of loose and cemented sulfate-bearing soils: Implications for duricrust on Mars, *Icarus*, *158*, 42–55.

Edgett, K. S., and T. J. Parker (1997), Water on early Mars: Possible subaqueous sedimentary deposits covering ancient cratered terrain in western Arabia and Sinus Meridiani, *Geophys. Res. Lett.*, *24*(22), 2897 – 2900.

Edgett, K. S., and M. C. Malin (2002), Martian sedimentary rock stratigraphy: Outcrops and interbedded craters of northwest Sinus Meridiani an southwest Arabia Terra, *Geophys. Res. Lett.*, *29*(24), 2179, doi:10.10292002GL016515.

Ehlmann, B. L. et al. (2011a), CRISM-derived mineral abundances at the MSL landing sites, presented at *5th MSL Landing Site Workshop*, May 16, 2011.

Ehlmann, B. L. et al. (2011b), Estimating modal mineralogy of mixtures with phyllosilicates using radiative transfer modeling of visible/near infrared spectra, presented at *Lunar Planet. Sci. XLII*, Abstract 1704.

Feely, K.C., and Christensen, P.R. (1999) Quantitative compositional analysis using thermal emission spectroscopy: Application to igneous and metamorphic rocks. J. Geophys. Res. *104*(E10), 24195–24210.

Gillespie, A.R., Kahle, A.B., and Walker, R.E. (1986), Color enhancement of highly correlated images. I. Decorrelation and HSI contrast stretches. *Remote Sens. Environ.*, *20*, 209–235.

Hamilton, V. E., and P. R. Christensen (2000), Determining the modal mineralogy of mafic and ultramafic igneous rocks using thermal emission spectroscopy, *J. Geophys. Res.*, *105*(E4), 9717 – 9733.

Hamilton, V. E., M. B. Wyatt, H. Y. McSween, and P. R. Christensen (2001), Analysis of terrestrial and Martian volcanic compositions using thermal emission spectroscopy. 2. Application to Martian surface spectra from the Mars Global Surveyor Thermal Emission Spectrometer, *J. Geophys. Res.*, *106*(7), 14,733-14,746.

Hamilton, V. E., and P. R. Christensen (2005), Evidence for extensive, olivine-rich bedrock on Mars, *Geology*, *33*(6), 433-436.

Hapke, B. (1981), "Bidirectional reflectance spectroscopy 1. Theory," *J. Geophys. Res.*, *86*, 3039-3054.

Howard, A. D., and J. H. Moore (2007), The light-toned sediments in and near lower Mawrth Vallis may be a drape deposit, *Lunar Planet. Sci.*, XXXVIII, Abstract 1339.

Koeppen, W. C., and V. E. Hamilton (2005), Discrimination of glass and phyllosilicate minerals in thermal infrared data, *J. Geophys. Res.*, *110*, E08006, doi:10.1029/2005JE002474.

Langevin, Y., S. Douté, M. Vincendon, F. Poulet, J. –P. Bibring, B. Gondet, B. Schmitt, and F. Forget (2006), No signature of clear CO2 ice from the 'cryptic' regions in Mars' south seasonal polar cap, *Nature*, *447*, 790-792, doi:10.1038/nature05012.

Loizeau, D., N. Mangold, F. Poulet, J. –P. Bibring, A. Gendrin, V. Ansan, C. Gomez, B. Gondet, Y. Langevin, P. Masson, and G. Neukum (2007), Phyllosilicates in the Mawrth Vallis region of Mars, *J. Geophys. Res.*, *112*, E08S08, doi:10.1029/2006JE002877.

Malin, M. C., and K. S. Edgett (2000), Sedimentary rocks of early Mars, *Science*, *290*(5498), 1927-1937.

McKeown, N. K., *et al.* (2008), Characterization of phyllosilicates observed in the central Mawrth Vallis region, Mars, their potential formation processes, and implications for past climate, *J. Geophys. Res.*, *114*, E00D10.

McSween, H. Y. *et al.* (2003), Constraints on the composition and petrogenesis of the Martian crust, *J. Geophys. Res.*, *108*, 5135-5153.

Michalski, J. R., S. W. Ruff, and P. R. Christensen (2006a), TES and THEMIS analysis of Martian clay-bearing deposits discovered by Mars Express OMEGA, paper presented at *Lunar Planet. Sci. XXXVII*, Abstract 1242.

Michalski, J. R., M. D. Kraft, T. G. Sharp, L. B. Williams, and P. R. Christensen (2006), Emission spectroscopy of clay minerals and evidence for poorly crystalline aluminosilicates on Mars from Thermal Emission Spectrometer data, *J. Geophys. Res.*, *111*, E03004, doi:10.1029/2005JE002438.

Michalski, J. R., and E. Z. Noe Dobrea (2007), Evidence for a sedimentary origin of clay minerals in the Mawrth Vallis region, Mars, *Geology*, *35*(10), 951 – 954, doi:10.1130/G23854A.

Michalski, J. R. and R. L. Fergason (2009), Composition and thermal inertia of the Mawrth Vallis region of Mars from TES and THEMIS data, *Icarus*, *199*, 25-48.

Milam, K. A., H. Y. McSween Jr., J. Moersch, and P. R. Christensen (2010), Distribution and variation of plagioclase compositions on Mars, *J. Geophys. Res.*, *115*, E09004, doi:10.1029/2009JE003495.

Milliken, R. E., and J. F. Mustard (2005), Quantifying absolute water content of minerals using near-infrared reflectance spectroscopy, J. Geophys. Res., 110, E12001, doi:10.1029/2005JE002534.

Milliken, R. E., Bristow, T., Bish, D. L., and Mustard, J.F. (2010), The case for mixed-layered clays on Mars, 41st Lunar and Planetary Science Conference, CD #2030.

Moersch, J. E., and P. R. Christensen (1995), Thermal emission from particulate surfaces: A comparison of scattering models with measured spectra, *J. Geophys.. Res.*, *100*, E4, 7465-7477.

Murchie, S. L., et al. (2007a), Compact Reconnaissance Imaging Spectrometer for Mars (CRISM) on Mars Reconnaissance Orbiter (MRO), *J. Geophys. Res.*, *112*, E05S03, doi:10.1029/2006JE002682.

Murchie, S. L., E. Guinness, and S. Slavney (2007b), CRISM data product software interface specification, ftp://pds-geosciences.wustl.edu/mro-crism/mro-m-crism-2-edr-v1/mrocr_0001/document/crism_dpsis.pdf, *NASA Planet. Data Syst.*, Greenbelt, Md., 17 Aug.

Mustard, J. F., et al. (2008), Hydrated silicate minerals on Mars observed by the Mars Reconnaissance Orbiter CRISM instrument, *Nature*, *454*, 305-309, doi:10.1038/nature07097.

Noe Dobrea, E. Z., et al. (2008), Clay bearing units in the region around Mawrth Vallis: Stratigraphy, extent, and possible alteration fronts, *Lunar Planet. Sci.*, XXXIX, Abstract 1077.

Noe Dobrea, E. Z., et al. (2010), Mineralogy and stratigraphy of phyllosilicate-bearing and dark mantling units in the greater Mawrth Vallis/west Arabia Terra area: Constraints on geological origin, *J. Geophys. Res., 115*, E00D19, doi:10.1029/2009JE003351.

Parente, M. (2008), A new approach to denoising CRISM images, paper presented at Lunar Planet. Sci., XXXIX, Abstract 2528.

Pelkey, S. M. et al. (2007), CRISM multispectral summary products: Parameterizing mineral diversity on Mars from reflectance, *J. Geophys. Res.*, *112*, E08S14, doi:10.1029/2006JE002831.

Poulet, F., J. –P. Bibring, J. F. Mustard, A. Gendrin, N. Mangold, Y. Langevin, R. E. Arvidson, B. Gondet, C. Gomez, and the Omega Team (2005), Phyllosilicates on Mars and implications for early martian climate, *Nature*, *438*, 623-627, doi:10.1038/nature04274.

Poulet, F., N. Mangold, D. Loizeau, J. –P. Bibring, Y. Langevin, J. Michalski, and B. Gondet (2008), Abundance of minerals in the phyllosilicate-rich units on Mars, *Astron. Astrophys.*, *487*, L41-L44, doi:10.1051/0004-6361:200810150.

Poulet, F., and J. Carter (2011) Mineral abundances of the phyllosilicate-bearing deposits of the four candidate MSL landing sites, presented at *5th MSL Landing Site Workshop*, May 16, 2011.

Ramsey, M. S., and P. R. Christensen (1998), Mineral abundance determination: Quantitative deconvolution of thermal emission spectra, *J. Geophys. Res., 103*(B1), 577 – 596.

Rogers, A. D., P. R. Christensen, and J. L. Bandfield (2005), Compositional heterogeneity of the ancient Martian crust: Analysis of Ares Vallis bedrock with THEMIS and TES data, *J. Geophys. Res.*, *110*, E05010.

Rogers, A. D., and J. L. Bandfield (2009), Mineralogical characterization of Mars Science Laboratory candidate landing sites from THEMIS and TES data, *Icarus*, *203*, 437-453.

Ruff, S. W., and P. R. Christensen (2007), Basaltic andesite, altered basalt, and a TES-based search for smectite clay minerals on Mars, *Geophys. Res. Lett.*, *34*, L10204, doi:10.1029/2007GL029602.

Salisbury, J. W., L. S. Walter, N. Vergo, and D. M. D'Aria (1991), Infrared (2.1–25 μm) *Spectra of Minerals*, 267 pp., Johns Hopkins Univ. Press, Baltimore, MD.

Scott, D. H., and Tanaka, K. L. (1986) Geologic map of the Western Equatorial Region of Mars: U.S. Geological Survey Geologic Investigations Series Map I-1802-A, 1 sheet, scale 1:15,000,000.

Shkuratov, Y., Starukhina, L., Hoffmann, H., and Arnold, G. (1999) A model of spectral albedo of particulate surfaces: Implications for optical properties of the Moon, *Icarus*, *137*, 235–246.

Thomson, J. L., and J. W. Salisbury (1993), The mid-infrared reflectance of mineral mixtures (7 – 14 mm), *Remote Sens. Environ.*, *45*, 1-13.

Velde, B., Righi, D., Meunier, A., Hillier, S., and A. Inoue (1995) Composition and mineralogy of clay minerals, in *Origin and mineralogy of clays: clays and the environment*, edited by B. Velde, pp. 8-42, Springer, Berlin.

Vincent, R.K., and Hunt, G.R.(1968) Infrared reflectance from mat surfaces, *Appl. Optics*, *7*(1), 53–59.

Viviano, C. E. and J. E. Moersch (submitted), Mapping Fe/Mg-rich phyllosilicates on Mars using THEMIS multispectral thermal infrared images, *J. Geophys. Res*.

Wray, J.J., Ehlmann, B.L., Squyres, S.W., Mustard, J.F., and Kirk, R.L., 2008, Compositional stratigraphy of clay-bearing layered deposits at Mawrth Vallis, Mars, *Geophys. Res. Lett.*, *35*, L12202, doi: 10.1029/2008GL034385.

Wyatt, M. B., V. E. Hamilton, H. Y. McSween, P. R. Christensen, and L. A. Taylor (2001), Analysis of terrestrial and martian volcanic compositions using thermal emission spectroscopy: 1. Determination of mineralogy, chemistry, and classification strategies, *J. Geophys. Res.*, *106*(E7), 14,711-14,732.

Wyatt, M. B., and H. Y. McSween (2002) Spectral evidence for weathered basalt as an alternative to andesite in the northern lowlands of Mars, *Nature*, *417*, 263-266.

Appendix B

Table B1. TES spectral unmixing results of light-toned material, from *Michalski and Fergason*, 2009.

Mineral group	Minus Feld	Minus Pyx	Minus Silica	Minus Clay	Minus Zeo	Minus Other
Feldspar	-	12	27	16	17	-
Pyroxene	0	-	14	9	13	-
Silica-rich	35	35	-	34	40	-
Clay	20	18	13	-	15	-
Zeolite	21	14	27	24	-	-
Other	24	21	19	17	15	-
Total	100	100	100	100	100	-
RMS	0.215	0.200	0.287	0.200	0.209	-
MPE	-	-	-	-	-	-

Table B2. THEMIS spectral unmixing results of light-toned material, scene I01199005.

Mineral	Minus Feld	Minus Pyx	Minus Silica	Minus Clay	Minus Zeo	Minus Other
			Unmixing with Clay=nontronite			
Labradorite	-	11.23	8.14	12.59	8.59	10.51
Augite	8.11	-	4.77	6.40	6.75	15.37
Felsic Glass	10.07	7.73	-	12.93	12.88	4.00
Nontronite	19.32	14.57	21.35	-	12.74	41.69
Heulandite	12.32	11.33	21.70	5.88	-	28.41
Dust	50.15	55.13	44.04	62.18	59.04	-
Total	100	100	100	100	100	100
RMS	0.00304	0.00330	0.00277	0.00296	0.00152	0.00425
MPE	0.00268	0.00287	0.00235	0.00257	0.00222	000355
			Unmixing with Clay=montmorillonite			
Labradorite	-	41.69	13.06	12.59	12.44	34.09
Augite	12.35	-	5.48	6.40	6.78	15.67
Felsic Glass	15.36	15.37	-	12.94	8.00	2.43
Montmorillonite	6.99	10.51	17.54	-	12.34	16.35
Heulandite	4.77	4.00	9.06	5.88	-	31.45
Dust	60.51	28.41	54.85	62.18	60.42	-
Total	100	100	100	100	100	100
RMS	0.00348	0.00226	0.00278	0.00296	0.00280	0.00499
MPE	0.00300	0.00287	0.00236	0.00257	0.00240	0.00401

Table B3. THEMIS spectral unmixing results of light-toned material, scene I01561006.

Mineral	Minus Feld	Minus Pyx	Minus Silica	Minus Clay	Minus Zeo	Minus Other
			Unmixing with Clay=nontronite			
Labradorite	-	26.41	23.22	27.98	27.35	27.7
Augite	6.41	-	1.17	4.77	7.26	6.38
Felsic Glass	18.55	21.61	-	27.09	40.36	28.57
Nontronite	19.81	6.48	13.06	-	3.14	8.45
Heulandite	45.52	25.42	57.63	24.30	-	28.89
Dust	9.70	20.07	4.90	15.85	21.89	-
Total	100	100	100	100	100	100
RMS	0.00393	0.00325	0.00365	0.00281	0.00289	0.00290
MPE	0.00350	0.00281	0.00305	0.00242	0.00249	0.00248
			Unmixing with Clay=montmorillonite			
Labradorite	-	31.07	28.42	27.98	28.21	31.10
Augite	17.24	-	2.05	4.77	7.29	6.65
Felsic Glass	48.96	18.23	-	27.09	37.84	26.06
Montmorillonite	4.10	11.08	25.62	-	4.86	8.90
Heulandite	9.72	21.54	35.40	24.30	-	27.25
Dust	19.95	18.07	8.51	15.85	21.80	-
Total	100	100	100	100	100	100
RMS	0.00379	0.00305	0.00322	0.00281	0.00291	0.00297
MPE	0.00334	0.00263	0.00269	0.00242	0.00251	0.00248

Table B4. THEMIS spectral unmixing results of light-toned material, scene I19047008.

Mineral	Minus Feld	Minus Pyx	Minus Silica	Minus Clay	Minus Zeo	Minus Other
			Unmixing with Clay=nontronite			
Labradorite	-	28.18	23.26	29.62	24.06	27.95
Augite	8.15	-	3.27	4.36	5.06	8.63
Felsic Glass	6.02	9.68	-	13.02	13.18	3.57
Nontronite	39.25	8.99	23.43	-	12.94	34.18
Heulandite	24.58	7.25	23.25	5.02	-	25.67
Dust	21.99	45.91	26.78	47.98	44.76	-
Total	100	100	100	100	100	100
RMS	0.00464	0.00369	0.00321	0.00346	0.00294	0.00408
MPE	0.00431	0.00327	0.00269	0.00304	0.00250	0.00336
			Unmixing with Clay=montmorillonite			
Labradorite	-	33.34	31.07	29.62	29.62	51.77
Augite	19.58	-	3.59	4.36	4.63	8.96
Felsic Glass	29.09	8.14	-	13.02	9.00	1.88
Montmorillonite	1.03	5.29	17.01	-	9.99	14.87
Heulandite	1.46	5.92	9.17	5.02	-	22.51
Dust	48.84	47.30	39.16	47.98	46.76	-
Total	100	100	100	100	100	100
RMS	0.00590	0.00376	0.00334	0.00346	0.00333	0.00508
MPE	0.00511	0.00333	0.00286	0.00304	0.00287	0.00402

Table B5. THEMIS spectral unmixing results of light-toned material, scene I39449009.

Mineral	Minus Feld	Minus Pyx	Minus Silica	Minus Clay	Minus Zeo	Minus Other
			Unmixing with Clay=nontronite			
Labradorite	-	26.42	22.01	28.56	25.80	26.25
Augite	4.55	-	1.32	3.27	4.66	4.42
Felsic Glass	14.64	21.71	-	24.22	32.49	18.97
Nontronite	26.61	6.79	18.79	-	7.25	17.01
Heulandite	39.64	17.44	49.42	18.51	-	33.33
Dust	14.54	27.63	8.44	25.46	29.78	-
Total	100	100	100	100	100	100
RMS	0.00425	0.00349	0.00386	0.00323	0.00320	0.00340
MPE	0.00380	0.00303	0.00326	0.00280	0.00274	0.00284
			Unmixing with Clay=montmorillonite			
Labradorite	-	30.95	28.99	28.56	28.59	35.28
Augite	14.81	-	1.91	3.27	4.59	4.53
Felsic Glass	42.46	19.36	-	24.22	28.59	15.53
Montmorillonite	3.53	7.93	26.21	-	7.99	15.46
Heulandite	9.05	15.02	27.53	18.51	-	29.19
Dust	30.13	26.72	15.34	25.46	30.16	-
Total	100	100	100	100	100	100
RMS	0.00443	0.00338	0.00349	0.00323	0.00331	0.00359
MPE	0.00384	0.00293	0.00296	0.00280	0.00283	0.00296

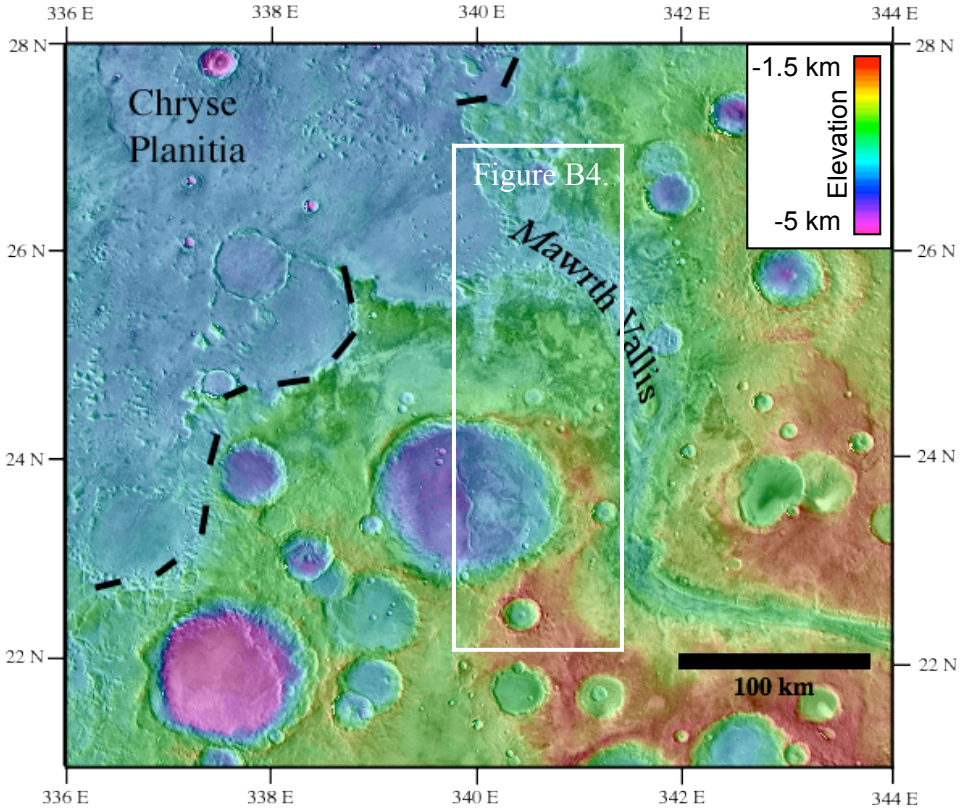

Figure B1. Geologic context map of the Mawrth Vallis region. The Mawrth Vallis channel terminates at the dichotomy boundary (indicated by black hashed lines) between the cratered highlands and northern lowlands at Chryse Planitia. Topography (color scale) is overlain on THEMIS daytime infrared imagery. White box indicates location of Figure B4.

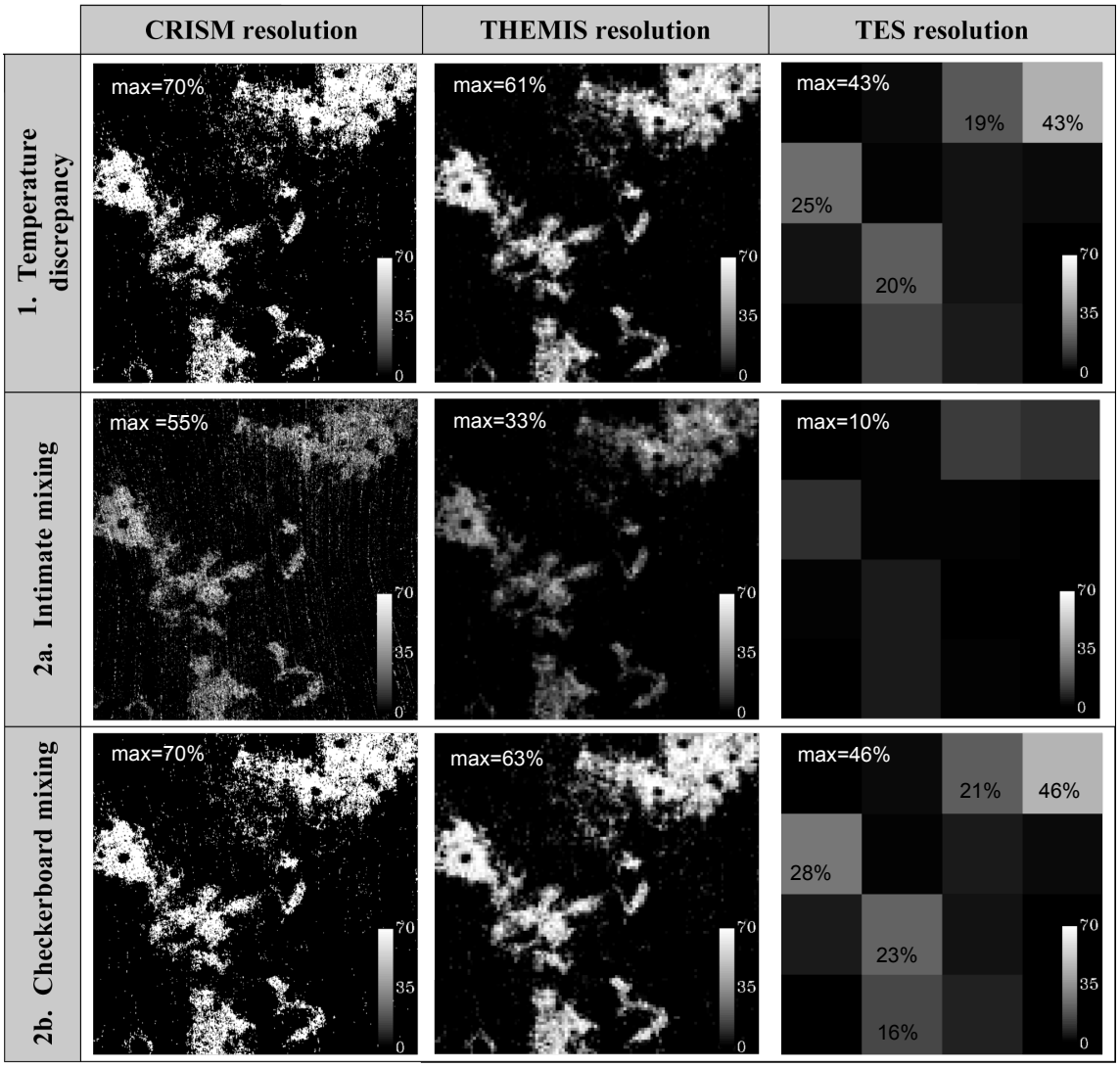

Figure B2. Modeling of *Hypotheses 1*, *2a*, and *2b* using an example CRISM FRT mapped distribution of clays in Mawrth Vallis. See section 2.1 for a complete description of each model. Abundances at CRISM, THEMIS, and TES resolution are indicated by grayscale and all images display identical contrast stretching (from 0 to 70%). Maximum clay abundance measured in each model is reported in upper left corner of each image. TES pixels with modeled clay abundance greater than the limit of detection reported in black. (*1*, left): 70% nontronite, 30% ST1 at 248 K (white), 100% ST1 at 256 K (black), (*1*, center): THEMIS resolution and measured nontronite abundance, (*1*, right): TES resolution and measured nontronite abundance. (*2a*, left): Grayscale range of nontronite abundance for intimate mixture modeling (see section 2.1), (*2a*, center): THEMIS resolution and measured nontronite abundance, (*2a*, right): TES resolution and measured nontronite abundance. (*2b*, left): 70% nontronite, 30% ST1 (white), 100% ST1 (black), (*2b*, center): THEMIS resolution and measured nontronite abundance, (*2b*, right): TES resolution and measured nontronite abundance.

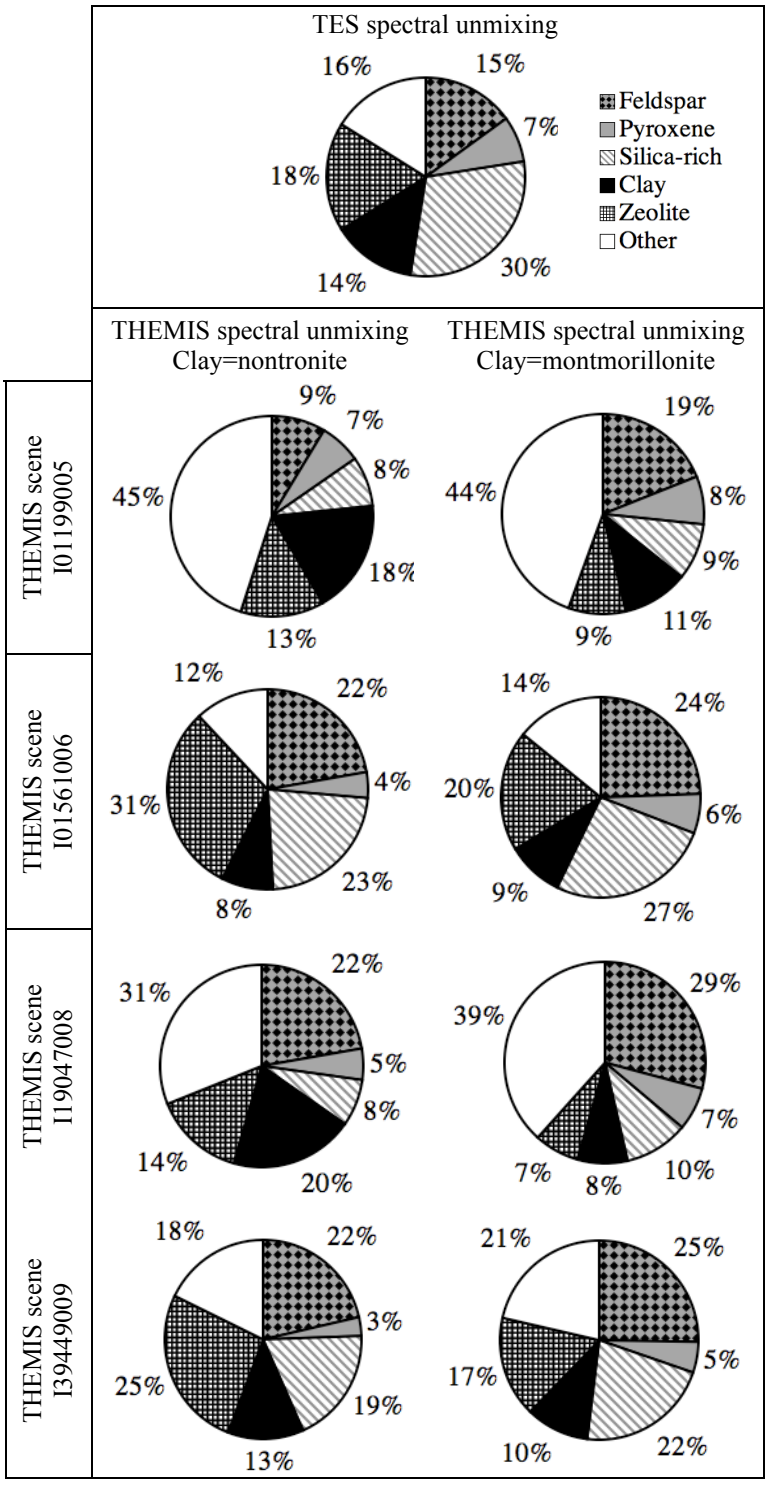

Figure B3. Pie charts of mineral proportions inferred from linear unmixing of TES spectra [*Michalski and Fergason,* 2009] and averaged THEMIS unmixing iterations for four THEMIS scenes (this study). Left column charts for THEMIS scenes indicate unmixing results using nontronite as the clay endmember; right column indicates montmorillonite. See section 2.2 for abundance calculation description.

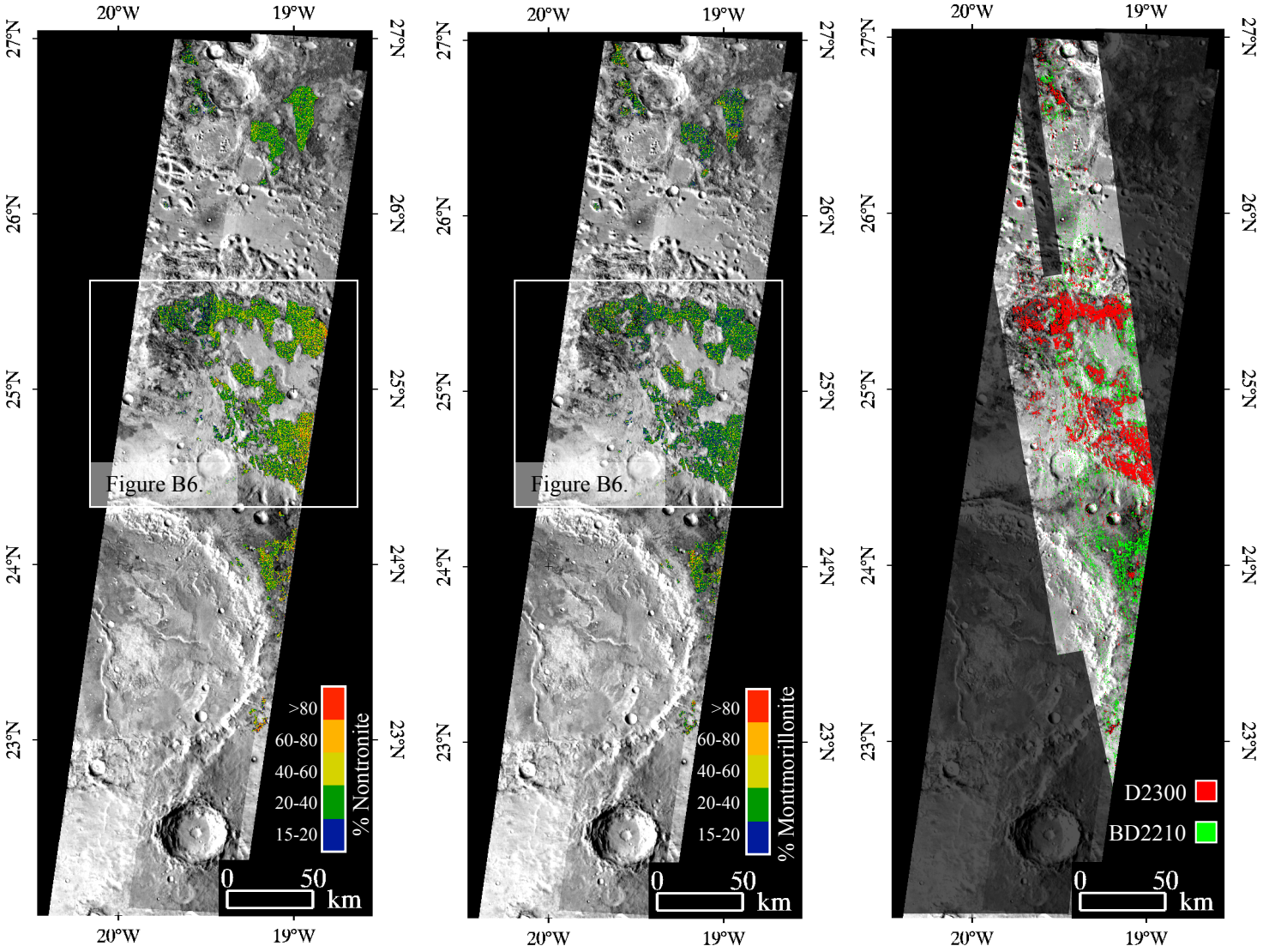
20°W
19°W
27°N
26°N
25°N
24°N
23°N
Figure B6.
>80
60-80
40-60
20-40
15-20
% Nontronite
0
50
km
% Montmorillonite
D2300
BD2210

Figure B4. THEMIS linear unmixing results of clay component in light-toned phyllosilicate-bearing materials in Mawrth Vallis as compared to CRISM MSP mapping results. Mapping is overlain on THEMIS brightness temperature image. White boxes indicate location of Figure B6. (left) nontronite abundance, (middle) montmorillonite abundance, (right) MSP mapping of Fe/Mg-rich clay index (D2300) in red and Al-rich clay index (BD2210) in green; indices described in *Pelkey et al.*, [2007]. Darkened areas lack MSP coverage.

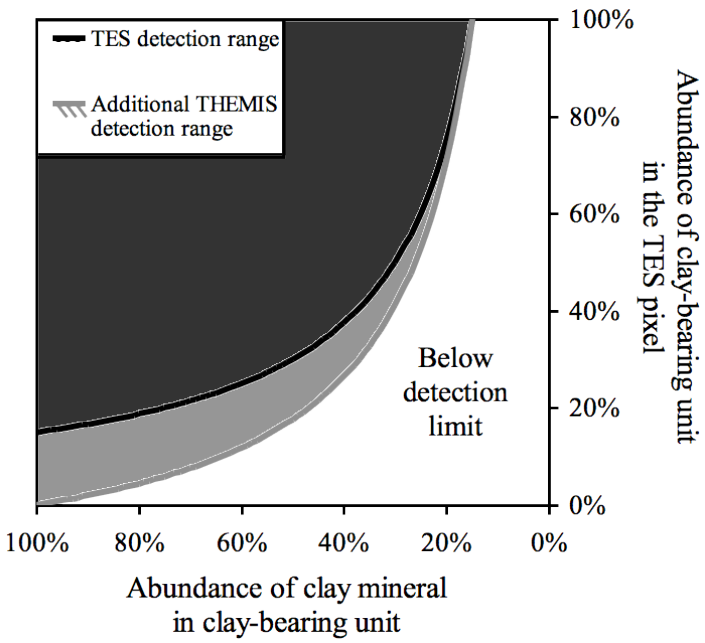

Figure B5. Dependency of clay detectability with TES and THEMIS on the percentage of that clay-bearing unit within a TES pixel as compared to the actual abundance of clays within that unit; modified from [*Michalksi and Fergason*, 2009]. Detectability with TES instrument indicated by dark fill; additional detectability added by THEMIS resolution at this scale is shown with hashed lines.

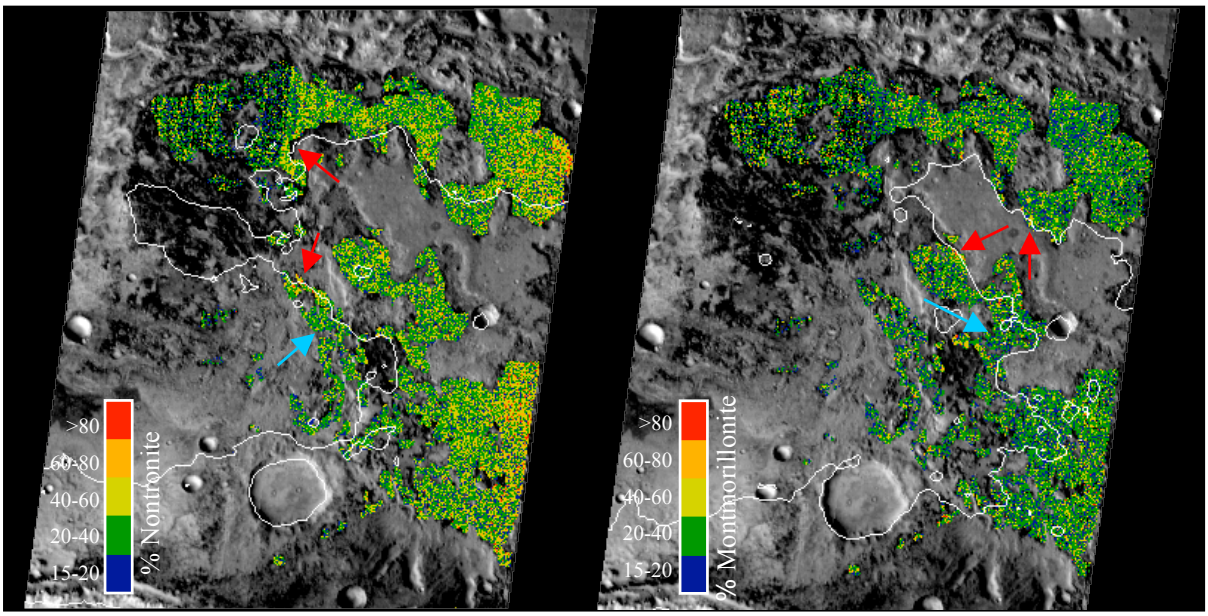

Figure B6. THEMIS linear unmixing results of clay component in light-toned phyllosilicate-bearing materials in Mawrth Vallis; location outlined in Figure B4. (left) nontronite abundance with overlain contour interval in white at -3350m, (right) montmorillonite abundance with overlain contour interval in white at -2960m. Section 4.3 describes significance of colored arrows.

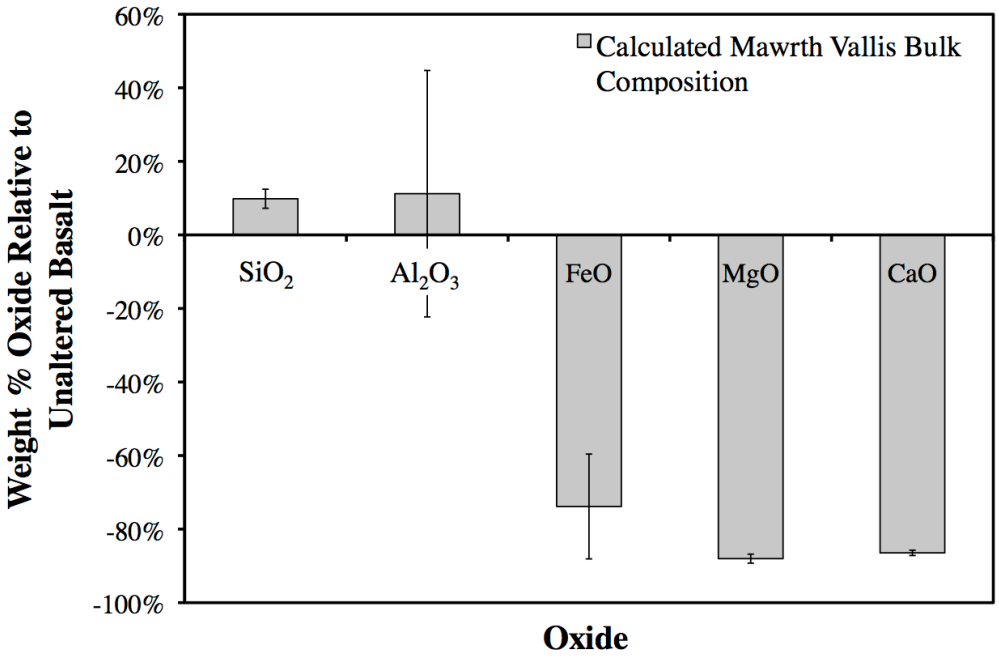

Figure B7. Calculated bulk composition of weight percent oxides for Mawrth Vallis relative to weight percent oxides for four derived TES ST1 compositions (see section 4.4). Error bars indicate the standard deviation for this measurement based on the four TES compositions. The bulk Mawrth Vallis composition was determined by endmember abundances presented in this study.

Part 4
Evidence for the Carbonation of Serpentine in Nili Fossae, Mars: Implications for Hydrothermal Processes

ABSTRACT

The identification of serpentine [*Ehlmann et al.*, 2010] and magnesium carbonate [*Ehlmann et al.*, 2008] in the easternmost portions of the Nili Fossae region of Mars indicates hydrothermal alteration of an olivine-rich protolith. Here we characterize Fe/Mg phyllosilicates associated with these units and present spectral evidence for the presence of a talc component, distinguishable from saponite. Locations with magnesium carbonate are exclusively associated with talc-related phyllosilicates. The westernmost portion of the Nili Fossae region, where a mafic protolith dominates, is associated with Fe/Mg phyllosilicates that alternatively display spectral evidence for a wide degree of chloritization. We suggest that Noachian Fe/Mg smectites were uniformly buried in the easternmost portion of the Nili Fossae region, and were subsequently overlain by Hesperian lava flows that initiated the hydrothermal alteration. This alteration resulted in serpentization of olivine followed by carbonation of serpentine, providing an explanation for the limited occurrence of serpentine and the co-location of carbonate and talc-bearing material throughout this area. If this carbonation reaction was a widespread phenomenon, it may have been an important process in the ancient Martian carbon cycle and could have provided a sink for CO_2 in the past.

1.0 INTRODUCTION

Reports of an increasingly diverse suite of alteration minerals on Mars can be attributed to the improved coverage provided by high spatial and spectral resolution orbital spectroscopy. Initial interpretations of data from the Observatoire pour la Minéralogie, l'Eau, les Glaces, et l'Activité (OMEGA) experiment on Mars Express, and the Compact Reconnaissance Imaging Spectrometer for Mars (CRISM) experiment on the Mars Reconnaissance Orbiter suggest Mars experienced neutral to alkaline conditions with significant water-rock interactions during the Noachian, allowing for the production of Fe/Mg-rich smectites [*e.g. Bibring et al.*, 2006]. Recently, alteration phases including Fe/Mg-phyllosilicates, zeolites, prehnite, chlorite, serpentine, illite (or muscovite), kaolinite, and hydrated silica have been identified in the Nili Fossae region, Tyrrhena Terra (south of Syrtis Major), and Noachis Terra (west of Hellas Basin) [*Mustard et al.*, 2008; *Ehlmann et al.*, 2009; *Fraeman et al.*, 2009; *Ehlmann et al.*, 2011]. These minerals, identified from high spatial and spectral resolution data provided by CRISM, are interpreted to be products of low-grade thermal metamorphism or hydrothermal interaction, along with diagenesis, suggesting that past aqueous alteration of the subsurface crust occurred at elevated temperatures [*Ehlmann et al.*, 2009; *Ehlmann et al.*, 2010].

The distinction between low-temperature sedimentary processes (weathering and diagenesis) that occur during and after lithification at the near-surface environment, and low-grade metamorphism is difficult, as some of the same minerals may be generated in both environments. This distinction is particularly difficult to make using orbital detection of these mineral phases, because evaluation of rock textures and identification

of the full mineral assemblage is impossible. Additionally, the temperature at which recrystallization or new mineral formation occurs is highly dependent upon the protolith. Thus, the regional context of metamorphism may be difficult to decipher. Despite these limitations, with the assumption of a basaltic protolith for Mars [*McSween et al.*, 2009], metamorphic assemblages can be used to constrain and identify particular pressure and temperature conditions and metamorphic facies [*McSween et al.*, 2011, *Ehlmann et al.*, 2011].

1.1 Previously identified metamorphic assemblages on Mars

Ehlmann et al. [2011] has identified several metamorphic mineral assemblages on Mars using CRISM spectra. It is worth noting that an "assemblage", as used in their work, refers to a collection of individual minerals identified in pixels that are in close proximity to each other, not necessarily all in the same CRISM pixel, and is by necessity an incomplete tally of co-exiting minerals. This nontraditional definition of an assemblage is justified because visible and near-infrared spectra of minerals do not combine linearly, making minor and/or spectrally non-dominant minerals hard to identify in compositionally mixed pixels. The assemblages identified by *Ehlmann et al.* [2011], typically associated with host craters, are: (*Assemblage 1*) prehnite-chlorite-silica, (*Assemblage 2*) analcime-silica-Fe/Mg smectite-chlorite, and (*Assemblage 3*) chlorite-illite(muscovite). Additionally, (*Assemblage 4*) serpentine has been found both associated with craters and in bedrock units. The distribution of these assemblages occurs in the Nili Fossae region, Tyrrhena Terra, and Noachis Terra. The distribution of alteration minerals in the Nili Fossae region identified by *Ehlmann et al.* [2009], as well as phases identified in this study, are shown in Figure C1.

1.1.1. Prehnite-chlorite-silica and analcime-silica-Fe/Mg smectite-chlorite assemblages

Prehnite-bearing rocks (*Assemblage 1*) are of particular interest; prehnite forms in hydrothermal or metamorphic environments [*e.g.*, *Frey and Robinson*, 1999] and has a unique OH overtone absorption feature at 1.48 μm [*Clark et al.*, 2007], allowing for its discrimination from chlorite, which shares a ~2.35-2.36-μm absorption feature. The stability of prehnite (along with pumpellyite) defines the onset of sub-greenschist facies metamorphism, which typically occurs between 300-400º C [*e.g.*, *Schiffman and Day*, 1999]. Although it is spectrally similar to Mg-rich chlorite, radiative transfer modeling by Poulet *et al.* [2008] suggests pumpellyite may also be present. Analcime-bearing rocks (*Assemblage 2*) indicate the onset of zeolite facies metamorphism [*Arkai et al.*, 2003], though the presence of the silica phase in this assemblage is not indicative of a particular environment, as it forms in a variety of conditions [*McLennan*, 2003]. Analcime shares diagnostic absorption features (at 1.42, 1.91, and 2.52 μm) with other zeolites as well as a unique, weaker feature at 1.79 μm. *Ehlmann et al.* [2011] suggest the most probable formation mechanism for *Assemblages 1* and *2* is the interaction of hydrothermal (<400º C) fluids with a basaltic protolith.

1.1.2. Chlorite-illite assemblage

Chlorite and illite (*Assemblage 3*) are typically products of hydrothermal activity or low-grade metamorphism on Earth. During burial diagenesis, dioctahedral smectite can ultimately convert to illite, and trioctohedral smectite converts to chlorite. Mixed-layered clays, such as illite/smectite (I/S) or smectite/chlorite (S/C), have phyllosilicate layers that are mixed at the mineral structural level. The proportion of different

phyllosilicate layers in these mixed-layered clays changes with burial depth, and thus is a useful parameter for characterizing the environment of formation. Chloritization (the conversion of smectite to chlorite) appears to be a much more common process on Mars than on Earth, where illitization dominates (the conversion of smectite to illite) [*Milliken et al.*, 2010]. This is consistent with the low abundance of K+ on Mars required for illitization [*ibid.*]. On Earth, the conversion of smectite to chlorite typically begins with the formation of saponite (Mg-rich smectite) at the expense of volcanic minerals. Then, as diagenesis or hydrothermal alteration proceeds, saponite transforms to corrensite (S/C) [*e.g.*, *Reynolds*, 1988]. In geothermal environments, the transformation of smectite to chlorite proceeds through three identified pathways: (1) a continuous mixed-layer smectite/chlorite series, (2) a discontinuous smectite-corrensite-chlorite series, and (3) a direct transition from smectite to chlorite. These reaction pathways are kinetically controlled and depend on fluid/rock ratios and fluid transport mechanisms, where pathway 1 occurs in response to incomplete reactions due to low fluid/rock ratios and pathway 3 occurs with high fluid/rock ratios promoting the dissolution/nucleation/growth necessary for chloritization [*e.g.*, Robinson *et al.*, 2002].

Milliken et al. [2010, 2011] have derived two spectral parameters for the identification and characterization of S/C mixed-layered clays. The first parameter, referred to by *Milliken et al.* [2010, 2011] as "absorption angle" (here shortened to AA), quantifies the angle defined by two separate continuum lines, one from approximately 2.2 to 2.36 μm, and the other from 2.36 to 2.42 μm. This angle becomes smaller as the proportion of chlorite interlayers increases. The second parameter is a ratio of the band depth at 2.34 μm (associated with chlorite) to the band depth at 2.295 μm (associated

with smectite). *Milliken et al.* [2010, 2011] used laboratory spectra of smectite, chlorite, and S/C mixed-layered clays to define several zones of chloritization based on the 2.34-μm/2.295-μm band depth ratio which delineate unaltered and heated smectites, mix-layered clays, and chlorites. A plot of the two spectral parameters described above for a suite of clay samples [*Bristow et al.*, 2009] spanning the range of chloritization (S→S/C→C) shows an inverse correlation through the mixed-layered zone. *Milliken et al.* [2011] have used these parameters to identify mix-layered clays in the ancient crust of Mars, including regions such as Nili Fossae, as well as unaltered smectites in locations such as Mawrth Vallis.

1.1.3 Serpentine assemblage

The serpentine-bearing rocks (*Assemblage 4*) in the Nili Fossae region are indicative of hydrothermal alteration of olivine-rich rocks. *Ehlmann et al.* [2009] identified serpentine-bearing rocks in association with an olivine-rich draping unit overlying Mg-smectite, a stratigraphic relationship found throughout Nili Fossae [*Mangold et al.*, 2007]. The spectral signature of magnesium carbonate, first identified by *Ehlmann et al.* [2008], is also associated with the underlying Mg-smectite and has been hypothesized to be a weathering product of either the olivine or serpentine in this region [*Ehlmann et al.*, 2009, 2010; *Brown et al.*, 2010]. *Ehlmann et al.* [2008] suggested a potential formation mechanism for the carbonate-bearing unit was that impact or volcanic heating of the olivine-bearing material led to hydrothermal alteration along the contact with the underlying water-bearing Mg-smectite unit. *Brown et al.* [2010] proposed a different spectral interpretation, suggesting that the Mg-smectite phase could actually be talc based on their assertion that the two phases are spectrally

indistinguishable. The consequence of this new spectral interpretation was a modified hydrothermal hypothesis, in which the phyllosilicate was formed at the same time as the overlying carbonate-bearing unit by a single hydrothermal event [*Brown et al.*, 2010]. If correct, this hypothesis suggests that stratigraphic relation of the phyllosilicate and carbonate-bearing units are simply the result of different temperatures regimes within the zone of hydrothermal alteration [*Brown et al.*, 2010]. The abundant and compositionally varying olivine in the Nili Fossae region [*Hoefen et al.*, 2003; *Mustard et al.*, 2005; *Hamilton and Christensen*, 2005; *Koeppen and Hamilton*, 2008] particularly dominates in the northeast portion of the area shown in Figure C1. The predominance of this mineral suggests an olivine-rich protolith is appropriate for this region of Nili Fossae.

The following two-step reaction series describes the process of serpentine and talc/carbonate formation via the hydrothermal alteration of an Mg-rich protolith [*e.g., Brown et al.*, 2010]:

Step 1: Serpentization

$$3Mg_2SiO_4 + SiO_2 + 4H_2O \Rightarrow 2Mg_3Si_2O_5(OH)_4 \quad \text{(Eq. 1)}$$

(*forsterite* + *aqueous silica* + *water* ⇒ *serpentine*)

Alt. Step 1a: Serpentization

$$18Mg_2SiO_4 + 6Fe_2SiO_4 + CO_2 + 26H_2O \Rightarrow 12Mg_3Si_2O_5(OH)_4 + 4Fe_3O_4 + CH_4 \quad \text{(Eq. 1a)}$$

(*forsterite* + *fayalite* + *carbon dioxide* + *water* ⇒ *serpentine* + *magnetite* + *methane*)

Step 2: Carbonation

$$2Mg_3Si_2O_5(OH)_4 + 3CO_2 \Rightarrow Mg_3Si_4O_{10}(OH)_2 + 3H_2O + 3MgCO_3 \quad \text{(Eq. 2)}$$

(*serpentine* + *carbon dioxide* ⇒ *talc* + *water* + *magnesite*)

Step 1 requires the presence of aqueous silica available in significant amounts, dissolved from mafic rocks as predicted by *McLennan* [2003]. The 'alternate' step 1 results in significant magnetite production; however, magnetite has no distinguishing absorption features visible and near-infrared wavelength ranges and therefore is undetectable using these techniques. Equation 2 also provides a condition where methane may be produced in the presence of CO_2; *Brown et al.* [2010] and *Ehlmann et al.* [2010] suggested serpentization may be one potential source of telescopic observations of methane [*Mumma et al.*, 2009] that have been contested [*Zahnle et al.*, 2010]. If this region was the source of methane on Mars, it would require currently active serpentization in the subsurface [*Brown et al.*, 2010]. *Brown et al.* [2010] argue that if the Nili Fossae carbonates observed were formed under hydrothermal conditions, the presence of large oceans or a warmer atmospheric environment in Noachian Mars would not be required. Serpentine is known to be very reactive in the presence of CO_2 and carbonation of serpentinite may represent a significant but neglected sink in Earth's global carbon cycle [*Klein and Garrido*, 2011]. Thus, the identification of talc as the phyllosilicate-bearing unit in the Nili Fossae region would be potentially relevant to our understanding of the formation mechanisms for carbonates on Mars and potential atmospheric sources and sinks for the Martian atmospheric CO_2.

1.4. Near-infrared identification of Fe/Mg smectites from orbit

In the visible and near-infrared wavelength region (λ = 0.3-5.0 μm), phyllosilicate minerals have absorption features (~1.4 and 1.9 μm) due to water that is loosely bound in their structures and the cation-hydroxyl bond in the octahedral layers (*e.g.*, Fe-OH in nontronite). Variations in the shape and wavelength of the ~2.2-2.3-μm X-OH

absorption feature and the ~1.4-μm X-OH overtones are due to the specific cation(s) (X) bonded to the hydroxyl. By itself the Al-OH bond typically gives rise to an absorption feature around 2.2 μm, whereas varying degrees of Fe and Mg exchange cause the absorption feature to shift to around 2.3 μm. The distribution and composition of phyllosilicate minerals on Mars can be mapped and measured using CRISM data, which measures reflected sunlight in the visible and near-infrared portions of the spectrum (0.362-3.92 μm). CRISM can acquire data in a targeted mode with a high spatial resolution of 18 or 36 m/pixel in 544 bands, or in one of two survey modes at 100 or 200 m/pixel in 72 bands.

2.0 DATA AND METHODS

CRISM data were processed using the CRISM Analysis Toolkit (CAT) interface (http://pds-geosciences.wustl.edu/missions/mro/crism.htm#Tools). Data were converted to I/F (a ratio of measured spectral radiance to the incoming solar flux) using the procedures described by *Murchie et al.* [2007a, 2007b]. The I/F values were divided by the cosine of the incidence angle as a simple photometric correction to provide an approximation of reflectance. The photometrically corrected values were atmospherically corrected, following the volcano scan method described in *Langevin et al.* [2006] employed by the OMEGA mission [*Mustard et al.*, 2005]. This method compares the depth of the atmospheric 2-μm CO_2 feature to that of an atmospheric transmission spectrum derived from a ratio of spectra from the top and base of Olympus Mons. The 2-μm feature in the scene is fitted to the Olympus Mons atmospheric ratio spectrum and extrapolated to determine the atmospheric transmission at all wavelengths

using the automated CAT interface. A spectral and spatial noise removal routine [after *Parente*, 2008] was also applied to the data. Equations for established spectral parameters from *Pelkey et al.* [2007] were applied to the corrected CRISM images to map different spectral compositions. The BD2290 and D2300 spectral parameters were used to map Fe/Mg smectites. As described in *Ehlmann et al.* [2009], where possible a $n \times n$ pixel region of spectrally bland material was used to ratio against a $n \times n$ pixel region of spectral interest in the same column of the unprojected CRISM image, to remove any residual atmospheric or instrument-related spectral features. If no spectrally bland material was present within the columns of interest, larger regions were chosen that were not necessarily from the same columns. As a final step, the two spectral parameters from *Milliken et al.* [2010, 2011] (described in section 1.1.2) were calculated for spectra from areas identified as containing Fe/Mg smectites in order to assess their potential as markers for metamorphic conditions.

3.0 RESULTS

3.1 Characterization of Fe/Mg smectites

Figure C3 shows a plot of the two spectral parameters that *Milliken et al.* [2010, 2011] used to define zones of chloritization for locations where Fe/Mg phyllosilicates and prehnite/chlorite have been identified, including those newly identified in this work. The data are plotted using two different ranges of the 2.34 μm/2.295 μm band depth ratio parameter so that points that fall within different zones of chloritization are discernable. Also depicted in Figure C3 is a spectral parameter mixing line (green-dashed line) extracted from a suite of synthetic spectra that were created by linearly mixing (in 10%

increments) the spectra of saponite (SapCa-1) and an example prehnite/chlorite spectrum from Nili Fossae. This is the mixing line that would be expected for sub-pixel checkerboard mixing of saponite and prehnite/chlorite. We note that this mixing line is significantly different from the trend inferred from *Milliken et al.* [2011] (gray arrow) as representing chloritization. The spectral parameters extracted from actual CRISM spectra with dominant prehnite/chlorite features in the Nili Fossae region (red circles, Figure C3) fall closer to the linear mixing trendline than the chloritization trend inferred from *Milliken et al.* [2011]. While this would nominally suggest sub-pixel checkerboard mixing is occurring, other evidence from laboratory spectra makes this interpretation less definitive. Spectral parameters extracted from two laboratory spectra of the 50/50 interlayered C/S clay corrensite (orange triangles, Figure C3) suggest chloritization may not always follow the trend inferred from *Milliken et al.* [2011], and may in fact mimic the trend associated with sub-pixel checkerboard mixing. Clearly, more work is required to characterize the trends in spectral parameters that result from the chloritization process.

Nili Fossae CRISM spectra showing a dominant spectral component of Fe/Mg phyllosilicate are plotted in two different colors in Figure C3. Those with relatively high AA values (>167º) are shown as green circles, and those with relatively low AA (<167º) values are shown as blue circles. The green circles are consistent with both the sub-pixel checkerboard mixing trendline and the chloritization trend inferred from *Milliken et al.* [2011], whereas the blue circles are only consistent with the chloritization trend. These facts taken together would suggest that the population of Fe/Mg phyllosilicates as a whole has undergone chloritization. However, additional evidence from other spectral

parameters (discussed in section 4.2) introduces the possibility that other types of low-grade metamorphism, not uniquely distinguishable in using the parameters plotted in Figure C3, have also occurred.

3.2 Mapping of Fe/Mg phyllosilicates

A map of Fe/Mg phyllosilicates with high and low AA values (Figure C1) shows that the two populations occupy geographically distinct regions surrounding Nili Fossae. The low AA value Fe/Mg phyllosilicates (blue triangles) are found in the olivine-rich eastern portion of the region (dashed blue region), whereas the high AA value Fe/Mg phyllosilicates (orange triangles) are found mostly, but not exclusively, in the western portion of the region. Wherever carbonate has been identified (blue circles), only low AA value Fe/Mg phyllosilicates are found. High AA value Fe/Mg phyllosilicates are dominantly associated with occurrences of prehnite/chlorite phases (orange circles). There are some locations that possess both low and high AA value Fe/Mg phyllosilicates. The geochemical significance of the geographic associations is discussed in section 4.2.

3.3 Newly observed locations of metamorphic alteration minerals in Nili Fossae

Using the criteria described by *Ehlmann et al.* [2009] for the spectral identification of metamorphic alteration phases, we have identified several new occurrences of such phases in the Nili Fossae region (Figure C1, colored circles that include a cross hair pattern). None of the minerals in these newly identified locations are inconsistent with the mineral assemblages previously described by *Ehlmann et al.* [2011]. *Ehlmann et al.* [2011] found that prehnite and chlorite are always identified together in mixed spectra. However, we have identified at least one location where prehnite is the dominant phase and chlorite detection is marginal, at best (Figure C2).

4.0 DISCUSSION

The olivine-rich draping unit represents a protolith from which the serpentine likely formed in the Nili Fossae region [*Ehlmann et al.*, 2010]. The identifications of 2.31- and 2.51-μm absorption features in this region have been uniquely attributed to magnesium carbonate, which is likely another product of partial alteration of the olivine-rich unit [*Ehlmann et al.*, 2008]. *Mangold et al.*, [2007] and *Ehlmann et al.*, [2009], noted that where the olivine-rich unit exhibits absorptions at 1.91 and 2.32 μm, due to H_2O and Mg-OH respectively, the 2.5-μm carbonate absorption is weak or absent. *Mangold et al.*, [2007] and *Ehlmann et al.* [2008] suggested these absorptions imply the presence of an Mg-rich phyllosilicate, such as saponite. *Brown et al.*, [2010] proposed, given the context of an olivine-rich protolith and associated magnesium carbonate, that talc is a more likely phase responsible for these spectral features. They identified a spectral signature in CRISM scene FRT000028BA that is consistent with talc, but suggest that talc is spectrally indistinguishable from an Mg-rich smectite, such as saponite. Upon closer inspection, however, we believe talc is in fact spectrally distinguishable from saponite, and furthermore that talc is the dominant Mg-phyllosilicate associated with olivine and magnesium carbonate in Nili Fossae.

4.1 Spectral analysis of Fe/Mg phyllosilicates in Nili Fossae

Figure C4 shows laboratory spectra of saponite and talc. Both phases share similar indistinguishable absorption features with similar relative band depths (compared to the local continuum) at 2.31 and 2.39 μm. However, the gap between the local continuum and the septum at 2.35 μm (between the two absorption bands) is greater in

the saponite spectrum than the talc spectrum. Laboratory spectra of a full suite of Fe/Mg phyllosilicates (shown) reveal that talc is unique within this group in having a septum with this characteristic gap and an absorption feature at 2.31 μm, presumably because talc is the only Mg-OH endmember in its phyllosilicate subgroup. Phlogopite shares the septum gap feature, however, the 2.31 μm feature is shifted to significantly longer wavelengths, a shift resolvable with CRISM spectral resolution. Some Fe/Mg phyllosilicates (*e.g.*, chlorite) do have a reflectance at 2.35 μm that falls below the local continuum, but lack the septum that is present in the talc spectrum. Spectra of the non-phyllosilicate mineral actinolite do display a septum at 2.35 μm that falls below the local continuum and the 2.31 μm absorption feature, but for reasons described below, these phases are thought less likely to be present in this region of Nili Fossae. The magnitude of the continuum-septum gap is given by the relative band depth between the local continuum defined at ~2.2 and 2.42 μm and the local maximum of the septum at 2.35 μm. To distinguish between talc and other phyllosilicate phases (*e.g.*, chlorite) that also display reflectances at 2.35 μm below the local continuum, a second spectral parameter is necessary. These phases have an additional absorption feature at 2.21 μm, which talc lacks. Thus, a plot of relative band depth at 2.35 μm versus relative band depth at 2.21 μm (Figure C5) allows for the separation of talc, prehnite/chlorite, and other Fe/Mg phyllosilicates.

The distinction between Fe/Mg phyllosilicates with high AA values (orange triangles) versus those with low AA values (blue triangles) as determined by parameters from *Milliken et al.* [2011] (Figure C3), becomes much more clearer when plotted with the parameters we have developed to distinguish between talc, prehnite/chlorite, and

Fe/Mg smectites (Figure C5). The population of CRISM spectra from Nili Fossae falls along two distinct trendlines when plotted in this new spectral parameter space. Trendline 1 is composed of Fe/Mg phyllosilicates with high AA values (orange triangles) and Nili Fossae spectra dominated by prehnite/chlorite features (orange circles). As shown in Figure C5, Trendline 1 falls roughly along a vector between laboratory spectra of Fe/Mg smectite and prehnite/chlorite. Points along this trendline represent increasing abundances of prehnite/chlorite toward the upper right portion of the plot (in the direction of the points representing laboratory spectra of prehnite/chlorite). Trendline 2 is composed of Fe/Mg phyllosilicates with low AA values (blue triangles) and is approximately orthogonal to the Trendline 1 in the parameter space of Figure C4. Interestingly, the laboratory spectra of talc (as well as actinolite and phologopite) fall along an extension of Trendline 2. The spectral parameters used in Figure C5 were chosen to separate the talc from Fe/Mg smectite and chlorite, so points along Trendline 2 represent increasing abundances of talc toward the upper left portion of the plot (in the direction of the points representing the laboratory spectra of talc). As we previously noted, talc is spectrally indistinguishable from actinolite, though considering the olivine-rich protolith and the context of associated assemblages with the Fe/Mg phyllosilicate phase (Figure C1), we argue that talc is the most likely spectral candidate. Actinolite is typically formed by metamorphism of basaltic rocks. The spectra of the Fe/Mg phyllosilicate material has a 1 μm absorption consistent with an olivine component [*Brown et al.*, 2010], suggesting it may be mixed with remaining olivine-rich protolith (residual reactant in the carbonation process). If the spectra were actually associated with actinolite, there would be other (unobserved) mineral endmembers expected. With

increasing metamorphism, the onset of actinolite occurs at the transition from the prehnite-pumpellyite facies to the greenschist facies. While this trend may be expected transitioning eastward of the prehnite-pumpellyite assemblages observed in the Nili Fossae region, the assemblages associated with actinolite typically would include other minerals, such as epidote, which have significant spectral features in the near-infrared that are not observed.

It is useful to consider the paleoenvironmental conditions for the Nili Fossae region that would be consistent with the trendlines in Figure C5. A possible interpretation of the points along Trendline 1 is that they represent varying degrees of chloritization of Fe/Mg smectite. Points toward the upper right portion of the plot would represent greater degrees of chloritization, and perhaps correlated with greater burial depth. The points along Trendline 2, which progress towards pure talc, may represent varying degrees of carbonation (equation 2). Interestingly, Trendline 2 does not appear to originate with pure Fe/Mg smectite. Rather, it originates in a region partway along Trendline 1. Chloritization normally occurs when parent rock is buried, so the fact that Trendline 2 originates partway along the chloritization trendline suggests that carbonation occurred after burial to a particular depth.

4.2 Depth dependence and implications of Fe/Mg phyllosilicates in Nili Fossae

Additional insight can be gained by considering the geographic and depth distribution within the Nili Fossae region of the points along the two trendlines in Figure C5. The points that fall along Trendline 1 are dominantly associated with the western portion of the Nili Fossae region (prehnite/chlorite and Fe/Mg phyllosilicates with AA>167º, Figure C1). Because the points representing Fe/Mg phyllosilicates and

prehnite/chlorite are distributed along Trendline 1, rather than concentrated at a single point, varying degrees of chloritization (burial diagenesis) are inferred to have occurred in the eastern portion of the region. Calculating the depth of excavation for exposed phyllosilicates can provide further evidence for the chloritization process. Throughout this region, Fe/Mg phyllosilicates are excavated from some initial depth (D_E) below the currently exposed surface via crater impact processes, and are located in crater ejecta, rims, and central peaks. Using relationships between a crater's final diameter (D) and the excavation depth (D_E), the depth of excavation may be calculated for different displacement mechanisms in cratering mechanics. There are several models that relate the size of the transient crater cavity (D_t) to D on Mars, but for reasons outlined in *Tornabene et al.* [2008], the following equation from *Grieve* [1981] and *Melosh* [1982] can be used to provide a conservative lower limit of D_t:

$$D_t \cong 0.5D . \quad \text{(Eq. 3)}$$

The depth of excavation of phyllosilicates exposed through crater ejecta (d_e) is a function of D_t and can be approximated from *Melosh* [1989]:

$$d_e \cong 0.1D_t . \quad \text{(Eq. 4)}$$

The central peak of a complex crater exposes the deepest-seated materials sampled by a crater. The following relationship between the stratigraphic uplift (SU) in a central peak is based on data from terrestrial impact structures [*Grieve and Pilkington*, 1996]:

$$SU = 0.086D^{1.03} . \quad \text{(Eq. 5)}$$

Finally, a rough estimate of rim uplift can be approximated for complex craters by the following relationship [*Garvin et al.*, 2003]:

$$h_R = 0.02D^{0.84} , \quad \text{(Eq. 6)}$$

though problems including stratigraphic overturn and subsequent erosion arise when estimating this parameter. In this paper, results from equations 4-6 are similarly expressed as a general depth of excavation (D_E), and have been calculated for all occurrences of phyllosilicates associated with Trendline 2 (Figure C5) that have a discernable contextual relationship to either a crater ejecta blanket, rim, or central peak. To illustrate the depth relationship of different phyllosilicate compositions, the spectral parameters presented in Figure C5 have been plot as a function of D_E (Figure C6). A trend of inferred chloritization with increasing D_E is observed; those phases located at the origin of Trendline 1 are excavated from shallower depths than those phases located at the end of Trendline 1 (Figure C6, red arrow). This relationship suggests that burial diagenesis (chloritization) is in fact responsible for the compositional distribution of Fe/Mg-phyllosilicates in the western portion of the Nili Fossae region.

4.3 Spatial distribution and implications of Fe/Mg phyllosilicates in Nili Fossae

By contrast to the Fe/Mg phyllosilicates in the western portion of the Nili Fossae region, those in the eastern portion of the region do not have such marked spectral variability, and typically are unassociated with craters. The fact that the low-carbonation end of Trendline 2 emanates from a localized area along Trendline 1 suggests that the ~160,000 km^2 area in eastern Nili Fossae, where the low AA Fe/Mg phyllosilicates are concentrated, experienced a relatively uniform depth of burial. This is also the portion of Nili Fossae where the olivine-rich cap unit and underlying magnesite are found, as well as the two documented occurrences of serpentine in the region. The local geographic association of olivine, serpentine, magnesite and potentially talc, provides the necessary

solid reactants and products for the serpentization and carbonation processes described in equations (1 and 2).

Evidence for the serpentization and carbonation reactions appears throughout this ~160,000 km^2 area, though neither could have run to completion across the entire region because both olivine and serpentine are still observed. Complete carbonation of serpentine is achieved with low fluid to rock ratios at temperatures ≤ 200º C, but if temperatures remain this low, extended fluid interaction at low temperatures can result in the decarbonation and silicification of the altered rock [*Klein and Garrido*, 2011]. This scenario would not be detectable in the wavelength range used in this study if the replacement is crystalline quartz, as it has no significant spectral features. Amorphous silica (*e.g.*, opal) is detectable with CRISM, however, none is observed within the region outlined in blue (Figure C1). If temperatures increase above 200º C, even high levels of fluid interaction will not cause the dissolution of carbonate [*ibid.*]. Because the magnesium carbonate in Nili Fossae persists, either the temperature of the olivine-rich protolith remained low but fluid interactions were limited, or temperatures above 200º C were reached.

The carbonate-bearing layer in the Nili Fossae region is thought to be mixed with other phases, such as olivine and nontronite, and is matched well with laboratory mixtures containing 80% magnesite [*e.g.*, *Ehlmann et al.*, 2008]. In order to assess the upper limits of the effects of the carbonation of serpentine in this region, we can calculate the total amount of CO_2 and the associated atmospheric pressure trapped in the magnesite in this layer. As an upper limit, we assume the magnesite-bearing layer is uniformly thick across the entire ~160,000 km^2 area where magnesite or talc-related phyllosilicate is

present, with an abundance of 80% magnesite. The upper limit of the thickness of the carbonate-bearing layer can be approximated using the thickness of the olivine-bearing layer (meters to tens of meters thick) [*Mustard et al.*, 2007]. If this thickness is assumed to be 10 m for the entire ~160,000 km^2 area, this would be equivalent to ~6,000 Pa (~0.06 atm) of CO_2 locked in the rock. This is ~10 times the current Martian atmospheric pressure. Although the Nili Fossae region carbonates may not account for all of the hypothesized sedimentary carbonates from ancient Mars [*e.g.*, *Kasting,* 1991], it may reveal an important process that occurred in the subsurface and whose products are otherwise buried.

4.4 Similar assemblages outside of the Nili Fossae region

Evidence for subsurface carbonate is not limited to the Nili Fossae region. The presence of a Fo_{60-80} olivine-carbonate assemblage in the Comanche Spur by the Mars Exploration Rover at Gusev Crater is hypothesized to have formed during the Noachian under neutral pH hydrothermal conditions [*Morris et al.*, 2010]. The assemblage has been compared to carbonates in the Nili Fossae region, and *Morris et al.* [2010] have indicated that the relative remoteness of carbonate outcrops may imply that such environments had multiple occurrences in the Noachian terrain across the globe. Although no significant phyllosilicate component has been observed in the olivine-carbonate assemblages, orbital observations of phyllosilicates in an outcrop near the Comanche Spur appear Mg-rich [*Carter and Poulet*, 2012]. Given the similarity to Nili Fossae assemblages, the Mg-rich phyllosilicates may also have a talc component. CRISM spectra of the Colombia Hills carbonate have an additional 1.9-μm feature,

similar to those in Nili Fossae, indicating the presence of chemically bound water or mixture with a hydrated phase [*Carter and Poulet*, 2012].

Michalski and Niles [2010] have identified carbonate- and phyllosilicate-bearing material exhumed and exposed by crater central uplifts (*e.g.*, Leighton Crater). These authors prefer the hypothesis that these ancient exposed deposits were likely buried and metamorphosed sediments rather than products of hydrothermal alteration in the subsurface, based on morphological evidence of sedimentary features; but the authors acknowledge that CO_2 rich fluids interacting with subsurface basaltic rocks may also explain the presence of these assemblages. The fact that the occurrences of olivine, Mg-phyllosilicate, and carbonate-bearing assemblages are not localized to one region suggests hydrothermal carbonate formation may have been an important process for CO_2 sequestration during the Noachian.

5.0 CONCLUSIONS

The olivine-bearing unit that overlie Noachian phyllosilicate-bearing unit in the Nili Fossae region may have been a target of hydrothermal alteration in the past. We put forth the following sequence of events for the development of alteration assemblages and stratigraphic relationships found in the easternmost portion of the region (Figure C7):

1) Alteration of Noachian-aged crust to Fe/Mg smectite.

2) Uniform burial and the onset of chloritization beneath olivine-rich lava flows or impact ejecta.

3) The overlying olivine-rich unit provides a heat source to drive water from underlying Noachian phyllosilicates and initiates hydrothermal alteration and

serpentization. This step requires an additional component of aqueous silica that may be derived locally (from Si-rich phyllosilicate-bearing material) or from depth (if another fluid source is present).

4) Continued alteration via high temperature (above 200º C) or low temperature (≤ 200º C) fluid-limited carbonation of serpentine to form magnesium carbonate and talc-bearing material mixed with the underlying Noachian mixed-layer clay. This reaction requires additional CO_2 that may be derived locally (melting of buried H_2O-CO_2 ice, *e.g. Changela and Bridges*, [2011]) or from depth (if another fluid source is present).

5) continued burial diagenesis of Noachian phyllosilicates with the onset of Early Hesperian volcanic activity forming the Syrtis lava cap unit.

We also believe that the uniform distribution and consistent co-location of carbonate and talc-bearing mixed-layer clay is consistent with the *Brown et al.* [2010] modification of the *Ehlmann et al.* [2008] hydrothermal hypothesis, suggesting that these units formed through a single hydrothermal event. This hypothesis suggests hydrothermal activity was not restricted to the Noachian era, but was present and possibly prevalent through the Hesperian period via volcanic flows. As *Ehlmann et al.* [2011] suggests, long-term hydrothermal settings may provide habitable environments through an extended period of time in Martian history. Further characterization of Fe/Mg phyllosilicates in this region and in those associated with abundant olivine (*e.g.* Argyre and Terra Tyrrhena [*Koeppen and Hamilton*, 2008]) may indicate carbonation of serpentine was a widespread process on Mars and is the reason for the limited occurrence of serpentine on Mars as shown in *Ehlmann et al.* [2008]. If carbonation of serpentine was a global process, this reaction

could provide a significant atmospheric sink for CO_2 and may have controlled part of the Martian global carbon cycle in the past.

REFERENCES

Arkai P., Sassi F.P., and Desmons J. (2007), A systematic nomenclature for metamorphic rocks. 5. Very low- to low-grade metamorphic rocks. *Recommendations by the IUGS Subcommission on the systematics of metamorphic rocks*. SCMR website (www.bgs.ac.uk/SCMRH).

Bibring, J. -P., et al. (2006), Global mineralogical and aqueous Mars history derived from OMEGA/Mars Express data, *Science*, *312*, 400-404, doi: 10.1126/science.1122659.

Bristow, T. F., et al. (2009), Mineralogical constraints on the paleoenvironments of the Ediacaran Doushantuo Formation, *PNAS*, *106*, 13190-13195.

Brown, A. J., et al. (2010), Hydrothermal formation of clay-carbonate alteration assemblages in the Nili Fossae region of Mars, *Earth and Planetary Science Letters*, *297*, 174-182.

Carter, J. and Poulet, F. (2102), Orbital identification of clays and carbonates in Gusev Crater, *Icarus*, DOI:10.1016/j.icarus.2012.02.024.

Changela, H. G. and J. C. Bridges (2011), Alteration assemblages in the nakhlites: Variation with depth on Mars, *Met. & Planet. Sci.*, *45*(12), 1847-1867.

Clark, R.N., Swayze, G.A., Wise, R., Livo, K.E., Hoefen, T.M., Kokaly, R.F., and Sutley, S.J. (2007), USGS Digital Spectral Library splib06a. U.S. Geological Survey Data, 231.

Ehlmann, B. L., et al. (2008), Orbital identification of carbonate-bearing rocks, *Science*, *322*, 1828-1831.

Ehlmann, B. L. *et al.* (2009), Identification of hydrated silicate minerals on Mars using MRO-CRISM: Geologic context near Nili Fossae and implications for aqueous alteration, *J. Geophys. Res.*, *114*, E00D08, doi:10.1029/2009JE003339.

Ehlmann, B. L., J. F. Mustard, and S. L. Murchie (2010), Geologic setting of serpentine deposits on Mars, Geophys. Res. Lett., 37, L06201, doi:10.1029/2010GL042596.

Ehlmann, B. L. et al. (2011), Evidence for low-grade metamorphism, diagenesis, and hydrothermal alteration on Mars from phyllosilicate mineral assemblages, *Clays and Clay minerals*, *59*(4), 359-377.

Fraeman, A.A., et al. (2009), Evaluating models of crustal cooling using CRISM observations of impact craters in Terra Tyrrhena and Noachis Terra. Lunar & Planetary Science Conference, *40*, abstract 2320.

Frey, M., and Robinson, D. (1999), Low Grade Metamorphism. Blackwell Science, Oxford, 313pp.

Garvin, J. B., S. E. H. Sakimoto, and J. J. Frawley (2003), Craters on Mars: Global Geometric Properties from Gridded MOLA Topography, in *Sixth International Conference on Mars*, NASA/JPL, Pasadena, Calif.

Grieve, R. A. F. (1981), Impact cratering, *Nature*, *291*, 16.

Grieve, R. A. F., and M. Pilkington (1996), The signature of terrestrial impacts, *AGSO J. Aust. Geol. Geophys.*, *16*, 399-420.

Hamilton, V. E., and P. R. Christensen (2005), Evidence for extensive, olivine-rich bedrock on Mars, *Geology*, 33, 433 – 436, doi:10.1130/G21258.1.

Hoefen, T.M., Clark, R.N., Bandfield, J.L., Smith, M.D. Pearl, J.C., and Christensen, P.R. (2003), Discovery of olivine in the Nili Fossae region of Mars. Science, 302, 627–630.

Kasting, J. F. (1991), CO_2 condensation and the climate of Mars, *Icarus*, *94*, 1-13.

Klein, F. and Garrido, C. J. (2011), Thermodynamic constrains on mineral carbonation of serpentinized peridotite, *Lithos*, *126*, 147-160.

Koeppen, W. C., and V. E. Hamilton (2008), Global distribution, composition, and abundance of olivine on the surface of Mars from thermal infrared data, *J. Geophys. Res.*, *133*, E05001.

Langevin, Y., S. Douté, M. Vincendon, F. Poulet, J. –P. Bibring, B. Gondet, B. Schmitt, and F. Forget (2006), No signature of clear CO2 ice from the 'cryptic' regions in Mars' south seasonal polar cap, *Nature*, *447*, 790-792, doi:10.1038/nature05012.

Mangold, N., F. Poulet, J. F. Mustard, J. –P. Bibring, B. Gondet, Y. Langevin, V. Ansan, Ph. Masson, C. Fassett, J. W. Head, H. Hoffmann, and G. Neukum (2007), Mineralogy of the Nili Fossae region with OMEGA/Mars Express data: 2. Aqueous alteration of the crust, *J. of Geophys. Res.*, *112*, E08S04, doi:10.1029/2006JE002835.

Melosh, H. J. (1982), A schematic model of crater modification by gravity, *J. Geophys. Res.*, *87*(B1), 371-380.

Melosh, H. J. (1989), *Impact Cratering: A Geologic Process*, 245 pp., Oxford Univ. Press, New York.

McLennan, S. M. (2003), Sedimentary silica on Mars, *Geology*, *31*, 315-318.

Mumma, M.J., et al. (2009), Strong Release of Methane on Mars in Northern Summer, 2003, *Science*, *323*, 1041–1045.

Murchie, S. L., et al. (2007a), Compact Reconnaissance Imaging Spectrometer for Mars (CRISM) on Mars Reconnaissance Orbiter (MRO), *J. Geophys. Res*, *112*, E05S03, doi:10.1029/2006JE002682.

Murchie, S. L., E. Guinness, and S. Slavney (2007b), CRISM data product software interface specification, ftp://pds-geosciences.wustl.edu/mro-crism/mro-m-crism-2-edr-v1/mrocr_0001/document/crism_dpsis.pdf, *NASA Planet. Data Syst.*, Greenbelt, Md., 17 Aug.

McLennan, S.M. (2003), Sedimentary silica on Mars. *Geology*, 31, 315-318.

Michalski, J. R. and P. B. Niles (2010), Deep crustal carbonate rocks exposed by meteor impact on Mars, *Nature Geoscience*, 3, 751-55, DOI:10.1038/NGE0971.

Milam, K. A., McSween, H. Y., Moersch, J., and Christensen, P. R. (2010), Distribution and variation of plagioclase compositions on Mars: *Journal of Geophysical Research*, v. 115, E09004, doi:10.1029/2009JE003495.

Milliken, R. E., Bristow, T., Bish, D. L., and Mustard, J.F. (2010), The case for mixed-layered clays on Mars, 41st Lunar and Planetary Science Conference, CD #2030.

Milliken, R. E., Bristow, T., and Bish, D. L. (2011), Diagenesis of clay minerals on Mars and implications for the Mars Science Laboratory rover [abs.], 42nd Lunar and Planetary Science Conference, CD #2230.

McSween, H. Y., Hahn, B. C., Viviano, C. E., and Moersch, J. E. (2011), Onset of metamorphism in the Martian crust, 42nd Lunar and Planetary Science Conference, CD #1064.

McSween, H. Y., Taylor, J. G., and Wyatt, M. B. (2009), Elemental composition of the Martian crust, *Science*, 324, 736-739, doi:10.1126/science.1165871.

Morris, R. V., et al. (2010), Identification of carbonate-rich outcrops on Mars by the Spirit Rover, *Science*, 329, 421-424, doi:10.1126/scinece.1189667.

Mustard, J. F., et al. (2005), Olivine and pyroxene diversity in the crust of Mars, *Science*, 307, 1594 – 1597, doi:10.1126/science.1109098.

Mustard, J. F. et al. (2007), Mineralogy of the Nili Fossae region with OMEGA/Mars Express data: 1. Ancient impact melt in the Isidis Basin and implications for the transition from the Noachian to Hesperian, *J. of Geophys. Res.*, *112*, E08S03, DOI:10.1029/2006JE002834.

Mustard, J. F., *et al.* (2008), Hydrated silicate minerals on Mars observed by the Mars Reconnaissance Orbiter CRISM instrument, *Nature*, *454*, 305-309, doi:10.1038/nature07097.

Mustard, J. F. and J. E. Hayes (1997), Effects of hyperfine particles on reflectance spectra from 0.3 to 25 μm, *Icarus, 125*, 145-163.

Parente, M. (2008), A new approach to denoising CRISM images, paper presented at Lunar Planet. Sci., XXXIX, Abstract 2528.

Pelkey, S. M. *et al.* (2007), CRISM multispectral summary products: Parameterizing mineral diversity on Mars from reflectance, *J. Geophys. Res.*, *112*, E08S14, doi:10.1029/2006JE002831.

Poulet, F., J. –P. Bibring, J. F. Mustard, A. Gendrin, N. Mangold, Y. Langevin, R. E. Arvidson, B. Gondet, C. Gomez, and the Omega Team (2005), Phyllosilicates on Mars and implications for early martian climate, *Nature*, *438*, 623-627, doi:10.1038/nature04274.

Poulet, F., N. Mangold, D. Loizeau, J. –P. Bibring, Y. Langevin, J. Michalski, and B. Gondet (2008), Abundance of minerals in the phyllosilicate-rich units on Mars, *Astron. Astrophys.*, *487*, L41-L44, doi:10.1051/0004-6361:200810150.

Reynolds, R. C. (1988), Mixed-layer chlorite minerals, *Mineralogical Society of America, Reviews in Mineralogy*, 19, 601-629.

Robinson, D., Schmidt, S. T., and A. S. de Zamora (2002), Reaction pathways and reaction progress for the smectite-to-chlorite transformation: evidence from hydrothermally altered metabasites, *J. of Metamorphic Geology*, *20*, 167–174.

Schiffman, P. and H. Staudigel, H. (1995), The smectite to chlorite transition in a fossil seamount hydrothermal system: the basement complex of La Palma, Canary Islands, *J. of Metamorphic Geology*, *13*, 487-498.

Schiffman, P., and H. W. Day (1999), Petrological methods for the study of very low grade metabasites. In *Low-grade metamorphism*, M. Frey and D. Robinson, ed. Blackwell, Oxford, p108-142.

Tornabene, L. L., et al. (2008), Surface and crater-exposed lithologic units of the Isidis Basin as mapped by coanalysis of THEMIS and TES derived data products, *J. Geophys. Res.*, *113*, E10001, doi:10.1029/2007JE002988.

Zahnle, K., R. S. Freedman, and D. C. Catling (2011), Is there methane on Mars?, *Icarus*, *212*, 493-503, doi:10.1016/j.icarus.2010.11.02.

Appendix C

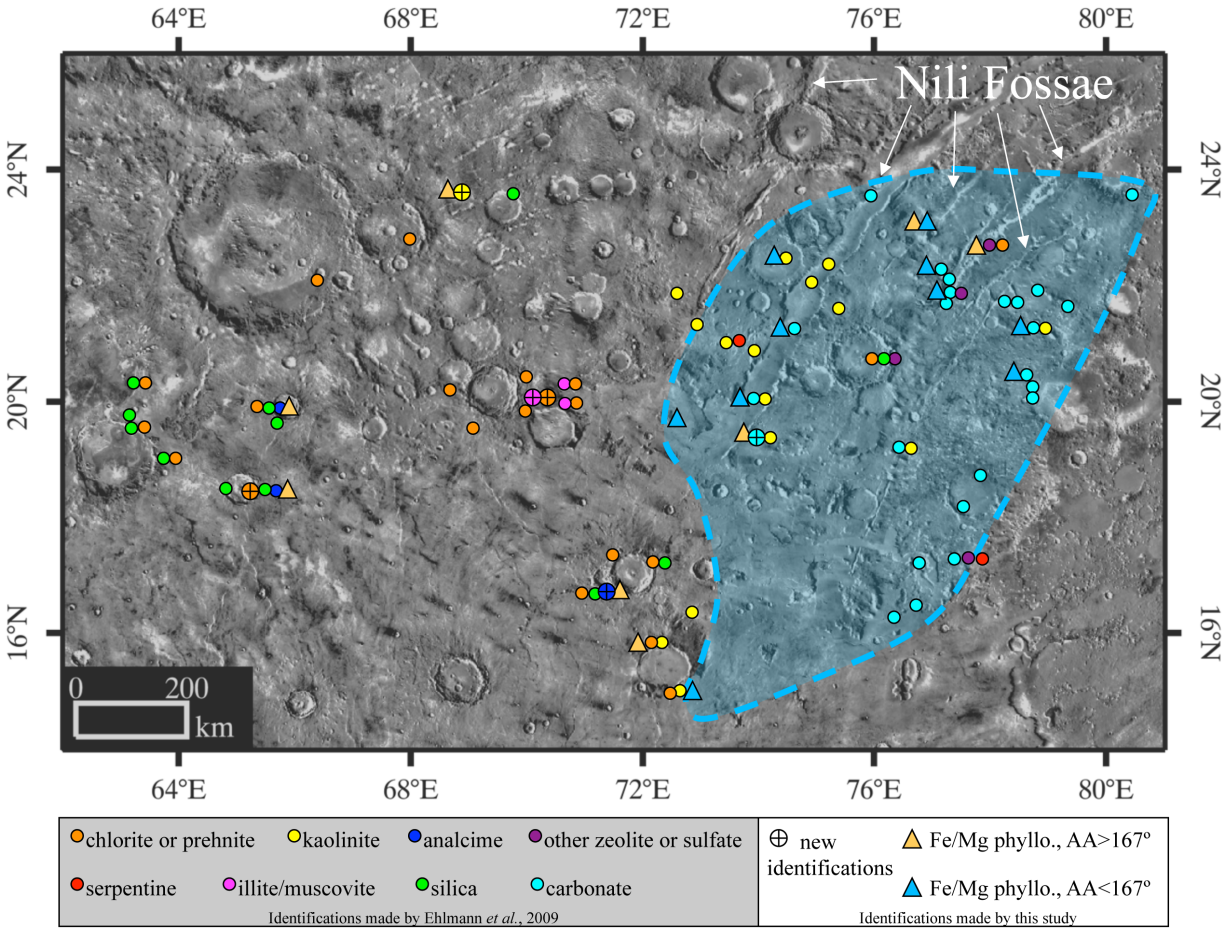

Figure C1. THEMIS daytime infrared mosaic of the Nili Fossae region, with locations of alteration minerals as identified by *Ehlmann et al.* [2009] and this study. Colored circles indicate the locations of minerals identified by *Ehlmann et al.* [2009] (open circles) and the present study (circles with cross hairs). Symbols are placed side-by-side where identifications fall within a single CRISM FRT. The orange triangles indicate a detection of Fe/Mg phyllosilicate with an absorption angle (AA, as defined by *Milliken et al.*, [2011]) greater than 167º (those associated with chloritization). Blue triangles indicate a detection of Fe/Mg phyllosilicate with an absorption angle of less than 167º (those associated with carbonation of serpentine). See section 1.2 for a description of this parameter. Blue dashed line encompasses region where hypothesized carbonation of serpentine occured.

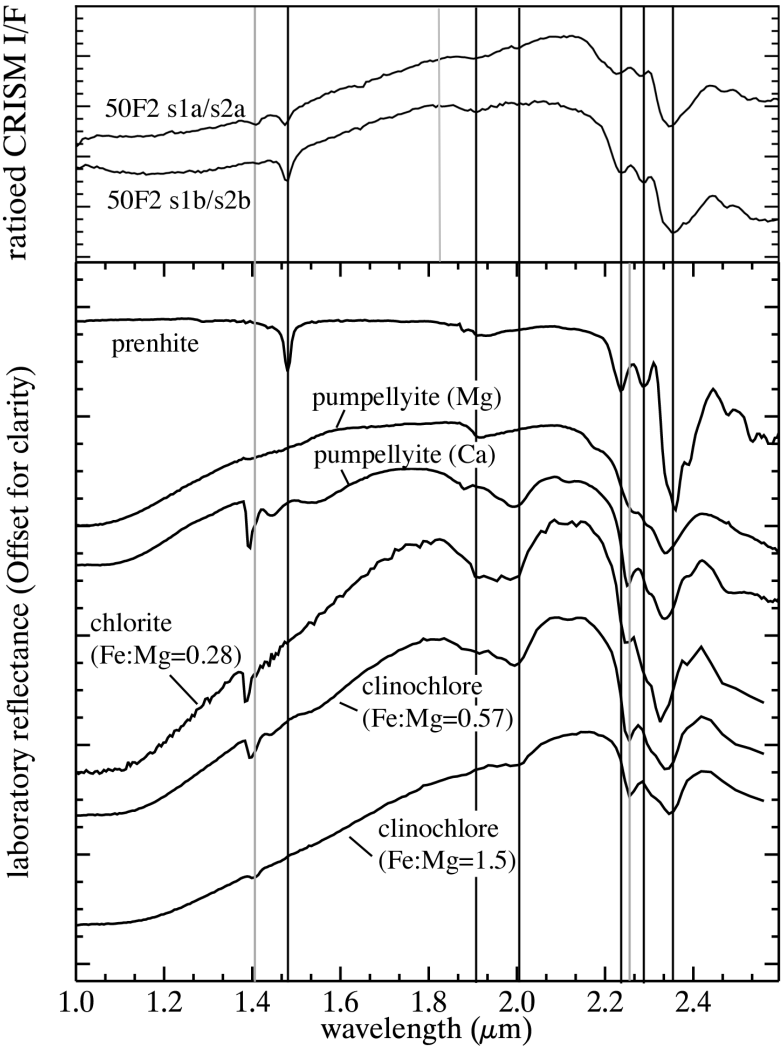

Figure C2. Newly identified prehnite-bearing spectra (without mixing of a chlorite phase) (top) Ratioed CRISM spectra with black vertical lines at 1.48, 1.91, 2.01, 2.22, 2.28, and 2.35 μm indicating the presence of prehnite. Gray vertical lines at 1.41 and 2.24 μm indicative of chlorite and don't appear coincident with CRISM spectra, particularly example b. (bottom) Library spectrum of prehnite (GDS613.a), chlorite (chlorite_smr13.4984), clinochlore Fe:Mg=0.57 (clinochlore_gds158.5327), clinochlore Fe:Mg=1.5 (clinochlore_gds157.5542) [*Clark et al.,* 2007]; pumpellyite, ca-rich (ZE-EAC-001-c1ze01), pumpellyite mg-rich (ZE-EAC-002-c1ze02) [RELAB].

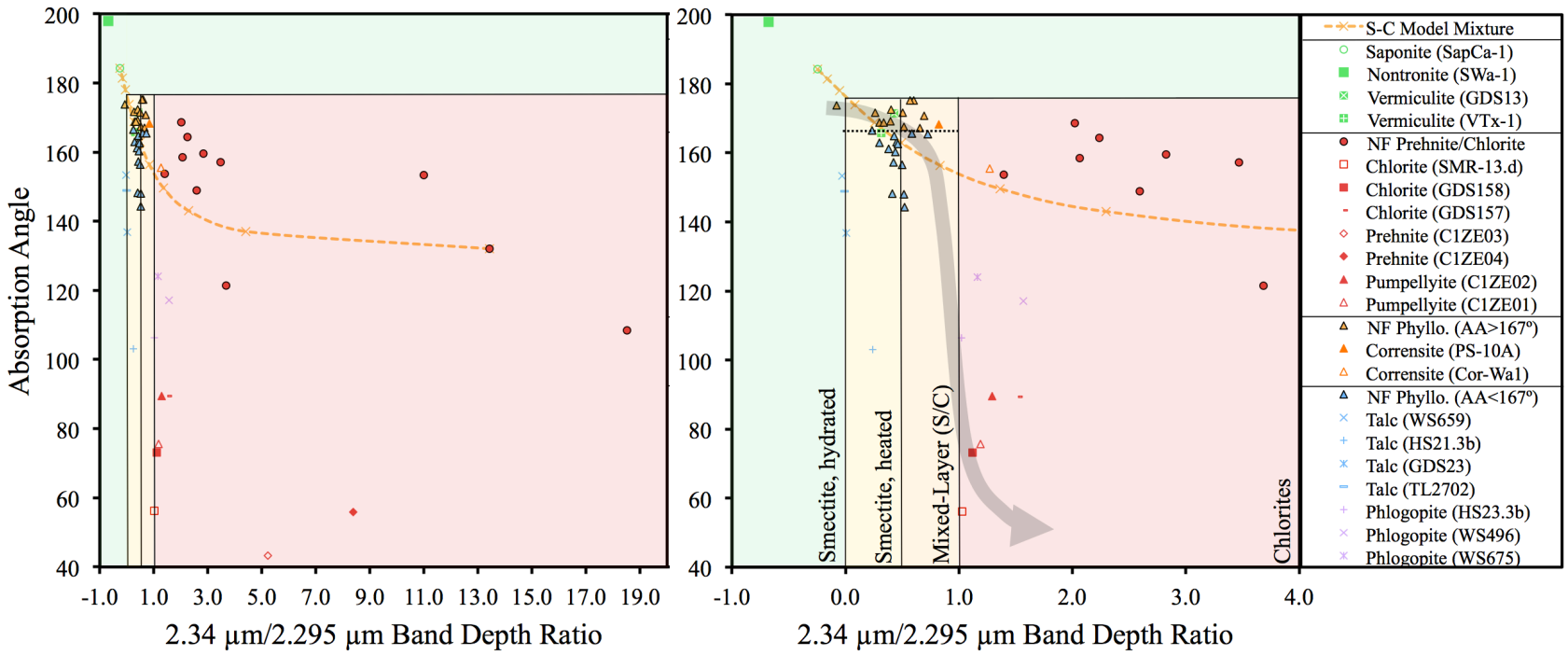

Figure C3. *Milliken et al.* [2011] parameter plot characterizing unaltered smectite, heated smectite, mixed-layered S/C, and chlorite. Smectite and prehnite/chlorite compositions from Nili Fossae (NF) are shown in filled circles and are plotted with library spectra from [*Clark et al.*, 2007] and RELAB. (left) Full distribution of NF chlorite is shown. Orange hashed line indicates linear mixing model between a selected NF chlorite and library saponite at 10% intervals. (right) Same parameters as in left panel, but spanning a restricted range of the band depth ratio (x-axis values) to allow for visual separation of the unaltered, heated, and mixed-layered zones. Mixing model appears consistent with laboratory mixed-layer S/C clays (corrensite) and trends through NF phyllosilicates with higher AA values. NF phyllosilicates with values less than 167° (indicated by dotted black horizontal line) appear to trend along a vertical line indicating a decrease in AA. Typically this trend indicates chloritization [*Milliken et al.*, 2011] towards the location of laboratory chlorite compositions (gray arrow). However, we argue this trend is better explained by the presence of talc (see section 4.2).

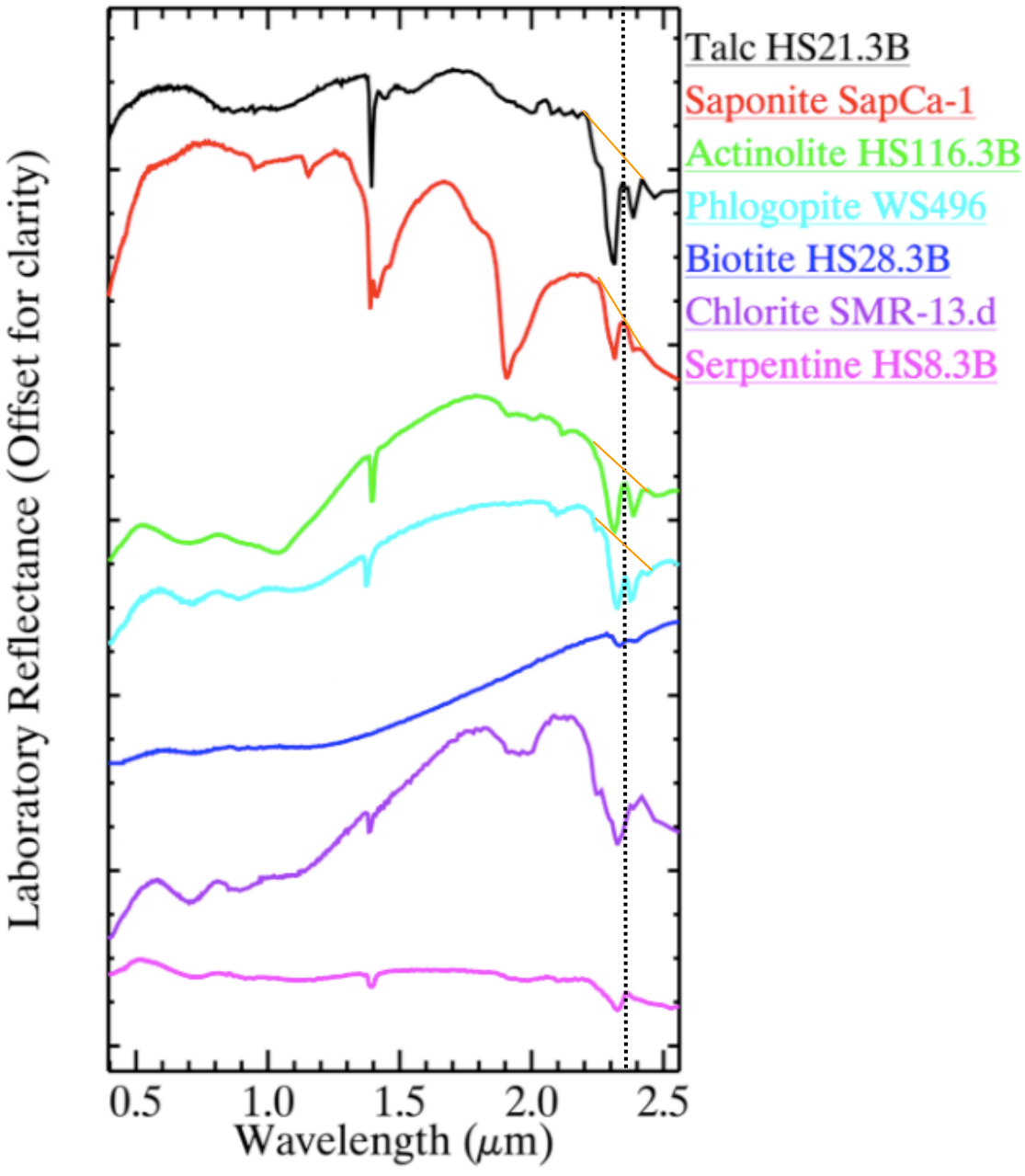

Figure C4. Comparison of Fe/Mg phyllosilicate versus talc laboratory spectra. Both saponite and talc share similar absorption features at 2.31 and 2.39 µm [*e.g.*, *Brown et al.*, 2010]. Local continuum between ~2.2 and 2.42 µm is shown in orange. A larger gap between the local continuum and the septum at 2.35 µm (dotted black vertical line) is present in the talc spectrum. Library spectra are from [*Clark et al.*, 2007].

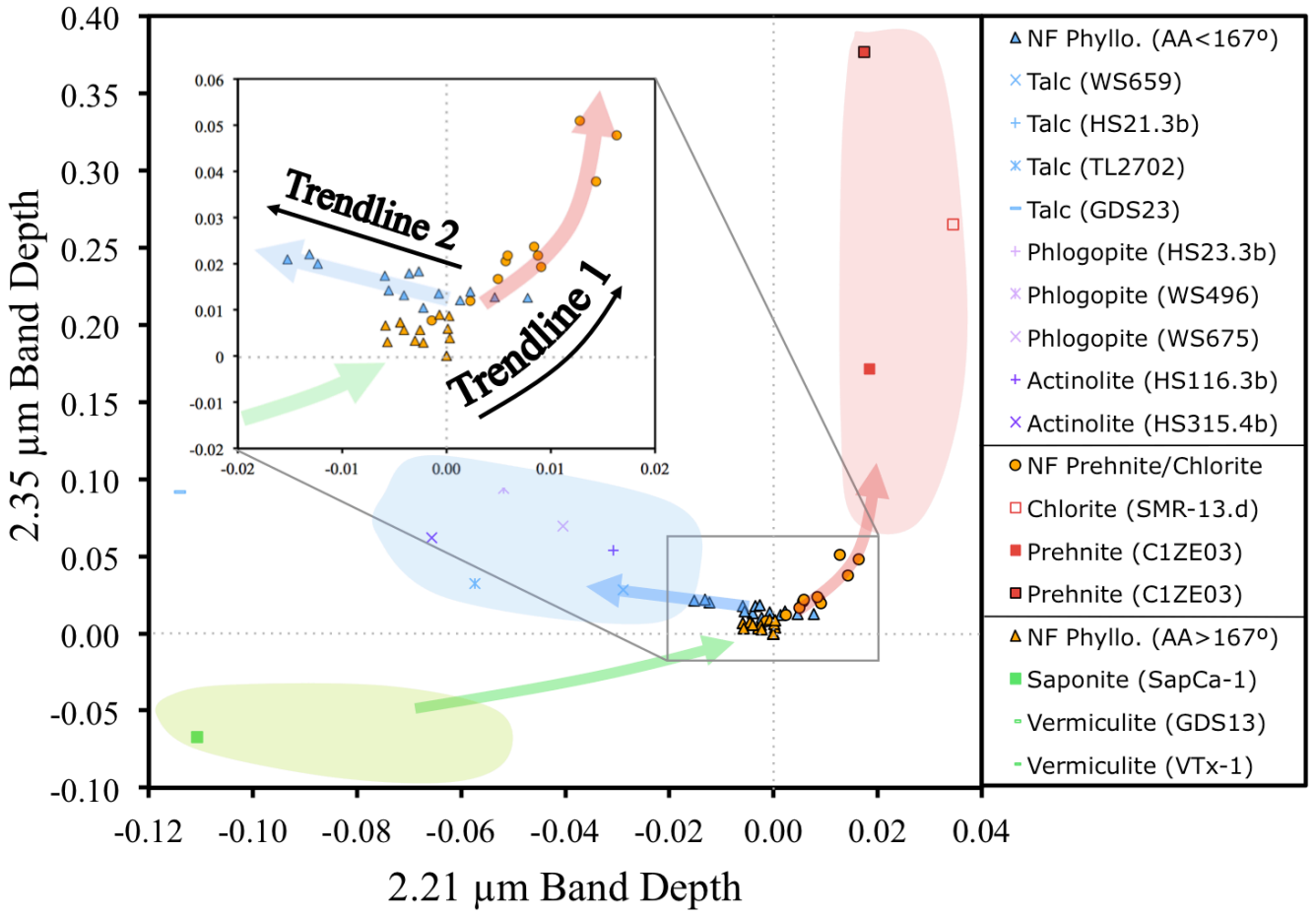

Figure C5. Relative band depth at 2.35 µm verses 2.210 µm for Fe/Mg phyllosilicates in the Nili Fossae (NF) region. As shown in Figure 5, the band depth at 2.355 µm can be used to differentiate between saponite and talc. Phyllosilicates with AA values of less than 167º (as defined in Figure 4) do not trend towards library chlorite phases (indicating chloritization), but rather trend towards the composition of library talc (also coincident with spectrally indistinguishable actinolite). The path of these phyllosilicates originates partway up the chloritization process and is distinct from phyllosilicates (AA>167º) that could originate from the saponite endmember. Library spectra from [*Clark et al.*, 2007] and RELAB.

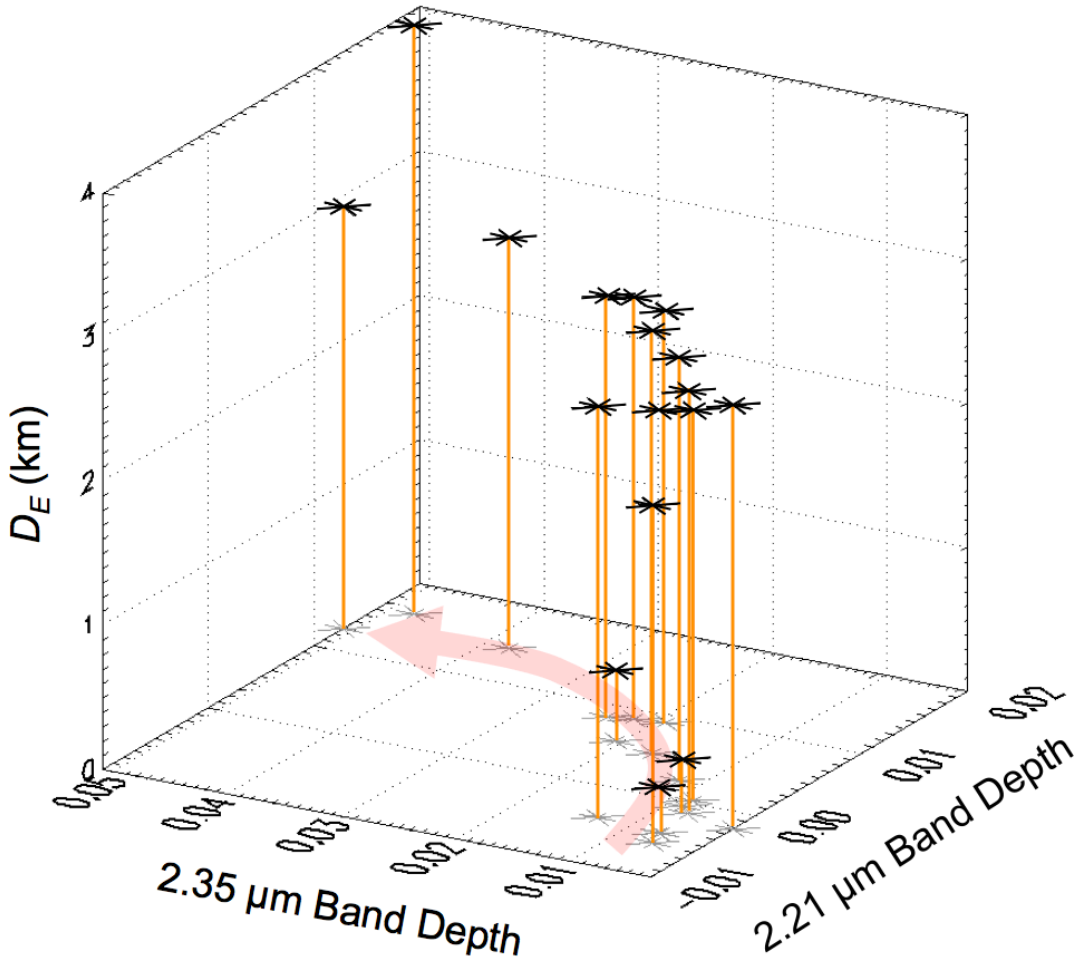

Figure C6. Depth of excavation (D_E) versus relative band depth at 2.35 µm and 2.210 µm for Fe/Mg phyllosilicates in the Nili Fossae region. Phyllosilicates associated with Trendline 1 (talc-related phyllosilicates) are not shown here, as the majority of them are unassociated with apparent craters. Points are projected onto the X-Y axis (spectral parameters) via orange vertical lines. The red arrow indicates Trendline 1 (from Figure C5), or the inferred trend of chloritization.

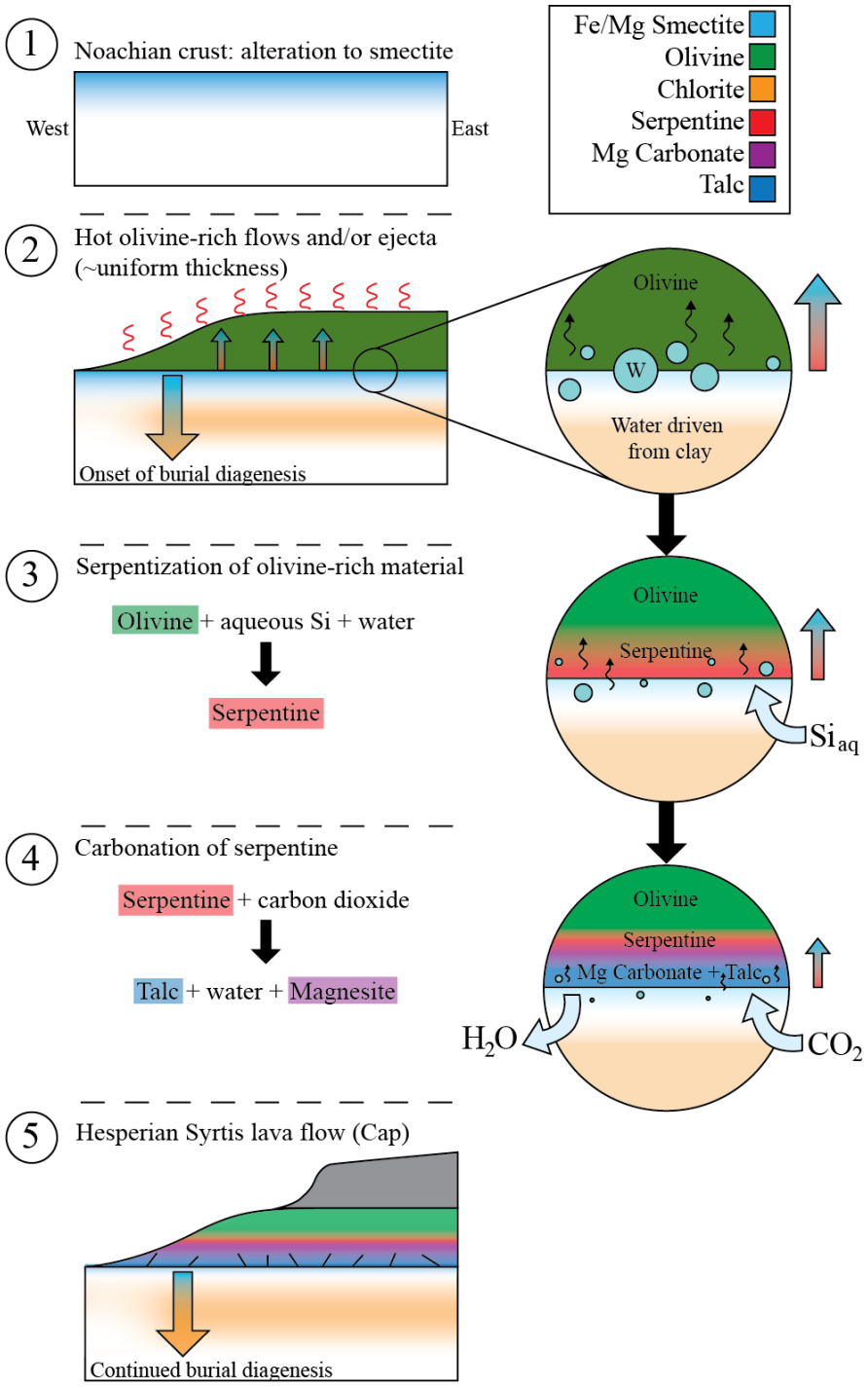

Figure C7. Schematic diagram through a possible geologic time sequence of the eastern portion of the Nili Fossae region. A walkthrough of this diagram can be found in section 5.0.

Part 5
Conclusion

In part 2 we develop a statistically optimized band ratio technique for mapping phyllosilicates with THEMIS daytime thermal infrared data. This technique is particularly useful as THEMIS coverage is nearly global and has relatively high spatial resolution (100 m/pixel). This allows for the mapping of phyllosilicate-bearing units beyond those areas of coverage with CRISM. We derive an initial formulation of an index used to map phyllosilicates with THEMIS by quantifying the spectral variability of a synthetic suite of Martian basalt spectrum mixed with laboratory phyllosilicate spectra. This initial formulation was refined by optimizing the correlation between co-located observations of phyllosilicates with the CRISM instrument on a scene-by-scene basis. This application of this method in Mawrth Vallis and Nili Fossae results in the first 100 m/pixel regional phyllosilicate maps generated for those regions. The approach utilized in this study has further applications for other cross-wavelength and cross-instrument mapping of phases that have spectral features in both wavelength ranges.

In part 3 we examine the effect of spatial resolution on the ability to detect phyllosilicates with the THEMIS vs. TES instruments in an effort to address the discrepancy of TES detections of phyllosilicates (at detection limits) as compared to CRISM and OMEGA detections (upwards of 65% phyllosilicate). We find that the improved spatial resolution THEMIS significantly increases the likelihood of phyllosilicate detection based on modeling of actual distributions of phyllosilicates on the surface of Mars. Thus, despite the limited spectral resolution of THEMIS, we apply spectral unmixing techniques to THEMIS spectra in the Mawrth Vallis phyllosilicate-rich region. We present the first phyllosilicate abundance map of units in this region and

reevaluate the proposed formation mechanisms for clay in this region, and find that abundance of alteration phases are consistent with leaching in an open system.

Finally, in part 4 we provide evidence for the carbonation of serpentine in the Nili Fossae region. The spectral identification of serpentine, magnesium carbonate, and an olivine-rich protolith in the Nili Fossae region suggest a hydrothermal origin for the formation of serpentine and magnesium carbonate. We have further characterized Fe/Mg phyllosilicate-bearing material associated with these minerals and show that they are likely a mixture of uniformly chloritized mixed-layer S/C clay and a talc component. When mapping the locations of phyllosilicates with this talc component in the Nili Fossae region, we find magnesium carbonates are exclusively associated with these phases. We provide an explanation for these phases that includes the uniform burial of Noachian Fe/Mg smectites, the serpentization of olivine through hydrothermal alteration via overlying olivine-rich material, and finally the carbonation of that serpentine. This final reaction explains the co-occurrence of carbonate and talc in the easternmost parts of the Nili Fossae region. Furthermore, if this process occurs as a global phenomenon on Mars, it may provide a sink for CO_2 in the Martian past.

VITA

Christina Elizabeth Viviano was born on April 30th, 1984 in Ann Arbor, Michigan, the daughter of Frank and Jeanette Viviano. She grew up in West Linn, Oregon, was homeschooled by her dedicated parents for two years in middle school, and attended St. Mary's Academy for high school. Christina's interest in geology was sparked during many summers spent collecting rocks and fossils with her grandparents at their cottage on Lake Erie. After graduating high school, Christina attended Colgate University in Hamilton, New York, and under the guidance of Dr. Thomas Balonek, graduated magna cum laude with a Bachelor of the Arts in Astrogeophysics and a minor in Geology in 2006. Christina held two summer research internships, one at Colgate University studying diatoms in Antarctic Ocean floor sediments and another at University of Colorado, Boulder quantifying Colorado Front Range seismicity. While attending Colgate, Christina spent a semester abroad at the University of Wollongong, Australia, where she was first introduced to remote sensing techniques that inspired her academic pursuit in Martian surface geology and spectroscopy.

Christina entered the Earth and Planetary Sciences doctoral program at the University of Tennessee, Knoxville, in Fall 2006 under the advisement of Dr. Jeffrey Moersch. She taught many laboratory courses at the University of Tennessee, including Introductory Geology, Introduction to Planetary Geology, Planetary Geology, and graduate level Remote Sensing. She also participated in successful outreach opportunities for students between pre-K through college-level in the Southeast. Christina received the Dwornik Award for her poster presentation at LPSC 2011. The research Christina conducted while at the University of Tennessee culminated in this document, and she was awarded the Doctor of Philosophy degree on May 10, 2012. Upon completion of her dissertation defense, she began a postdoctoral research associate position at the Johns Hopkins Applied Physics Laboratory in January, 2012.